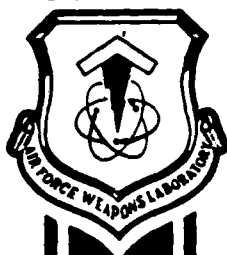


2

LINEAR STABILITY OF RELATIVISTIC SPACE-CHARGE FLOW IN A MAGNETICALLY INSULATED TRANSMISSION LINE OSCILLATOR

R. W. Lemke

April 1989



AD-A207 793

A
F
W
L

Final Report

Approved for public release; distribution unlimited.

AIR FORCE WEAPONS LABORATORY
Air Force Systems Command
Kirtland Air Force Base, NM 87117-6008

DTIC
ELECTE
MAY 10 1989
S H D

C19

UNCLASSIFIED

SECURITY CLASSIFICATION OF THIS PAGE

REPORT DOCUMENTATION PAGE

1a. REPORT SECURITY CLASSIFICATION UNCLASSIFIED			1b. RESTRICTIVE MARKINGS		
2a. SECURITY CLASSIFICATION AUTHORITY			3. DISTRIBUTION / AVAILABILITY OF REPORT		
2b. DECLASSIFICATION / DOWNGRADING SCHEDULE			Approved for public release; distribution unlimited.		
4. PERFORMING ORGANIZATION REPORT NUMBER(S) AFWL-TR-88-103			5. MONITORING ORGANIZATION REPORT NUMBER(S)		
6a. NAME OF PERFORMING ORGANIZATION Air Force Weapons Laboratory		6b. OFFICE SYMBOL (If applicable) AWPB		7a. NAME OF MONITORING ORGANIZATION	
6c. ADDRESS (City, State, and ZIP Code) Kirtland Air Force Base, NM 87117-6008			7b. ADDRESS (City, State, and ZIP Code)		
8a. NAME OF FUNDING / SPONSORING ORGANIZATION		8b. OFFICE SYMBOL (If applicable)		9. PROCUREMENT INSTRUMENT IDENTIFICATION NUMBER	
8c. ADDRESS (City, State, and ZIP Code)			10. SOURCE OF FUNDING NUMBERS		
			PROGRAM ELEMENT NO 61102F	PROJECT NO 2301	TASK NO Y2
			WORK UNIT ACCESSION NO 10		
11. TITLE (Include Security Classification) LINEAR STABILITY OF RELATIVISTIC SPACE-CHARGE FLOW IN A MAGNETICALLY INSULATED TRANSMISSION LINE OSCILLATOR					
12. PERSONAL AUTHOR(S) Lemke, Raymond W.					
13a. TYPE OF REPORT Final		13b. TIME COVERED FROM 2Jan86 to 31May88		14. DATE OF REPORT (Year, Month, Day) 1989 April	
				15. PAGE COUNT 106	
16. SUPPLEMENTARY NOTATION					
17. COSATI CODES			18. SUBJECT TERMS (Continue on reverse if necessary and identify by block number)		
FIELD	GROUP	SUB-GROUP	MILO Magnetically insulated transmission line		
			Slow-wave structure Relativistic Brillouin flow		
			Space-charge waves Slow electromagnetic waves (over)		
19. ABSTRACT (Continue on reverse if necessary and identify by block number)					
<p>The magnetically insulated transmission line oscillator (MILO) is a high-power microwave device that combines the technologies of magnetically insulated electron flow and slow-wave tubes. This combination makes the MILO a unique and robust device capable of operation over a wide range of voltages.</p> <p>MILOs are linear, two-conductor systems comprised of a cathode and an anode. The cathode is a smooth conductor. The anode consists of periodically spaced cavities. The system forms a slow-wave transmission line capable of transmitting electromagnetic waves having phase velocities less than the speed of light (slow waves).</p> <p>MILO operation is initiated by charging the cathode to high voltage with respect to the anode. The large electric field on the cathode surface generates a plasma from which electrons are emitted. For sufficiently high voltage, the electrons are magnetically (over)</p>					
20. DISTRIBUTION / AVAILABILITY OF ABSTRACT <input checked="" type="checkbox"/> UNCLASSIFIED/UNLIMITED <input type="checkbox"/> SAME AS RPT <input type="checkbox"/> DTIC USERS			21. ABSTRACT SECURITY CLASSIFICATION UNCLASSIFIED		
22a. NAME OF RESPONSIBLE INDIVIDUAL Raymond W. Lemke, PhD			22b. TELEPHONE (Include Area Code) (505) 844-0121		22c. OFFICE SYMBOL AWPB

DD FORM 1473, 84 MAR

83 APR edition may be used until exhausted.

All other editions are obsolete.

SECURITY CLASSIFICATION OF THIS PAGE
UNCLASSIFIED

18. SUBJECT TERMS (Continued)

Vlasov equation
Floquet expansion
Dispersion relation

19. ABSTRACT (Continued)

insulated from the anode and drift down the transmission line with substantial kinetic energy.

The presence of electrons excites the anode cavities which oscillate at their fundamental frequencies. These oscillations are comprised of slow and fast electromagnetic waves.

A microwave generating instability occurs when the slow electromagnetic wave phase velocity is slightly less than the electron drift velocity. In this case, wave amplification occurs at the expense of electron energy.

We present a linear analysis of the microwave instability in which we derive a dispersion relation for allowed modes in a cylindrical MIO. The dispersion relation is obtained by applying linear perturbation theory to Maxwell's equations coupled to equations for the electron equilibrium. Two models are used for the electron equilibrium: (1) thin-beam, and (2) relativistic Brillouin flow. The dispersion relation is numerically solved to obtain oscillation frequencies and growth rates of modes in the MIO. We compare the linear theory results with numerical simulation, and obtain excellent agreement.

ACKNOWLEDGEMENTS

I thank the following people for providing me with useful technical interaction throughout the course of this work: Dr Brendan Godfrey, Dr Colston Chandler, Dr Norman Roderick, and Dr Thomas Hughes.

This work was performed in the Advanced Technology Division of the Air Force Weapons Laboratory, Kirtland Air Force Base, New Mexico, and supported by the Air Force Office of Scientific Research, Bolling Air Force Base, DC.

Accession For	
NTIS GRA&I	<input checked="" type="checkbox"/>
DTIC TAB	<input type="checkbox"/>
Unannounced	<input type="checkbox"/>
Justification	
By	
Distribution/	
Availability Codes	
Dist	Avail and/or
A-1	Special



CONTENTS

<u>Section</u>		<u>Page</u>
1.0	INTRODUCTION	1
2.0	BACKGROUND	4
	2.1 MAGNETICALLY INSULATED TRANSMISSION LINES	4
	2.2 SPACE-CHARGE WAVES	11
	2.3 PERIODIC STRUCTURES AND SLOW ELECTROMAGNETIC WAVES	14
	2.4 QUALITATIVE DESCRIPTION OF MILO OPERATION	16
3.0	MILO DISPERSION RELATION FOR THIN BEAMS	20
4.0	NUMERICAL SOLUTION OF THE THIN-BEAM DISPERSION RELATION	32
	4.1 NUMERICAL SOLUTION OF EQUATION 62	32
	4.2 COMPARISON WITH NUMERICAL SIMULATION I	48
5.0	MILO DISPERSION RELATION FOR RELATIVISTIC BRILLOUIN FLOW	57
6.0	NUMERICAL SOLUTION OF THE MILO DISPERSION RELATION FOR RBF EQUILIBRIUM	66
	6.1 DISPERSION RELATION SOLUTIONS INCLUDING THE EFFECTS OF RBF	67
	6.2 COMPARISON WITH NUMERICAL SIMULATION II	71
7.0	CONCLUSIONS	76
	REFERENCES	78
	APPENDICES	
	A. PERIODIC ANODE FUNCTIONS USED IN MILO STABILITY ANALYSIS	81
	B. EQUILIBRIUM DISTRIBUTION FUNCTION FOR RELATIVISTIC BRILLOUIN FLOW	85
	C. EVALUATION OF THE PERTURBED CURRENT DENSITY INTEGRAL $I_n^*(f_0)$	91
	D. ANALYSIS OF SOLUTIONS TO EQUATION 93 ABOUT SINGULAR POINTS	93

FIGURES

<u>Figures</u>		<u>Page</u>
1.	Types of electron flow in coaxial transmission lines.	5
2.	Dispersion diagram for TM_{0n} waves in a coaxial transmission line containing a monoenergetic electron beam.	13
3.	Schematic of a hollow, cylindrical, slow waveguide.	15
4.	Dispersion diagram for TM_{0n} waves in a hollow, cylindrical, slow waveguide.	16
5.	Schematic of a cylindrical MILO.	18
6.	Model of MILO used in the linear theory.	21
7.	Dispersion diagram for TM_{0n} waves in a hollow, cylindrical, rippled waveguide.	34
8.	Dispersion diagram for TM_{0n} waves in a coaxial rippled waveguide.	36
9.	Dispersion diagram for TM_{0n} waves in a coaxial rippled waveguide showing sensitivity to structure period.	38
10.	Dispersion diagram for TM_{0n} waves in a coaxial rippled waveguide showing sensitivity to slot depth.	39
11.	Dispersion diagram for TM_{0n} waves in a smooth, coaxial transmission line containing an annular, monoenergetic electron beam.	41
12.	Dispersion diagram for TM_{0n} waves in a smooth, coaxial transmission line containing an annular, monoenergetic electron beam showing sensitivity to beam current.	42
13.	Dispersion diagram for TM_{0n} waves in a smooth, coaxial transmission line containing an annular, monoenergetic electron beam showing sensitivity to beam velocity.	43
14.	MILO dispersion relation for thin beams.	45
15.	MILO dispersion relation for thin beams showing sensitivity to beam velocity.	47
16.	Schematic of geometry used in ISIS MILO simulation.	49
17.	Dispersion relation for TM_{0n} waves in ISIS simulation geometry.	50

FIGURES (Concluded)

<u>Figures</u>		<u>Page</u>
18.	Dispersion relation for TM_{0n} waves in ISIS simulation geometry including space-charge effects.	51
19.	ISIS MILO simulation: particle plot.	52
20.	ISIS MILO simulation: axial field amplitude versus Z.	54
21.	ISIS MILO simulation: time history and Fourier transform of the axial electric field.	55
22.	Dispersion diagram for space-charge waves associated with RBF.	68
23.	MILO dispersion diagram including the physics of RBF.	70
24.	ISIS MILO simulation results showing details of electron flow.	73
25.	ISIS MILO simulation results showing details of the axial electric field spectrum.	74
A-1.	Sinusoidal model of a MILO.	82
A-2.	Square-wave model of a MILO.	82
A-3.	Double hyperbolic tangent model of a MILO.	84

Table

1.	Oscillation frequency and maximum growth rate of unstable TM modes in Fig. 23.	69
2.	Dependence of growth rate on electron radius and MILO voltage.	71

1.0 INTRODUCTION

The magnetically insulated transmission line oscillator (MILO) is a microwave device, potentially of gigawatt power, that combines the technologies of magnetically insulated electron flow and slow-wave tubes. This combination makes the MILO a unique and robust device capable of operation over a wide range of voltages.

MILOs are two-conductor systems comprised of a smooth inner conductor, the cathode, and an outer conductor, the anode, that consists of periodically spaced cavities. MILO operation is initiated by generating a large potential difference, kilovolts to megavolts, across the anode-cathode (A-K) gap. The large electric field associated with the voltage will cause a plasma to form on the cathode surface. The plasma is a source of electrons that flow into the A-K gap. The electron flow constitutes a current with an associated magnetic field, the strength of which increases with applied voltage. For sufficiently high voltage, the force associated with the self-generated magnetic field is strong enough to bend electron trajectories such that they are parallel to the anode. In this case, electrons are prevented from reaching the anode, thereby allowing high-power operation without vacuum breakdown associated with plasma generation by electrons impacting the anode. The resulting equilibrium consists of electrons drifting parallel to the transmission line axis in crossed electric and magnetic fields. This equilibrium is short-lived because the drifting electrons excite, and subsequently interact with, slow electromagnetic waves fundamental to the periodic A-K system. In particular, slow transverse magnetic waves are amplified by this process at the expense of electron energy.

Combining magnetically insulated flow and periodic structures for the purpose of generating microwaves was apparently first suggested by Bekefi (Ref. 1) in the mid-1970s, but was not extensively pursued. Increasing interest in the high-power microwave sources, in combination with the availability of adequate drivers, led to the rebirth of Bekefi's idea in the form of the MILO in 1985.*

* This idea was first suggested by M.C. Clark, formerly of the Advanced Technology Division, Air Force Weapons Laboratory, Kirtland AFB, NM, and now with Sandia Natl Lab (SNL), Albuquerque, NM. The name MILO is attributed to B. Marder of SNL.

This report presents the first detailed theoretical analysis of the microwave generating instability in MILO devices. The analysis is composed of a combination of linear perturbation theory and numerical simulation using a two-dimensional particle-in-cell computer code. The main theoretical result is a dispersion relation that is used to predict frequency and growth rate of the MILO instability.

Section 2.0 provides background concerning the physics of magnetic insulation, space-charge waves, and slow-wave systems.

In Sec. 3.0, linear perturbation theory is applied to a set of coupled field-fluid equations to derive a dispersion relation for electromagnetic and space-charge modes allowed in a coaxial MILO device. In this case, we use the standard technique of modeling the electron flow with an infinitesimally thin annular beam because the resulting perturbed field equations can be solved analytically. Although this constrains the resulting dispersion relation to a particular equilibrium, it is valid for general periodic geometries, coaxial or not.

In Sec. 4.0, we numerically solve the thin-beam dispersion relation and investigate its solution for a variety of geometrical and space-charge parameters. The numerical solution shows that the MILO instability is a result of unstable coupling between slow electromagnetic waves and space-charge waves. Numerical simulation is used to confirm frequency predictions obtained with the dispersion relation.

Section 5.0 uses a more general approach to derive a dispersion relation. In this case, linear perturbation theory is applied to a coupled set of field and kinetic equations. Electrons are modeled with a two-dimensional distribution function which corresponds to laminar, magnetically insulated flow having finite thickness. Starting with Vlasov's equation, we derive an expression for the perturbed distribution function. This is then used in corresponding field equations to obtain a dispersion relation. This dispersion relation is a considerable improvement over the one obtained in Sec. 3.0, because not only does it apply to general periodic waveforms, it also includes the physics of magnetically insulated electron flow. Although the dispersion

relation derived is restricted to laminar flow, this approach can be generalized to nonlaminar equilibria, albeit with significantly increased difficulty in numerically solving the resulting equations.

Section 6.0 investigates the numerical solution of the dispersion relation containing the physics of magnetically insulated electron flow. Computational studies are performed that show the effect of changing parameters associated with electron equilibria. We compare results with numerical simulation and obtain excellent agreement.

Conclusions are presented in Sec. 7.0.

2.0 BACKGROUND

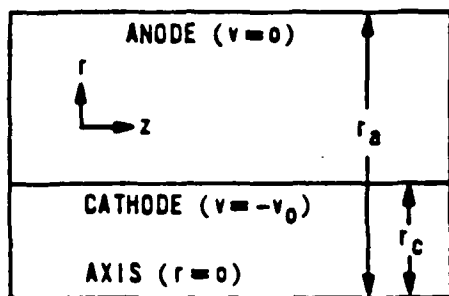
This section reviews the basic physics that determines MILO behavior. Important results from the theory of magnetically insulated transmission lines (MITLs), space-charge waves, and periodic structures are presented as a prerequisite to understanding MILO operation. Some of these results will be used later to analyze the stability of space-charge flow in the MILO. The intent is not to present the complicated derivations, but to provide the reader with enough background to comfortably follow the analysis in succeeding sections. All topics discussed in this section have been thoroughly discussed in the open literature and appropriate references are provided for the person desiring more detailed information.

2.1 MAGNETICALLY INSULATED TRANSMISSION LINES

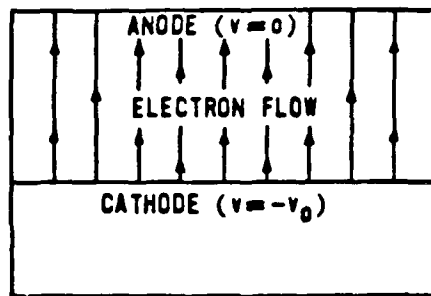
MITLs can be used to deliver considerable energy (megajoules) to a matched load in vacuo. The phenomenon of self-insulation permits the maintenance of large voltages (megavolts) on a transmission line for times longer than attainable in ordinary vacuum gaps. The combination of magnetically insulated flow and slow-wave tube physics is what makes the MILO a potentially high-power microwave device.

For the purpose of discussion, consider coaxial transmission lines having cylindrical symmetry. This is not an important restriction because the basic physics is independent of the transmission line geometry.

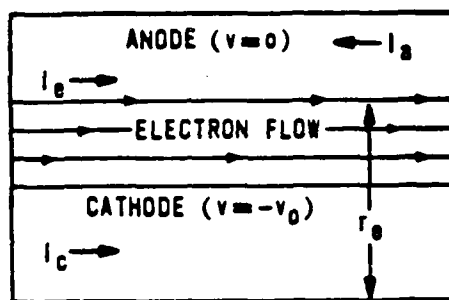
Figure 1a depicts a segment of coaxial transmission line having inner radius r_c , outer radius r_a , and length L . The inner and outer conductors will be referred to as cathode and anode, respectively. The space defined by $r_c \leq r \leq r_a$ is called the A-K gap. The entire system is under vacuum. We assume the line is long enough ($r_a - r_c \ll L$) so that end effects can be neglected in the segment under consideration; however, note that the manner in which the line is terminated has considerable influence on the equilibrium. Space-charge flow in the gap is initiated by charging the cathode (for example) to some potential ($-V_0$) with respect to ground (the anode). When



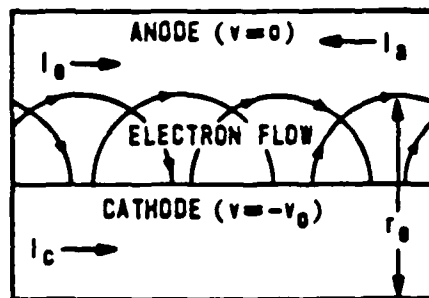
(a) COAXIAL TRANSMISSION LINE.



(b) CHILD LANGMUIR FLOW.



(c) RELATIVISTIC BRILLOUIN FLOW.



(d) NON-LAMINAR INSULATED FLOW.

Figure 1. Types of electron flow in coaxial transmission lines.

$|V_0|$ is above a material dependent threshold value, charged particles are emitted off the cathode and flow toward the anode (Ref. 2). In the case of field emission, the only one considered here, the large transverse electric field at the cathode surface causes plasma formation from which electrons ($V_0 > 0$) or positive ions ($V_0 < 0$) are emitted. We consider only the case of electron emission.

Electrons flowing in the A-K gap considerably modify the field equilibrium. The special case of space-charge-limited emission (Ref. 3) occurs when the plasma density near the cathode is such that the surface value of the transverse electric field is reduced to zero. At this point, the emitted electron current density cannot increase and the transmission line is said to be space-charge limited. Experimental evidence suggests that electron flow in MITLs is space-charge limited (Ref. 4); hence, it is the only type of flow considered in this report.

Figure 1b depicts the electron flow for sufficiently low voltage and electron current. Electrons flow directly from cathode to anode. This type of flow is known as Child-Langmuir flow (Ref. 3) and is characterized by a current density that is proportional to $|V_0|^{3/2}$. For higher voltages the electron current increases and the associated magnetic field becomes strong enough to bend trajectories toward the cathode. At a critical current I_{cr} (typically kiloamps), the self-magnetic field prevents electrons from reaching the anode (Ref. 5). In this case, electrons are cut off from the anode and the transmission line is said to be magnetically insulated. Electron cutoff is the crux of magnetic insulation; it permits the sustenance of high voltage across vacuum gaps by delaying breakdown due to plasma generation via electron bombardment of the anode. Increasing the electron current above I_{cr} will cause the charge flow to be pinched closer to the cathode. In Figs. 1c and 1d, we show two types of equilibria, out of many possible, corresponding to insulated flow. The currents required to maintain these flow patterns are denoted I_a , I_e , and I_c , for anode current, electron current, and cathode current, respectively. In each case, electrons drift parallel to the cathode, as a result of crossed electric and magnetic fields, in a sheath that extends out to a radius denoted r_e ; however, the two equilibria are distinguished by different

particle orbits. In Fig. 1c, the orbits are laminar; a special case of this equilibrium is known as relativistic Brillouin flow (RBF) and is characterized by all electrons having the same constant Hamiltonian and canonical momentum (Ref. 6). Figure 1d depicts the more general, and more probable, case of cycloidal-type orbits. Theory shows that orbit type does not significantly affect transmission line current (Ref. 5).

Many theories of varying degrees of complexity and using different particle equilibria have been used to model MITL flow (Refs. 4, 6-8). Because of its relative simplicity, RBF equilibrium is used to derive a dispersion relation for the MILO. The following is an outline of results presented in Ref. 6.

As discussed above, electrons in RBF equilibrium drift parallel to the cathode (along equipotential lines) in laminar orbits with a velocity determined by crossed electric and magnetic fields. Figure 1c represents the configuration under consideration. In the following analysis, the cathode is assumed to be grounded and the anode has been charged to a voltage $V_0 > 0$. Let $\phi(r)$ and $A_z(r)$ respectively represent the equilibrium electric and magnetic potentials in cylindrical coordinates (r, θ, z) . The corresponding fields are given by $E_r = -d\phi/dr$ and $B_\theta = -dA_z/dr$. Let H represent the Hamiltonian and P_z the canonical momentum for electrons in this system. Then

$$P_z = \gamma m v_z - \frac{e}{c} A_z \quad (1)$$

and

$$H = \left[m^2 c^4 + c^2 \left(P_z + \frac{e}{c} A_z \right)^2 \right]^{1/2} - e\phi \quad (2)$$

where v_z represents the r dependent drift velocity, c the speed of light, m the electron mass, $-e$ the electron charge, and $\gamma = 1/(1-v^2/c^2)^{1/2}$. Because the fields are time independent, H and P_z are constants of the motion. Using boundary conditions $\phi(r_c) = A_z(r_c) = 0$ and conservation of energy, it is easy to show, using Eqs. 1 and 2, that $P_z = 0$. Therefore

$$\gamma m v_z = \frac{e}{c} A_z \quad (3)$$

and

$$(\gamma-1)mc^2 = e\phi \quad (4)$$

A differential equation for $\gamma(r)$ can be obtained by minimizing the action integral

$$S = \int dV L \left(\frac{d\phi}{dr}, \frac{dA_z}{dr}, r \right) \quad (5)$$

where dV represents a volume element and L the Lagrangian density of the fields. The latter is given by

$$L = \frac{1}{8\pi} \left[\left(\frac{d\phi}{dr} \right)^2 - \left(\frac{dA_z}{dr} \right)^2 \right] \quad (6)$$

The potentials are eliminated from Eq. 6 using Eqs. 3 and 4. Then, the action integral is minimized if L satisfies the following Euler equation

$$\frac{d}{dr} \frac{\partial L}{\partial \gamma'} - \frac{\partial L}{\partial \gamma} = 0 \quad (7)$$

where $\gamma' = d\gamma/dr$. Making the transformation $\rho = \ln[(r/r_c)^A]$ and performing the necessary algebra gives the following equation for γ

$$\frac{d^2\gamma}{d\rho^2} = \frac{\gamma}{\gamma^2-1} \left(\frac{d\gamma}{d\rho} \right)^2 \quad (8)$$

where A is a constant to be evaluated below. The solution of Eq. 8 is

$$\gamma = \cosh(\rho) \quad (9)$$

as is easily demonstrated by direct substitution. The following expressions result from Eq. 9:

$$v_z = c \tanh(\rho) \quad (10)$$

$$e\phi = mc^2[\cosh(\rho) - 1] \quad (11)$$

$$eA_z = mc^2 \sinh(\rho) \quad (12)$$

$$E_r = - \frac{mc^2}{e} \frac{A}{r} \sinh(\rho) \quad (13)$$

$$B_\theta = - \frac{mc^2}{e} \frac{A}{r} \cosh(\rho) \quad (14)$$

Note that on the cathode surface ($\rho = 0$) $E_r = 0$; thus, RBF corresponds to space-charge-limited emission. Furthermore, dividing Eq. 13 by Eq. 14 and comparing the result to Eq. 10, it is easy to see that the electron drift velocity is completely determined by the equilibrium fields. Note that the electron velocity is sheared, varying from 0 at the cathode to some maximum at the sheath radius r_e . This is an important property of RBF because it allows the MILO to operate over a wide range of voltages.

Using Eq. 13 for E_r in the integral form of Gauss' law yields

$$n = \frac{mc^2}{4\pi e^2} \left(\frac{A}{r}\right)^2 \cosh(\rho) \quad (15)$$

for the electron density of the flow. The square of the corresponding plasma frequency is given by

$$\omega_p^2 = \frac{4\pi e^2 n}{m} = \left(\frac{cA}{r}\right)^2 \cosh(\rho) \quad (16)$$

and will represent space-charge effects in the MILO stability analysis.

Because the magnetic field is nonzero on the cathode, a current must flow in this region. For a perfect conductor it will flow on the cathode surface (boundary). By conservation of current, I_c , I_e , and I_a (defined above) must satisfy the relation

$$I_a = I_c + I_e \quad (17)$$

To derive an expression for I_a , we first use Ampere's law to obtain $B_\theta = 2I_a/cr$ for the magnetic field in the region between the space charge and anode. Then, we equate this expression with Eq. 14 at $r = r_e$ and solve for I_a . The result is

$$I_a = AI_\alpha \gamma_e \quad (18)$$

where $I_\alpha = mc^3/2e = 8.5 \text{ kA}$.

The cathode current is obtained simply by evaluating Eq. 14 at $r = r_c$ and noting that $\cosh(\rho_c) = 1$. Thus,

$$I_c = AI_\alpha \quad (19)$$

Using Eqs. 18 and 19 in Eq. 17 yields

$$I_e = AI_\alpha (\gamma_e - 1) \quad (20)$$

for the space-charge current.

Expression 18 can be used to define the constant A because I_a and γ_e are often assumed to be known. Another useful expression for A is obtained by evaluating Eq. 9 at $r = r_e$ and solving for A . The result is

$$A = \frac{1}{2} \frac{\ln\left(\frac{1+\beta_e}{1-\beta_e}\right)}{\ln\left(\frac{r_e}{r_c}\right)} \quad (21)$$

where $\beta_e = v_{ze}/c = (\gamma_e^2 - 1)^{1/2}/\gamma_e$. Parameters having subscript e denote variables evaluated at the edge of the charge sheath; for example, $\gamma_e = \gamma(r_e)$. When $r_e = r_a$, the flow is said to be saturated.

In terms of the above parameters, the transmission line current (I_{cr}) necessary to cut off electron flow to the anode is given by (Ref. 6)

$$I_{cr} = \frac{I_\alpha \beta_a \gamma_a}{\ln\left(\frac{r_a}{r_c}\right)} \quad (22)$$

where the subscript a indicates a quantity evaluated at the anode. At this critical current, electron trajectories are tangent to the anode.

Upon examination of Eqs. 9-21, it is clear that knowledge of any pair of parameters (γ_e, r_e) , (β_e, r_e) , (I_e, I_c) , (I_e, I_a) , or (I_c, I_a) completely determines RBF equilibrium. The last pair (I_c, I_a) can be determined experimentally.

The above theory of RBF has been used successfully to predict total current in MITL experiments (Ref. 6) with good agreement for voltages up to 1.4 MV.

2.2 SPACE-CHARGE WAVES

Consider a region of plasma (neutral or nonneutral) in equilibrium. If ions are present, they are assumed to be stationary. When a region of plasma is perturbed, associated electrons respond with oscillations at a frequency proportional to ω_p , the plasma frequency defined in Eq. 16. Whether or not the disturbance propagates depends critically on many factors, including the electron velocity distribution, the temperature, and the presence of boundaries (Ref. 10). When a disturbance propagates, it is known as a space-charge wave. Because they are manifest as a movement of mass, space-charge waves cannot travel faster than the speed of light; hence, they are often called slow waves.

To better understand space-charge waves, we examine the dispersion relation for a simple problem. Consider a coaxial waveguide, shown in Fig. 1a, with the space between electrodes filled with a uniform density electron beam drifting with velocity $\vec{v} = v_b \hat{k}$ and immersed in an infinite solenoidal magnetic field. The infinite magnetic field precludes transverse electron motion; therefore, only longitudinal disturbances are considered. The dispersion relation for TM_{0m} (transverse magnetic) modes ($E_r, E_z, B_\theta \neq 0$ and $E_\theta, B_r, B_z = 0$) supported by this system is given in dimensionless form (Ref. 9).

$$\left(\omega - \beta_b k\right)^2 \left(\omega^2 - k^2 - q_{0m}^2\right) - \frac{\omega_p^2}{\gamma_b} \left(\omega^2 - k^2\right) = 0 \quad (23)$$

where $\beta_b = v_b/c$, $\gamma_b = 1/(1-\beta_b^2)^{1/2}$, $\omega' = \omega r_c/c$, $k' = k_0 r_c$, k_0 is the mode wave number, $\omega_p' = \omega_p r_c/c$, q_{0m} represents the m th zero of the expression $J_0(Z)Y_0(\lambda Z) - J_0(\lambda Z)Y_0(Z)$, and m represents the radial mode number. Here J_0 and Y_0 respectively denote zero order Bessel's functions of the first and second kind. Setting $\omega_p' = 0$ in Eq. 23 gives the classical dispersion relation for TM_{0m} modes in a coaxial waveguide. The term in Eq. 23 containing ω_p' represents the effect of space charge.

Figure 2 is a plot of a generic solution to Eq. 23. Solid lines represent solutions. Broken lines indicate beam velocity and speed of light. The light line separates fast and slow waves; that is, waves having phase velocity greater than or less than the speed of light, respectively. Although there are an infinite number of them, only the first ($m = 1$) electromagnetic mode is shown. It asymptotically approaches the light line as $k' \rightarrow \infty$, but never crosses it. Setting $k' = 0$ in Eq. 23 shows that the TM_{0m} modes are cut off (no longer propagate) at a frequency ω_c given by $\omega_c = (q_{0m}^2 + \omega_p'^2 / \gamma_b^3)^{1/2}$. The presence of electrons has increased the cutoff frequency of all modes. In general, there are two space-charge waves associated with a monoenergetic beam of electrons. In Fig. 2, these are represented by the solid lines straddling the beam line. Although each mode has phase velocity less than c , they are often referred to as fast and slow space-charge waves depending on whether the associated phase velocity ω'/k' is greater than or less than v_b , respectively.

The position of space-charge modes relative to the beam line, and their corresponding shape, is sensitive to electron density and velocity. For example, changing v_b changes the slope of the beam line and corresponding space-charge modes.

More than two space-charge waves exist in electron flows having a nonuniform velocity distribution (Ref. 10), of which RBF is an example. In particular, such systems support a single fast space-charge wave and a continuum of slow space-charge waves with phase velocities in the range $v_1 < v_{ph} < v_b$ where v_1 represents the slowest electron velocity. Depending on the value of v_1 , a single slow wave mode with $v_{ph} < v_1$ may exist. An upcoming section shows that

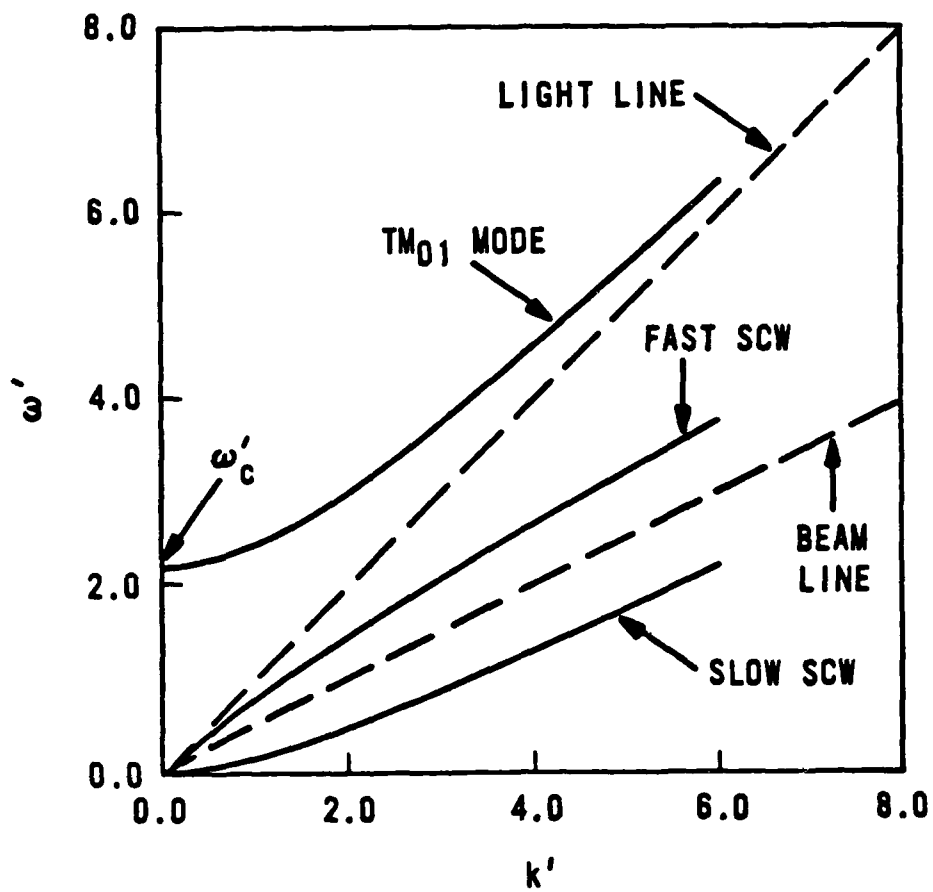


Figure 2. Dispersion diagram for TM_{0n} waves in a coaxial transmission line containing a monoenergetic electron beam.

the MILO instability is a result of coupling between space-charge waves with slow electromagnetic waves.

2.3 PERIODIC STRUCTURES AND SLOW ELECTROMAGNETIC WAVES

An important property of periodic structures is that they support slow electromagnetic waves; that is, the associated phase velocity is less than c . Thus, slow waves can be amplified by coupling them to collective charge flows. When the wave-phase velocity and charge-drift velocity are correctly matched, wave amplification occurs at the expense of particle energy. This is the method used to generate microwaves in devices such as magnetrons, traveling wave tubes (TWT), and backward wave oscillators (BWO), for example (Refs. 11-13). Because a MILO operates on the same principle, we will review some important results concerning slow-wave propagation in periodic structures.

Figure 3 is a schematic of a hollow, cylindrical, periodic waveguide. The waveguide wall is comprised of alternating vanes and slots having widths w_v and w_s , respectively. The structure period (z_0) is given by $z_0 = w_v + w_s$. The inner wall radius is r_i , and slots extend to a depth d , giving an outer wall radius $r_o = r_i + d$.

A qualitative picture of the dispersion diagram for TM_{0m} modes in this structure can be obtained using Floquet's theorem (Ref. 13). Floquet's theorem requires that field values at points separated by a structure period z_0 can differ only by a phase factor. Let F represent any field component associated with a TM_{0m} wave propagating in the waveguide shown in Fig. 3. Then, according to Floquet's theorem, F must have the form

$$F = \sum_{n=-\infty}^{\infty} F_n(r) \exp[i(k_n z - \omega t)] \quad (24)$$

where $k_n = k_0 + nh_0$, $h_0 = 2\pi/z_0$, and k_0 and ω represent mode wave number and frequency, respectively. The individual terms in Eq. 24 are sometimes referred to as Hartree components (spatial harmonics) of the field.

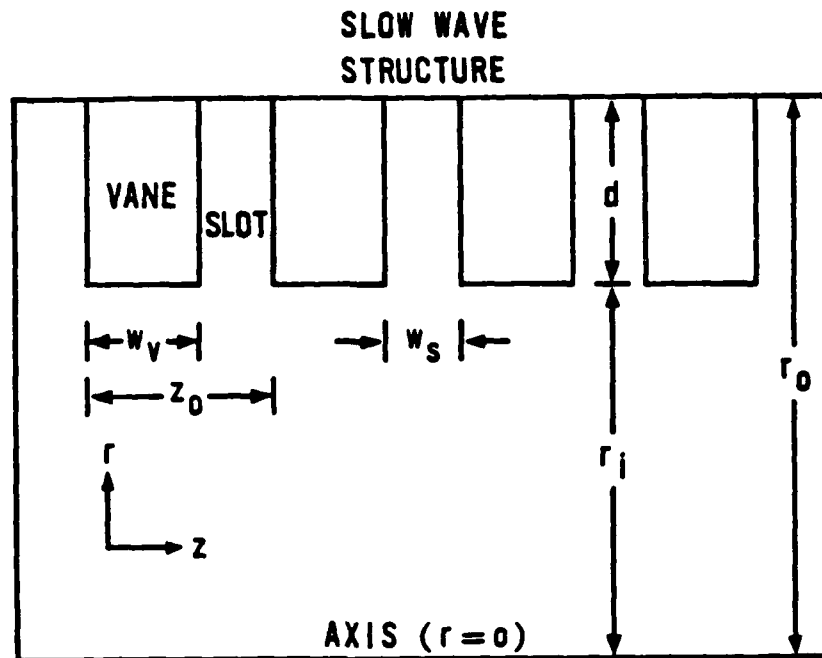


Figure 3. Schematic of a hollow, cylindrical, slow waveguide.

The expansion in Eq. 24 represents a superposition of an infinite number of standard waveguide modes, each shifted in wave number by an amount $2\pi n/z_0$. The resulting system of forward and backward traveling harmonics determines the character of all fundamental modes. Figure 4 represents the dispersion diagram of TM_{0m} waves supported by the structure shown in Fig. 3 with $d/r_i \ll 1$ (Ref. 13). Broken lines represent shifted standard waveguide modes; that is, those obtained without the corrugated wall. Solid lines are a superposition of the latter, and represent modes that will propagate in the periodic structure.

To electromagnetic waves, the periodic structure appears as a series of impedance discontinuities with corresponding transmission and reflection coefficients. The form of the dispersion diagram basically depends on the relative phase of waves reflected or transmitted by these discontinuities. The latter determines the upper and lower frequency cutoff for a mode. In particular, for shallow slots a mode will be cut off when its wavelength is such that $\lambda_1/2 = w_s$ or

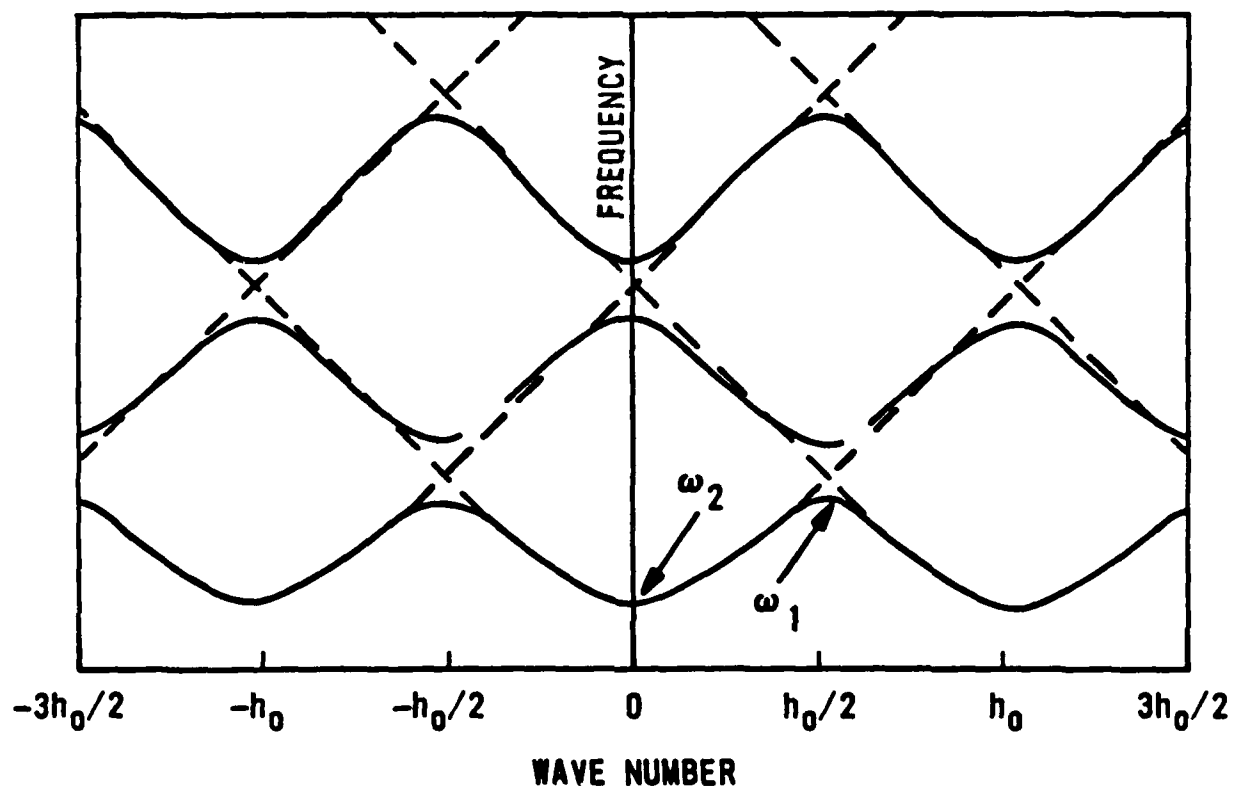


Figure 4. Dispersion diagram for TM_{0n} waves in a hollow, cylindrical, slow waveguide.

$\lambda_2/2 = r_i$. The first condition is realized when waves reflected by the slots are 180 deg out of phase with incoming waves. By analogy with magnetron theory, this mode is called the π -mode (Ref. 13). In this case, the electric field changes phase by 180 deg from slot to slot. The second condition corresponds to the standard waveguide cutoff condition. In Fig. 4 these points, exemplified by ω_1 and ω_2 , occur where $d\omega/dk_0 = 0$, that is, where the corresponding group velocity is zero.

Figure 4 is periodic with period h_0 , because the form of expansion in Eq. 24 is unchanged by the transformation $k_0 \rightarrow k_0 + mh_0$.

An important feature of Fig. 4 is the presence of slow electromagnetic waves (phase velocity less than c). Such modes can be amplified via an unstable interaction with drifting charge flows. In the MILO these modes are amplified via the unstable interaction with electrons in the magnetically insulated flow.

2.4 QUALITATIVE DESCRIPTION OF MILO OPERATION

Enough information is now available to put together a qualitative description of how the MILO operates in the linear regime in which the field perturbations are much weaker than the dc fields. Figure 5 is a superposition of Figs. 1c and 3, and represents a coaxial MILO in which the electron flow is laminar and magnetically insulated (RBF). From the previous discussion, the dispersion diagram for TM_{0m} modes is expected to consist of fast and slow electromagnetic waves in addition to space-charge waves. Velocity shear associated with the insulated flow will result in a continuum of slow space-charge waves having phase velocities in the range $0 < v_{ph} < v_e$, where the limits correspond to the minimum and maximum electron velocities in the flow. When the phase velocity of a TM_{0m} mode lies in this range, an instability is expected to occur. Electrons in this resonant layer always see a decelerating axial electric field. Consequently, field energy increases at the expense of particle energy.

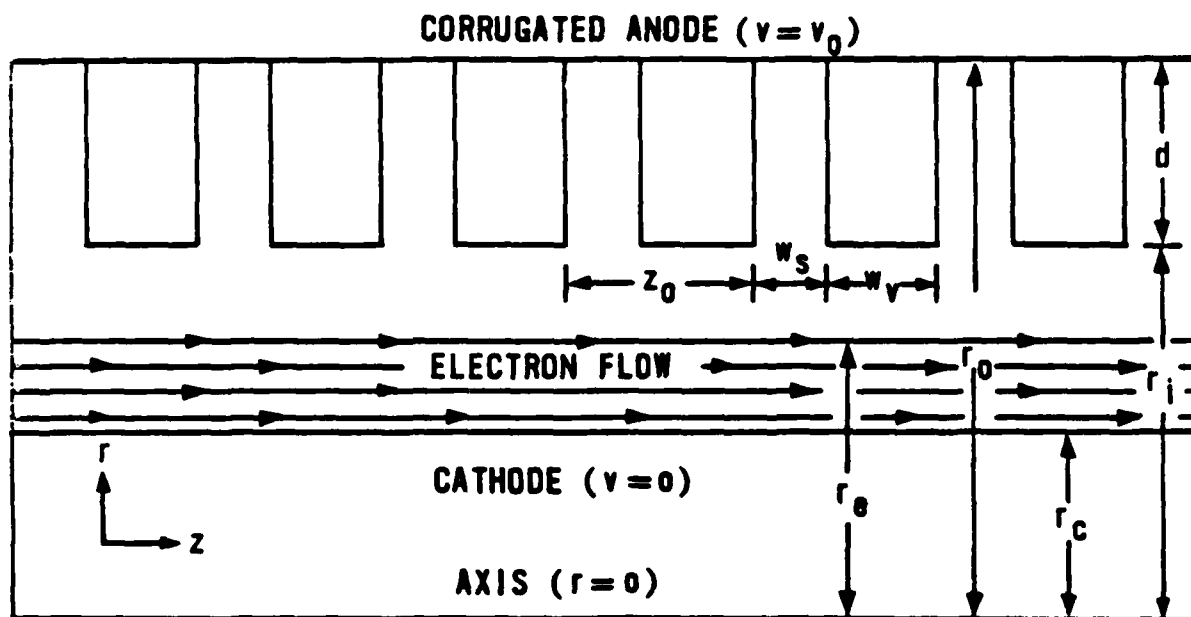


Figure 5. Schematic of a cylindrical MIO.

In succeeding sections, MILO dispersion relations are derived for several types of periodic structures and two different electron equilibria. Numerical results indicate that the qualitative description given above is correct in the linear regime.

3.0 MILO DISPERSION RELATION FOR THIN BEAMS

To obtain a preliminary understanding of MILO physics, we derive a dispersion relation for the simplest possible space-charge equilibrium. Assume that an infinitesimally thin annular beam of electrons with radius r_e drifts with velocity $\vec{v} = v_z \hat{k}$ parallel to and concentric with the center conductor of an infinitely long, cylindrically symmetric, periodic, coaxial transmission line (CTL). The cathode has constant radius r_c . The anode is a continuous, periodic structure with period z_0 and radius $r_a(z)$. The entire configuration is shown schematically in Fig. 6. In the figure, the parameter ϕ represents the angle between a tangent to the anode and the horizontal. It will be used later in the derivation of a key boundary condition.

Modeling the corrugated anode with a continuous periodic function has several advantages. Because we assume the anode is continuous with continuous first derivative, the problem consists of solving Maxwell's equations in two regions, one containing space charge and the other without. If we use the structure shown in Fig. 3 (square-wave anode), three regions are required: two corresponding to the space charge and vacuum in the A-K gap, and another for the vacuum in the slot region. An exact mathematical treatment of the latter problem would be quite difficult because the necessary matching conditions at the region interfaces are not easily implemented. Consequently, most analyses involving square-wave anodes assume the slot depth is very deep compared to its width (see Ref. 14, for example). This model ignores the slot E_r field (in cylindrical coordinates, for example) and precludes the existence of waves other than transverse electromagnetic (TEM) in the slot region. Furthermore, in cylindrical coordinates, analysis of coaxial structures with square-wave anodes produces formulae having singularities that strictly limit applicability. Therefore, to avoid these complications, we choose to model the corrugated anode with a continuous function having continuous first derivative.

Because all electrons are assumed to drift in the z direction, an E_z field component must be present for instability to occur. Hence, we consider only TM waves for which E_r , E_z , and B_θ are nonzero and E_θ , B_r , and B_z equal zero. In addition, it is assumed that asymmetries giving rise to asymmetric modes

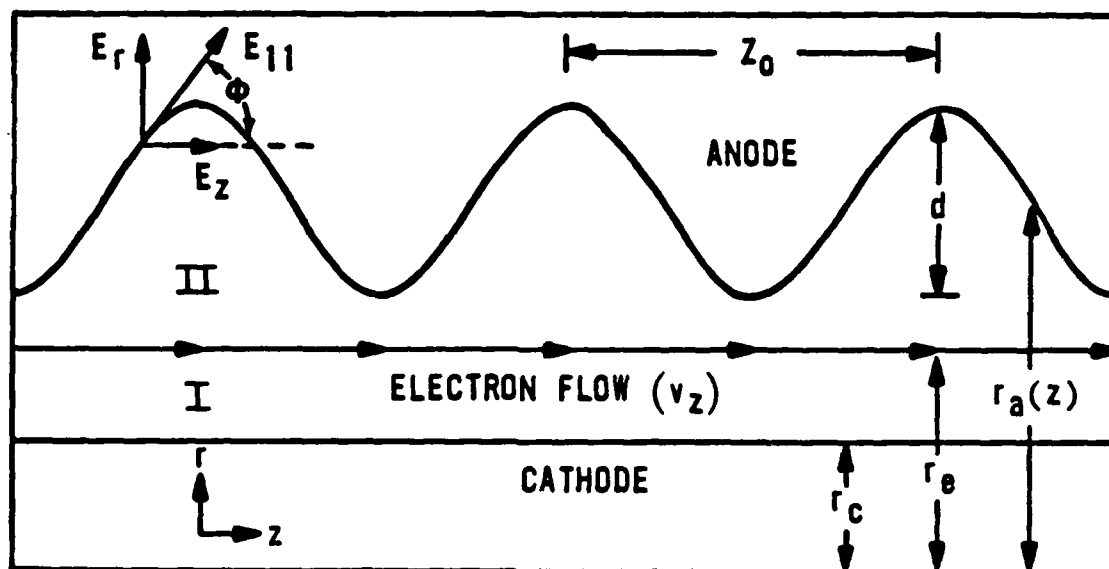


Figure 6. Model of MILO used in the linear theory.

do not exist; that is, quantities are independent of the azimuthal coordinate θ . Analogous to classical waveguide theory, these waves are referred to as TM_{0m} modes, where m refers to the radial mode number; the important difference is that periodic CTLs support slow electromagnetic waves.

The above space-charge equilibrium is not possible without the use of a strong (infinite), externally applied, solenoidal magnetic field to guide electrons through the CTL. The existence of such a field is assumed throughout the analysis, and allows us to neglect transverse electron motion.

A thin monoenergetic beam of electrons is considerably different from the magnetically insulated flow described in Section 2.1. Its use is justified by the fact that in the linear regime a thin sheath of electrons nearest the anode will interact strongest with the fundamental TM mode because it has a radial maximum in this region. Furthermore, as long as the radial electromagnetic wavelength is much longer than the charge sheath thickness, the latter will not be important. We expect this to be the case because, by analogy with classical waveguide theory, the wavelength of the fundamental mode will be approximately $2\max(r_a - r_c)$.

Implicit in the above discussion is the assumption that the electron equilibrium is unaffected by the presence of a periodic anode. This is certainly true for very shallow slots ($d < w_s$), and we assume it is approximately true for deep slots ($d > w_s$). In the case of deep slots, the dc electric field will bend significantly near the slot entrances, creating an electric field component parallel to the cathode in addition to the usual radial electric field. The parallel field component perturbs the transmission line equilibrium, but its magnitude decreases toward the cathode where it is zero. Thus, in the A-K gap where electrons are confined, the total electric field is approximately radial, and the electron motion is approximately laminar. This is confirmed for RBF in Sec. 6.

The thin-beam approximation was used to derive a dispersion relation because associated perturbed field equations have simple analytic solutions; and in the limit of zero cathode radius and shallow slots, the theory can be validated with an existing theory of backward-wave oscillators (Ref. 11).

As is shown in Fig. 6, the electron flow divides the problem into two distinct vacuum regions $r_c \leq r < r_e$ and $r_e < r \leq r_a(z)$. To derive a dispersion relation for this system, expand the fluid equations for electron flow and Maxwell's equations for E_r , E_z , and B_θ about the thin-beam equilibrium. All dependent variables can be written in terms of the expansion coefficients of the perturbed E_z field. Solutions for the perturbed E_z are obtained in regions I and II and matched at the space-charge interface. The boundary condition for the tangential component of the perturbed total electric field at the anode will lead to a dispersion relation.

Proceed by considering first the region containing space charge. Corresponding equations for the vacuum regions are easily obtained by setting the electron plasma frequency equal to zero.

With the above assumptions, Maxwell's equations in cylindrical coordinates (r, θ, z) become

$$\frac{\partial E_r}{\partial z} - \frac{\partial E_z}{\partial r} = -\frac{1}{c} \frac{\partial B_\theta}{\partial t} \quad (25)$$

$$-\frac{\partial B_{\theta}}{\partial z} = \frac{1}{c} \frac{\partial E_r}{\partial t} \quad (26)$$

$$\frac{1}{r} \frac{\partial}{\partial r} r B_{\theta} = \frac{4\pi}{c} J_z + \frac{1}{c} \frac{\partial E_z}{\partial t} \quad (27)$$

where J_z represents the electron current density. The equations describing the electron flow are

$$\left(\frac{\partial}{\partial t} + v_z \frac{\partial}{\partial z} \right) p_z = -e E_z \quad (28)$$

$$\frac{\partial n}{\partial t} + \frac{\partial}{\partial z} n v_z = 0 \quad (29)$$

where $p_z = \gamma m v_z$ is the axial component of relativistic momentum, $\gamma = 1/(1-v_z^2/c^2)^{1/2}$, n the electron density, and $\partial/\partial t + v_z \partial/\partial z$ represents the convective derivative (d/dt).

We now perturb the system about its equilibrium. Let F temporarily represent any one of the quantities E_r , E_z , B_{θ} , n , or v_z . For small perturbations we assume that $F = F_0 + F_1$ ($F_1 \ll F_0$) where 0 and 1 denote equilibrium and perturbed quantities, respectively. The perturbation F_1 is assumed to have the form

$$F_1 = \sum_{n=-\infty}^{\infty} F_n(r) \exp[i(k_n z - \omega t)] \quad (30)$$

where $k_n = k_0 + n h_0$ and $h_0 = 2\pi/z_0$ (Floquet's theorem). The parameters k_0 and ω represent mode wave number and angular frequency respectively. Substituting an expansion of the form just described for each of the dependent variables in Eqs. 25-29 yields to first order in the perturbed quantities:

$$i k_n E_{rn} - \frac{dE_{zn}}{dr} = i \frac{\omega}{c} B_{\theta n} \quad (31)$$

$$k_n B_{\theta n} = \frac{\omega}{c} E_{rn} \quad (32)$$

$$\frac{1}{r} \frac{d}{dr} r B_{\theta n} = \frac{4\pi}{c} J_{zn} - i \frac{\omega}{c} E_{zn} \quad (33)$$

$$i\Omega_n p_{zn} = eE_{zn} \quad (34)$$

$$\Omega_n n_n - n_0 v_{zn} k_n = 0 \quad (35)$$

where $\Omega_n = \omega - v_{z0} k_n$ represents the velocity shifted frequency. To obtain Eqs. 34 and 35, we have assumed that, because the structure under consideration is infinitely long, all equilibrium quantities are independent of z .

The thin-beam current density is given by $J_z = -en v_{zn} \delta(r-r_e)$ where δ is the Dirac delta-function and η is a normalization constant determined by requiring

$-|I_e| = 2\pi \int_{r_c}^{r_a} dr r J_z$. The parameter I_e represents total electron current. The integration is trivial and yields $\eta = |I_e| / (2\pi r_e n_0 v_{z0})$. The n th component of J_{z1} can now be written as

$$J_{zn} = -en(n_0 v_{zn} + n_n v_{z0}) \delta(r-r_e) \quad (36)$$

The n th component of p_{z1} is given by $p_{zn} = m(\gamma_n v_{z0} + \gamma_0 v_{zn})$. To obtain γ_n , expand $\gamma(v_z)$ in a Taylor series about v_{z0} . To first order this yields

$$\gamma_0 + \gamma_1 = \gamma(v_{z0}) + v_{z1} \left. \frac{d\gamma}{dv_z} \right|_{v_z = v_{z0}}$$

Because $\gamma_0 = \gamma(v_{z0})$, we identify the perturbed relativistic factor γ_1 with

$$v_{z1} \left. \frac{d\gamma}{dv_z} \right|_{v_z = v_{z0}}$$

Since $d\gamma/dv_z = v_z \gamma^3 / c^2$, we have $\gamma_n = v_{z0} \gamma_0^3 v_{zn} / c^2$ and $p_{zn} = m \gamma_0^3 v_{zn}$. Substituting the latter expression for p_{zn} into Eq. 34 yields

$$v_{zn} = -i \frac{e E_{zn}}{m \gamma_0^3 \Omega_n} \quad (37)$$

Solving Eq. 35 for n_n yields

$$n_n = \frac{n_0 k_n v_{zn}}{\Omega_n} \quad (38)$$

Substituting Eqs. 37 and 38 into Eq. 36 yields

$$J_{zn} = in \frac{e^2 n_0}{m \gamma_0^3} \frac{\omega E_{zn}}{\Omega_n^2} \delta(r-r_e) \quad (39)$$

Using Eq. 32 to eliminate $B_{\theta n}$ in Eq. 31 and solving for E_{rn} yields

$$E_{rn} = i \frac{k_n}{r_n^2} \frac{dE_{zn}}{dr} \quad (40)$$

where $r_n^2 = \omega^2/c^2 - k_n^2$. Using Eq. 32 to eliminate E_{rn} in Eq. 40 yields

$$B_{\theta n} = i \frac{\omega/c}{r_n^2} \frac{dE_{zn}}{dr} \quad (41)$$

An equation for E_{zn} is obtained by substituting Eqs. 39 and 41 for J_{zn} and $B_{\theta n}$, respectively, into Eq. 33. The substitution yields

$$\left(\frac{1}{r} \frac{d}{dr} r \frac{d}{dr} + r_n^2 \right) E_{zn} = \frac{2\alpha}{\pi r_e} \frac{r_n^2 c^2}{\Omega_n^2} E_{zn} \delta(r-r_e) \quad (42)$$

where $\alpha = \pi |I_e| / (\gamma_0^2 I_A)$, $I_A = mc^3 \gamma_0 \beta_{z0} / e$, and $\beta_{z0} = v_{z0}/c$. I_A represents the Alfven current (Ref. 15) and is equal to $17.1 \gamma_0 \beta_{z0}$ kA. The Alfven limit is the maximum amount of current that can be transported in a beam of electrons. The parameter α governs the effect that space charge has on the dispersion relation.

Setting $\alpha = 0$ in Eq. 42 yields the following equation for E_{zn} in each of the vacuum regions.

$$\left(\frac{1}{r} \frac{d}{dr} r \frac{d}{dr} + r_n^2 \right) E_{zn} = 0 \quad (43)$$

Relations 40 and 41 for E_{rn} and $B_{\theta n}$ remain valid in the vacuum regions because they are independent of space-charge parameters.

We now use Eqs. 40-43 and appropriate boundary conditions to obtain a dispersion relation for TM_{0m} waves supported by the system shown in Fig. 6.

Equation 43 is Bessel's equation (Ref. 16) of order zero. The most general vacuum solution is

$$E_{zn}(r) = A_n J_0(r_n r) + B_n Y_0(r_n r) \quad (44)$$

where J_0 and Y_0 represent zeroth order Bessel functions of the 1st and 2nd kind, respectively. Because the origin is excluded from region I, Eq. 44 applies to both vacuum regions, albeit with different coefficients. The latter are determined using boundary and matching conditions for the total axial field E_{z1} .

At the cathode we have $E_{z1}(r_c) = 0$ for all z . Because the exponential functions in Eq. 30 expansion are linearly independent, we must have $E_{zn} = 0$; that is, the coefficients must vanish independently. Applied to the region I solution, this requires that $B_n^I Y_0(r_n r_c) = -A_n^I J_0(r_n r_c)$, or

$$E_{zn}^I(r) = A_n^* [Y_0(r_n r_c) J_0(r_n r)] - J_0(r_n r_c) Y(r_n r) \quad (45)$$

In Eq. 45, we have renormalized A_n^I such that $A_n^I = Y_0(r_n r_c) A_n^*$. Expression 44 with superscript II will be used for the solution in region II.

The coefficients A_n^{II} and B_n^{II} can be solved for in terms of A_n^* by matching the vacuum solutions at $r = r_e$. A valid solution must be continuous across the space-charge interface. Thus, we require

$$E_{zn}^I(r_e) = E_{zn}^{II}(r_e) \quad (46)$$

To obtain a second condition, multiply Eq. 42 by rdr and integrate from $r_e - \epsilon$ to $r_e + \epsilon$ with $\epsilon/r_e \ll 1$. The result is

$$r \frac{d}{dr} E_{zn} \bigg|_{r_e - \epsilon}^{r_e + \epsilon} + \Gamma_n^2 \int_{r_e - \epsilon}^{r_e + \epsilon} dr r E_{zn} = \frac{2\alpha}{\pi} \frac{\Gamma_n^2 c^2}{\Omega_n^2} E_{zn}(r_e) \quad (47)$$

Letting ϵ go to zero in Eq. 47 yields

$$\left. \frac{dE_{zn}^{II}}{dr} \right|_{r=r_e} - \left. \frac{dE_{zn}^I}{dr} \right|_{r=r_e} = \frac{2\alpha}{\pi r_e} \frac{\Gamma_n^2 c^2}{\Omega_n^2} E_{zn}^I(r_e) \quad (48)$$

where we have used the fact that E_{zn} is continuous, $E_{zn}(r_e + \epsilon) = E_{zn}^{II}$, and $E_{zn}(r_e - \epsilon) = E_{zn}^I$.

Substituting the solutions in Eqs. 44 and 45 for E_{zn}^{II} and E_{zn}^I into Eqs. 46 and 48 yields

$$A_n^{II} J_0(\Gamma_n r_e) + B_n^{II} Y_0(\Gamma_n r_e) = F_n A_n^* \quad (49)$$

and

$$A_n^{II} J_1(\Gamma_n r_e) + B_n^{II} Y_1(\Gamma_n r_e) = \left(G_n - \frac{2\alpha}{\pi r_e} \frac{\Gamma_n^2 c^2}{\Omega_n^2} F_n \right) A_n^* \quad (50)$$

where

$$F_n = Y_0(\Gamma_n r_c) J_0(\Gamma_n r_e) - J_0(\Gamma_n r_c) Y_0(\Gamma_n r_e)$$

and

$$G_n = Y_0(\Gamma_n r_c) J_1(\Gamma_n r_e) - J_0(\Gamma_n r_c) Y_1(\Gamma_n r_e)$$

Solving Eqs. 49 and 50 for A_n^{II} and B_n^{II} yields

$$A_n^{II} = \left[Y_0(\Gamma_n r_c) - \alpha \frac{\Gamma_n^2 c^2}{\Omega_n^2} F_n Y_0(\Gamma_n r_e) \right] A_n^* \quad (51)$$

and

$$B_n^{II} = \left[-J_0(\Gamma_n r_c) + \alpha \frac{\Gamma_n^2 c^2}{\Omega_n^2} F_n J_0(\Gamma_n r_e) \right] A_n^* \quad (52)$$

We have simplified the expressions for A_n^{II} and B_n^{II} by using the Wronskian identity (Ref. 17) $J_1(r_n r_e) Y_0(r_n r_e) - J_0(r_n r_e) Y_1(r_n r_e) = 2/\pi r_n r_e$.

Using Eqs. 30, 44, 51 and 52, the solution for the total perturbed axial field in region II [$r_e \leq r \leq r_a(z)$] is given by

$$E_{z1}^{II}(r, z, t) = \sum_{n=-\infty}^{\infty} A_n^* \left\{ Y_0(r_n r_c) J_0(r_n r) - J_0(r_n r_c) Y_0(r_n r) \right. \\ \left. - \alpha \frac{r_n^2 c^2}{\Omega_n^2} F_n \left[Y_0(r_n r_e) J_0(r_n r) - J_0(r_n r_e) Y_0(r_n r) \right] \right\} \\ \times \exp[i(k_n z - \omega t)] \quad (53)$$

Similar expressions can be obtained for $E_{r1}^{II}(r, z, t)$ and $B_{\theta 1}^{II}(r, z, t)$ using Eqs. 30, 40, 41, 44, 51 and 52, but they are not needed for the remaining analysis.

Application of the electric field boundary condition at the anode wall leads to a dispersion relation. The component of the total field tangent to the anode surface must be zero for all z . In terms of the angle ϕ defined above, the boundary condition at the anode wall can be written as

$$E_{z1}^{II}[r_a(z), z, t] \cos(\phi) + E_{r1}^{II}[r_a(z), z, t] \sin(\phi) = 0 \quad (54)$$

Equation 54 is a crude form of the dispersion relation; however, it has the undesirable feature of explicit z dependence. Following Ref. 18, we convert Eq. 54 into an infinite system of homogeneous equations, and simultaneously eliminate z by multiplying by $\exp(-imh_0 z)$ and integrating from $-z_0/2$ to $z_0/2$. Dividing Eq. 54 by $\cos(\phi)$, we note that $\tan(\phi) = dr_a(z)/dz$. Substituting general expressions for E_{z1}^{II} and E_{r1}^{II} (using Eqs. 30 and 40) into the resulting equation, multiplying by $\exp(-imh_0 z)$, and integrating from $-z_0/2$ to $z_0/2$ yields

$$\sum_{n=-\infty}^{\infty} \int_{-z_0/2}^{z_0/2} dz \left\{ E_{zn}^{II}[r_a(z)] + i \frac{k_n}{r_n} \frac{dr_a(z)}{dz} \frac{dE_{zn}^{II}}{dr} \bigg|_{r=r_a(z)} \right\} \exp[i(n-m)h_0 z] = 0 \quad (55)$$

where the term $\exp[i(k_0 z - \omega t)]$ was factored out before the integration. Equation 55 can be simplified by noting that

$$\frac{dr_a(z)}{dz} \frac{dE_{zn}^{II}}{dr} \bigg|_{r=r_a(z)} = \frac{d}{dz} E_{zn}^{II}[r_a(z)] \quad (56)$$

Using Eq. 56, integrate the second term in Eq. 55 by parts to get

$$\begin{aligned} & \int_{-z_0/2}^{z_0/2} dz \frac{dr_a(z)}{dz} \frac{dE_{zn}^{II}}{dr} \bigg|_{r=r_a(z)} \exp[i(n-m)h_0 z] \\ &= \int_{-z_0/2}^{z_0/2} dz \left(\frac{d}{dz} E_{zn}^{II}[r_a(z)] \right) \exp[i(n-m)h_0 z] \\ &= E_{zn}^{II}[r_a(z)] \exp[i(n-m)h_0 z] \bigg|_{-z_0/2}^{z_0/2} \\ &\quad - i(n-m)h_0 \int_{-z_0/2}^{z_0/2} dz E_{zn}^{II}[r_a(z)] \exp[i(n-m)h_0 z] \end{aligned} \quad (57)$$

Note that, because $r_a(z)$ is periodic with period z_0 , the first term on the right-hand side of the second equal sign in Eq. 57 is zero. Substituting the result of Eq. 57 into Eq. 55 yields

$$\sum_{n=-\infty}^{\infty} \left[1 + \frac{h_0 k_n}{r_n^2} \right] \int_{-z_0/2}^{z_0/2} dz E_{zn}^{II}[r_a(z)] \exp[i(n-m)h_0 z] = 0 \quad (58)$$

Using Eq. 53 to obtain $E_{zn}^{II}[r_a(z)]$ and substituting the result into Eq. 58 yields an infinite system of homogeneous equations of the form

$$\sum_{n=-\infty}^{\infty} A_n D_{mn}(\omega, k_0) = 0 \quad (59)$$

We define the integral $I_{mn}(x)$ such that

$$I_{mn}(x) = \int_{-z_0/2}^{z_0/2} dz \{ Y_0(r_n x) J_0[r_n r_a(z)] - J_0(r_n x) Y_0[r_n r_a(z)] \} \exp[i(n-m)h_0 z] \quad (60)$$

The matrix elements $D_{mn}(\omega, k_0)$ are then given by

$$D_{mn}(\omega, k_0) = \left[r_n^2 + h_0 k_n(n-m) \right] \left[\Omega_n^2 I_{mn}(r_c) - \alpha c^2 r_n^2 F_n I_{mn}(r_e) \right] \quad (61)$$

To obtain Eq. 61, we renormalized A_n^* such that $A_n^* = A_n r_n^2 \Omega_n^2$. This avoids the possibility of singularities occurring in upcoming numerical work.

A dispersion relation for the configuration shown in Fig. 6 is obtained by requiring the existence of nontrivial solutions to the homogeneous system, Eq. 59. This is assured by setting the determinant of the coefficient matrix equal to zero. Thus, the desired dispersion relation is given by

$$\det[D(\omega, k_0)] = 0 \quad (62)$$

For a given k_0 , Eq. 62 determines the frequencies of all allowed transverse magnetic modes and space-charge waves supported by the system shown in

Fig. 6. The dispersion relation applies to any structure than can be modeled with a continuous periodic function having a continuous first derivative. The case $n=0$ in the above equations corresponds to ordinary waveguide analysis. In general, Eqs. 58 and 62 must be solved numerically because the D_{mn} are too complicated. The next section shows that accurate numerical solutions to Eq. 62 can be obtained for relatively small values of m and n .

4.0 NUMERICAL SOLUTION OF THE THIN BEAM DISPERSION RELATION

In this section, we investigate the numerical solution of Eq. 62 with coefficients in Eq. 61 for a variety of periodic transmission line geometries and space-charge parameters. For this purpose, a computer code called DISCODE was written to numerically calculate oscillation frequency and growth rate (for problems with space charge) associated with TM_{0n} modes supported in a given MILO structure.

The discussion is in two parts. Part 4.1 concerns the numerical solution of the analytic dispersion equation for the purpose of obtaining a preliminary understanding of MILO physics. Part 4.2 presents results from two-dimensional (2-D) particle simulations of the MILO for the purpose of making direct comparisons with, and establishing the validity of, the analytic theory.

4.1 NUMERICAL SOLUTION OF EQUATION 62

DISCODE is used to obtain dispersion diagrams for a coaxial MILO whose periodic anode varies sinusoidally in the axial direction (see Eq. A-1 and Fig. A-1). The results are separated into groups with and without space charge. In the latter case, electromagnetic modes can be investigated without complications arising from the presence of space charge. Furthermore, the electromagnetic part of the code can be validated by making direct comparisons with previous work involving hollow backward wave oscillators having shallow slots. For cases that include space charge, the dispersion relation solution consists of interacting electromagnetic and space-charge modes, and reveals the nature of the MILO instability.

4.1.1 DISCODE Algorithm

Given a wave number k_0 , DISCODE evaluates the matrix elements $D_{mn}(\omega, k_0)$, computes the associated determinant, and iteratively calculates the complex roots ω_i ($i=1,2,3,\dots$) of Eq. 62. The ω_i are calculated with a routine called CROOT (Ref. 19). CROOT uses Muller's method (Ref. 20), which is

based on Newton-Raphson iteration (Ref. 21), and can be used to find the roots of any equation in the form of Eq. 62.

Clearly, for numerical work, the series in Eq. 59 must be truncated at some finite value $|n| = N$. The matrix $D(\omega, k_0)$ is then $2N+1$ by $2N+1$, with indices m and n ranging from $-N$ to N in increments of 1. The value of N depends on the slot depth and width. The number of significant space harmonics contained in a slot increases with its size; therefore, N must increase in proportion to slot size. To obtain accurate numerical solutions, N was varied until the variation in ω_i was less than one percent. This accuracy was achieved with values of N in the range $2 \leq N \leq 4$ for the structures considered.

4.1.2 Numerical Solution Without Space Charge

Dispersion curves for TM_{0n} modes in the absence of space charge can easily be obtained from DISCODE by eliminating electron current and velocity from the dispersion equation. This is accomplished by setting $\alpha = 0$ and $v_{z0} = 0$ in Eq. 61. Without space charge, there is no instability; hence, the roots of Eq. 62 are real.

The first case we consider is that of a hollow, sinusoidally rippled waveguide. A benchmark exists for this geometry (Ref. 11) and we use it to validate DISCODE. The center conductor is removed from the coaxial dispersion equation by replacing $Y_0(r_n x)$ with 1 and $J_0(r_n x)$ with 0 in Eq. 60. This substitution will not yield correct results when $\alpha \neq 0$; in this case $I_{mn}(r_c)$ and F_n in Eq. 61 must be modified.

Figure 7 represents the numerical solution of Eq. 62 for a hollow rippled waveguide with parameters $r_0 = 1.3$ cm, $\epsilon = 0.077$, $d = 0.2$ cm, and $z_0 = 1.1$ cm. In this and succeeding examples, frequency and wavelength are normalized by r_0/c and r_0 , respectively. Shown in Fig. 7 are the first four electromagnetic modes ($TM_{01} - TM_{04}$) and the light line (straight line with slope one). The light line separates regions of fast and slow waves. The dispersion diagram is consistent with Fig. 4 and associated discussion. Furthermore, Fig. 7 is identical to Fig. 3 of Ref. 11. Therefore, the numerical

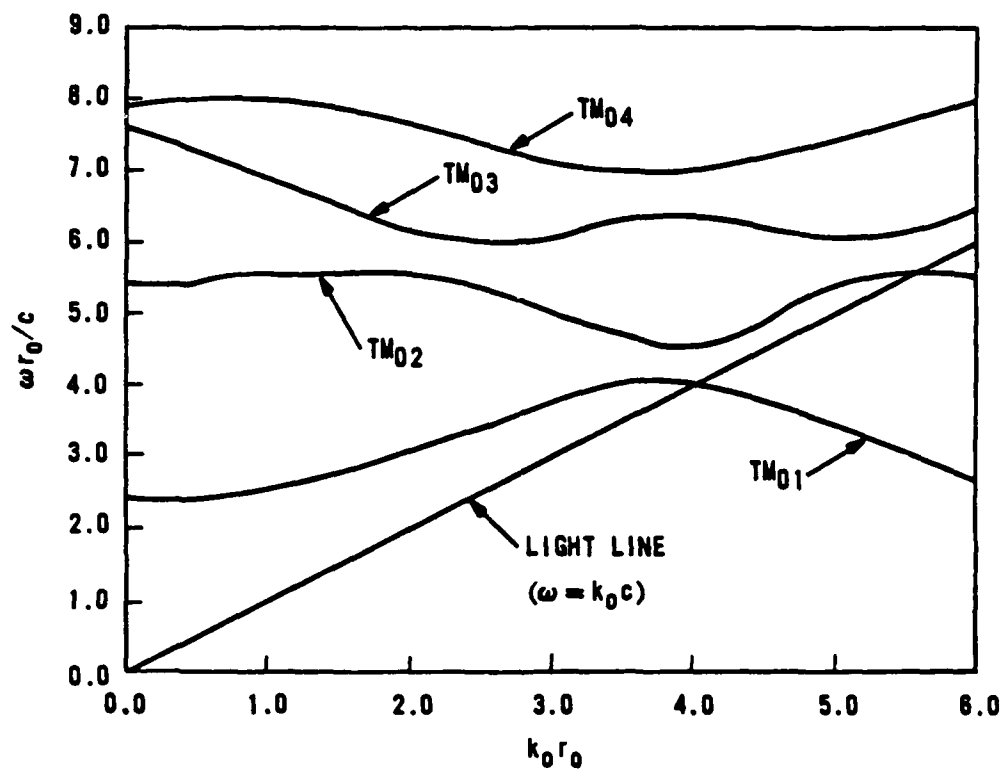


Figure 7. Dispersion diagram for TM_{0n} waves in a hollow, cylindrical, rippled waveguide.

solutions obtained with DISCODE should be accurate. Cases including space charge are validated below.

We now return to the case of coaxial geometry. Figure 8 represents the numerical solution of Eq. 62 for a coaxial MILO having inner conductor radius $r_c = 0.3$ cm, $r_0 = 1.3$ cm, $\epsilon = 0.077$, $d = 0.2$ cm, and $z_0 = 1.1$ cm. As required by theory, the dispersion diagram is clearly periodic with period $P = h_0 r_0 = 7.4$; that is, the normalized structure wave number. Unlike the previous example, the lowest order mode (TM_{01}) lies entirely on the slow-wave part of the diagram and includes zero frequency. This is characteristic of two conductor problems in which one conductor is rippled (corrugated) and can be understood in the following way. Suppose a zero frequency (dc) potential is applied across the gap in this system. Associated electric field lines must bend in the vicinity of the rippled anode such that they terminate normal to the conducting surface. Therefore, to satisfy boundary conditions, a static electric field in a periodic coaxial transmission line must have radial and axial components.

Figure 8 contains a series of passbands in which the frequency of propagating waves varies continuously with wave number. This is a result of using a nonreentrant geometry; that is, one that does not close in on itself. Electromagnetic fields in reentrant devices, such as the classical magnetron, are subject to closure conditions which lead to discrete modes. These modes are often characterized by the slot-to-slot phase difference of the dominant electric field component. For example, π -mode indicates a slot-to-slot field variation of π (180 deg).

Despite the fact that MILO modes are not discrete, it is often convenient to categorize them in terms of the slot-to-slot phase difference of the associated axial electric field. For example, in Fig. 8 the π -mode corresponds to $k_0 r_0 = P/2 = 3.7$. At this point the wave group velocity ($d\omega/dk_0$) is zero. Therefore, axial energy transport does not occur and the mode is said to be cut off.

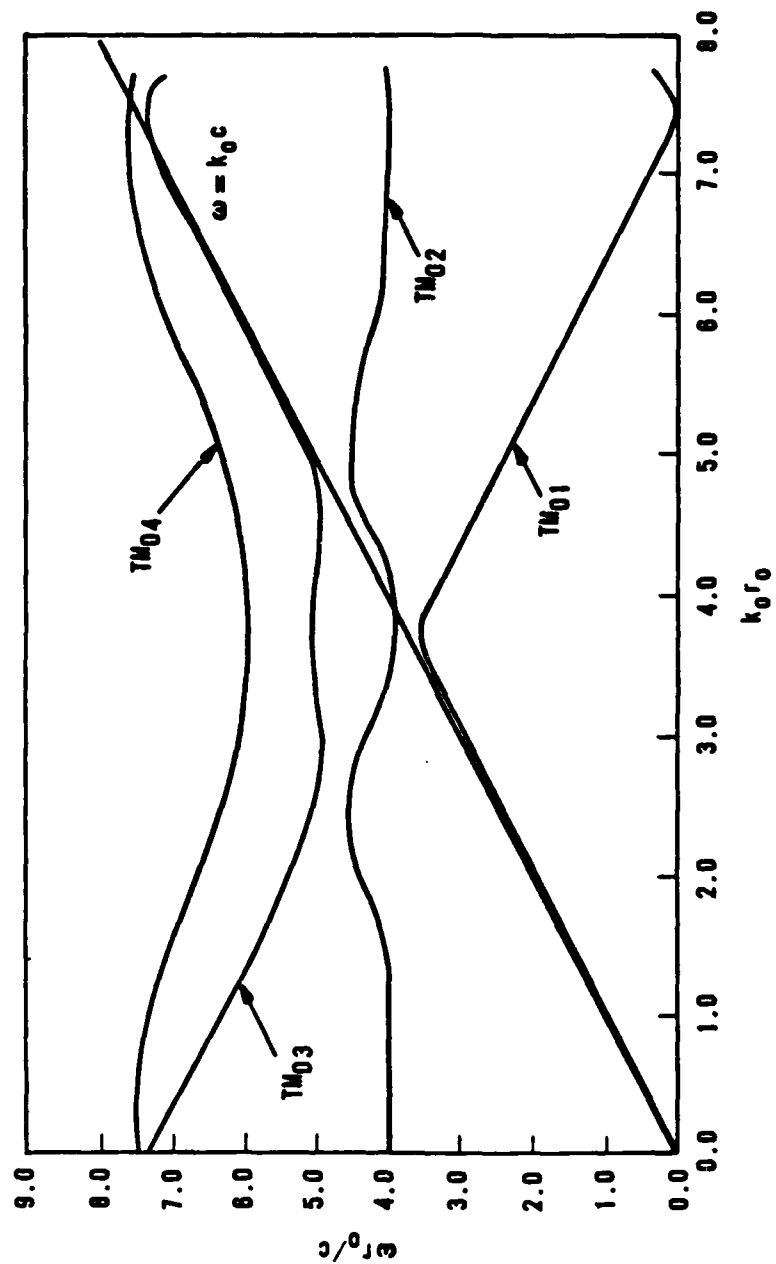


Figure 8. Dispersion diagram for TM_{0n} waves in a coaxial rippled waveguide.

The TM_{01} mode in Fig. 8 has the lowest cutoff frequency. By analogy with classical waveguide theory, this mode is expected to be dominant.

To verify the effect of changing structure period, we solve the dispersion equations for the previous geometry with the structure period increased by a factor of 2, now $z_0 = 2.2$ cm. In this case the dispersion diagram period should be 3.7. Figure 9 confirms this. In addition, note that the frequency of the TM_{01} π -mode is a factor of 2 less than in Fig. 8. This behavior is expected because, as discussed in Sec. 2.3, the upper frequency cutoff condition corresponds to half a free-space wavelength in a slot period when the slot depth is less than the slot width. In this case, the TM_{01} high-frequency cutoff is inversely proportional to structure period.

When the anode slots are deeper than their width, the high-frequency cutoff of the dominant mode is determined by the slot depth. Figure 10 is the dispersion diagram for the case in which $r_c = 0.3$ cm, $r_0 = 1.8$ cm, $\epsilon = 0.333$, $d = 1.2$ cm, $z_0 = 1.1$ cm, and $h_0 r_0 = 10.3$. A qualitative comparison with Fig. 8 (note that r_0 is different) shows the TM_{01} mode to be considerably flattened as a result of increasing the slot depth. The flattening of the TM_{01} mode becomes more pronounced as the slot depth increases. For very deep slots, think of a slot as a short-circuited transmission line in which a transverse electromagnetic (TEM) wave propagates. Because the electric field is maximum at the open end and zero at the closed end, the cutoff frequency corresponds to a quarter of a free-space wavelength in a slot. In any case, mode frequency decreases with increasing slot depth.

Having established the spectrum of TM_{0n} modes associated with the MILO in the absence of space charge, we now investigate how space charge modifies the dispersion relation solution.

4.1.3 Numerical Solution Including Space Charge

Before proceeding to the most general case of space charge flow in the rippled, coaxial guide, consider another benchmark problem.

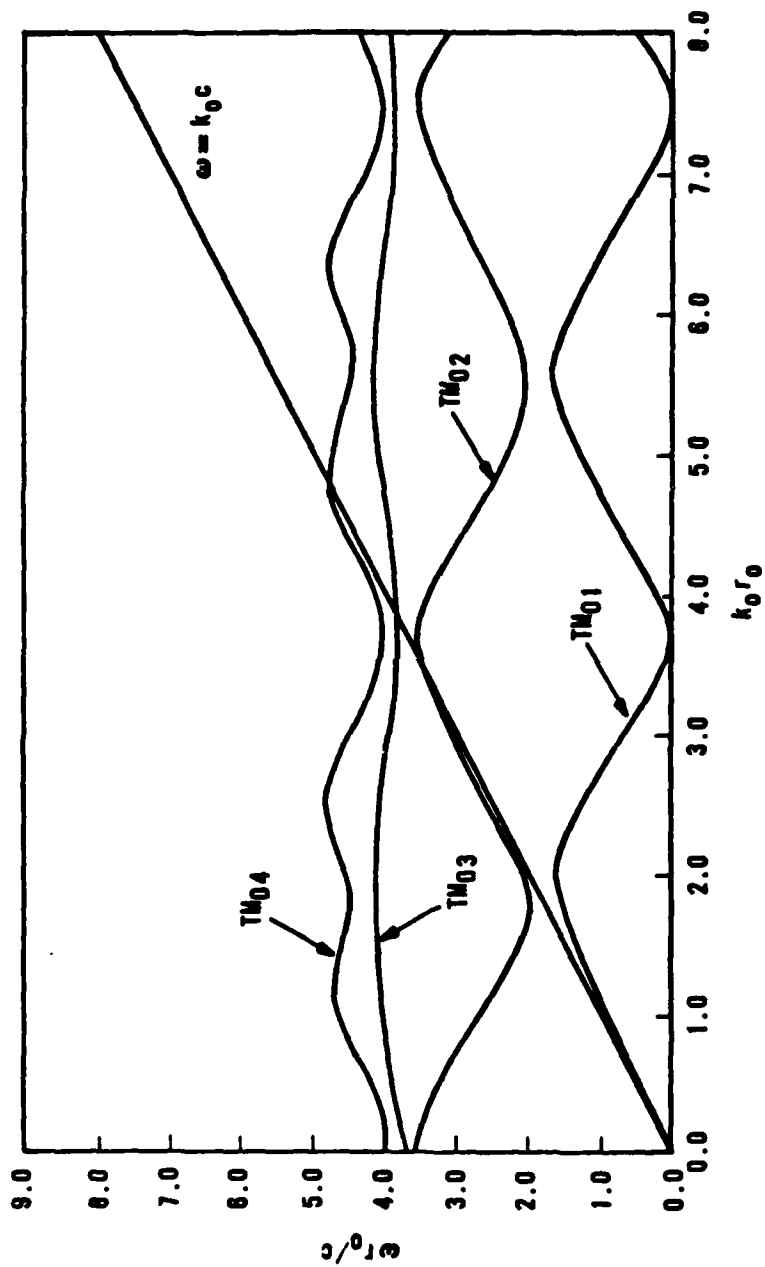


Figure 9. Dispersion diagram for TM_{0n} waves in a coaxial rippled waveguide showing sensitivity to structure period.

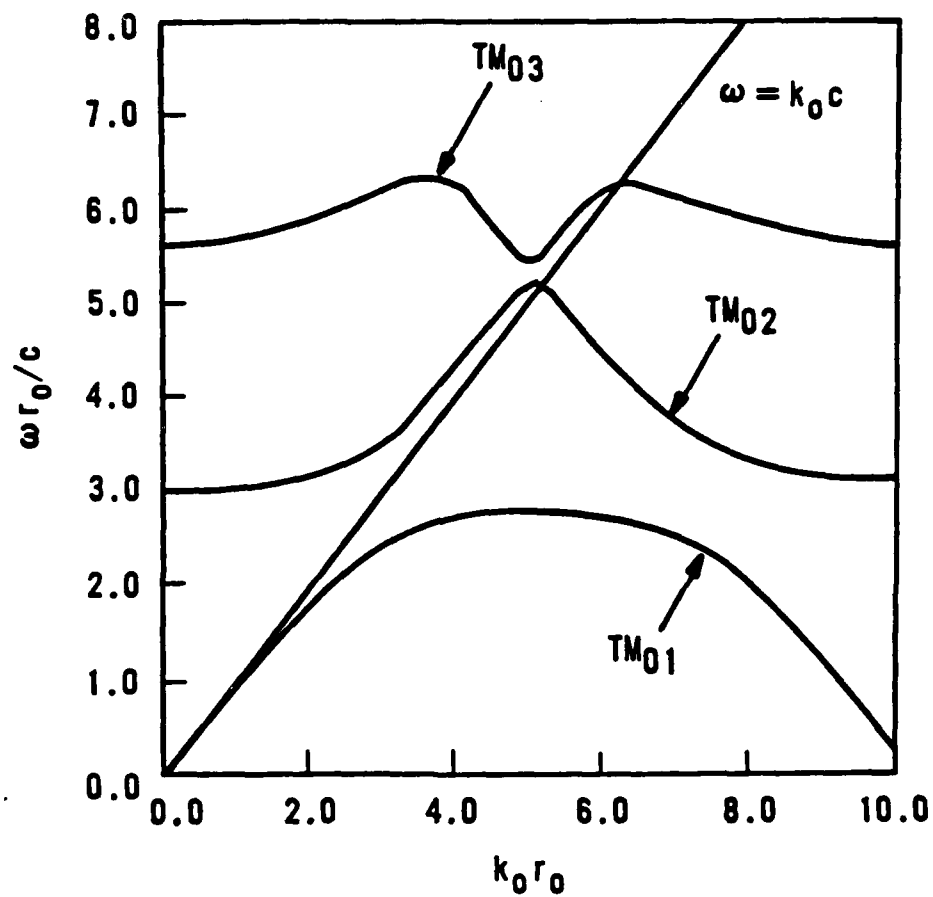


Figure 10. Dispersion diagram for TM_{0n} waves in a coaxial rippled waveguide showing sensitivity to slot depth.

With $n = 0$ and $\epsilon = 0$, the MILO dispersion equations should produce solutions corresponding to an ordinary (smooth) coaxial waveguide containing electrons drifting with velocity v_{z0} . In this case, as pointed out in Sec. 2.2, the dispersion relation is expected to consist of fast electromagnetic modes and two space-charge waves.

Figure 11 represents the solution of Eq. 62 with $n = 0$, $\epsilon = 0.0$, $r_c = 0.3$ cm, $r_a = r_0 = 2.4$ cm, $r_e = 1/4$ cm, $I_e = 1.0$ kA, $\beta_e = 0.5$, and $\gamma_e = 1.155$. Comparison with Fig. 2 clearly shows that the dispersion diagram is exactly as expected. Therefore, the MILO dispersion equations are expected to yield accurate solutions when the periodic anode is included, a case already validated in the absence of space charge.

Figures 12 and 13 show how the smooth coaxial line dispersion diagram is modified by increasing electron current and velocity, respectively. In both cases $I_e = -3.0$ kA. Figure 13 corresponds to $\beta_e = 0.85$ and $\gamma_e = 1.91$. Remaining parameters are the same as above.

Comparing Fig. 12 with Fig. 11 shows that the increased current (plasma frequency) has caused the TM_{01} mode to shift upward in frequency, and resulted in further separation of the space-charge waves. We expect this behavior because, as the electron density increases indefinitely, the space-charge sheath looks more like a conductor to the fields; therefore, for very large density, the electron annulus in effect becomes the outer conductor of a coaxial line. In this case, slow waves do not exist and the fast-wave frequencies readjust to the different outer conductor radius.

Comparing Fig. 13 with Fig. 12 indicates that the space-charge wave phase velocity (v_{sc}) is strongly dependent on electron drift velocity. For highly relativistic electrons, it can be shown that $v_{sc} \approx v_{z0}(1 \pm \omega_p/\omega\gamma_0^{3/2})$, where $\omega_p/\omega\gamma_0^{3/2} \ll 1$ (Ref. 23). Figure 13 is consistent with this relationship.

The preceding results give an indication of what the dispersion diagram will look like for the general MILO problem, space charge drifting in a

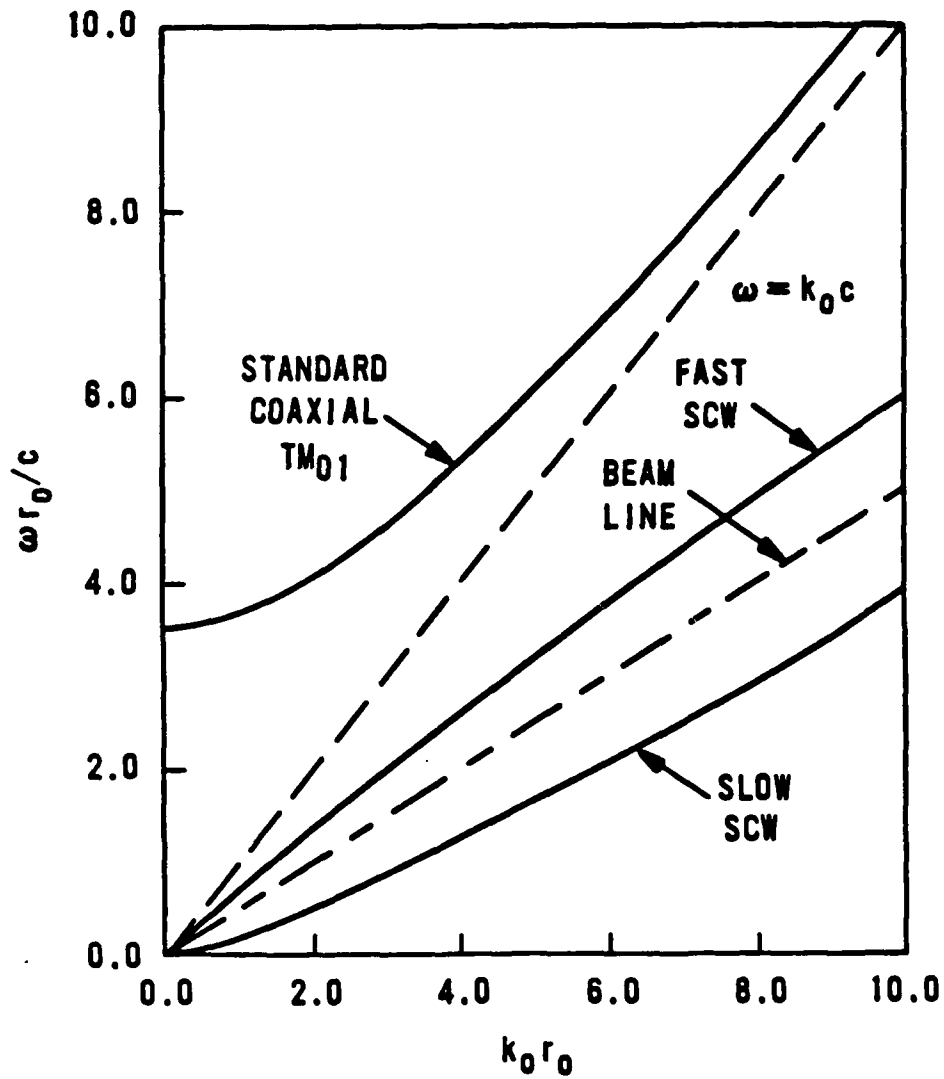


Figure 11. Dispersion diagram for TM_{0n} waves in a smooth, coaxial transmission line containing an annular, monoenergetic electron beam.

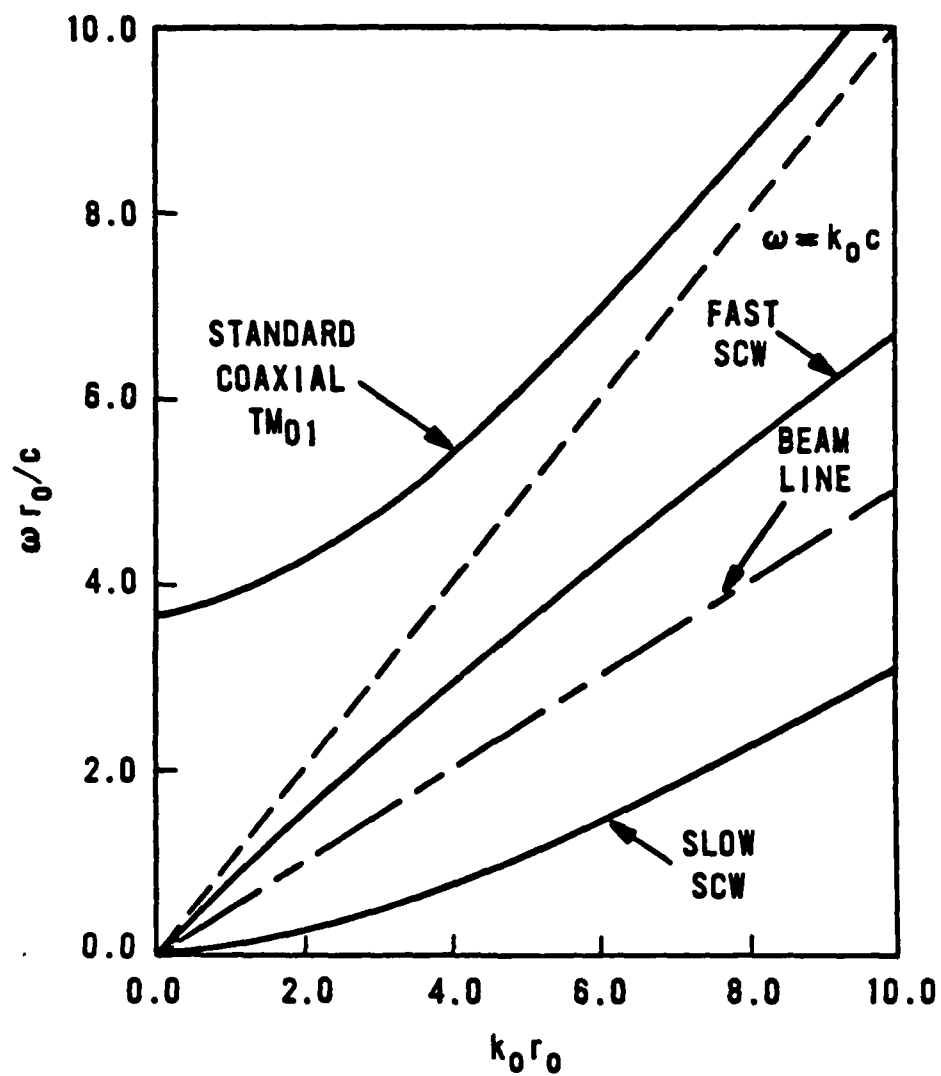


Figure 12. Dispersion diagram for TM_{0n} waves in a smooth, coaxial transmission line containing an annular, monoenergetic electron beam showing sensitivity to beam current.

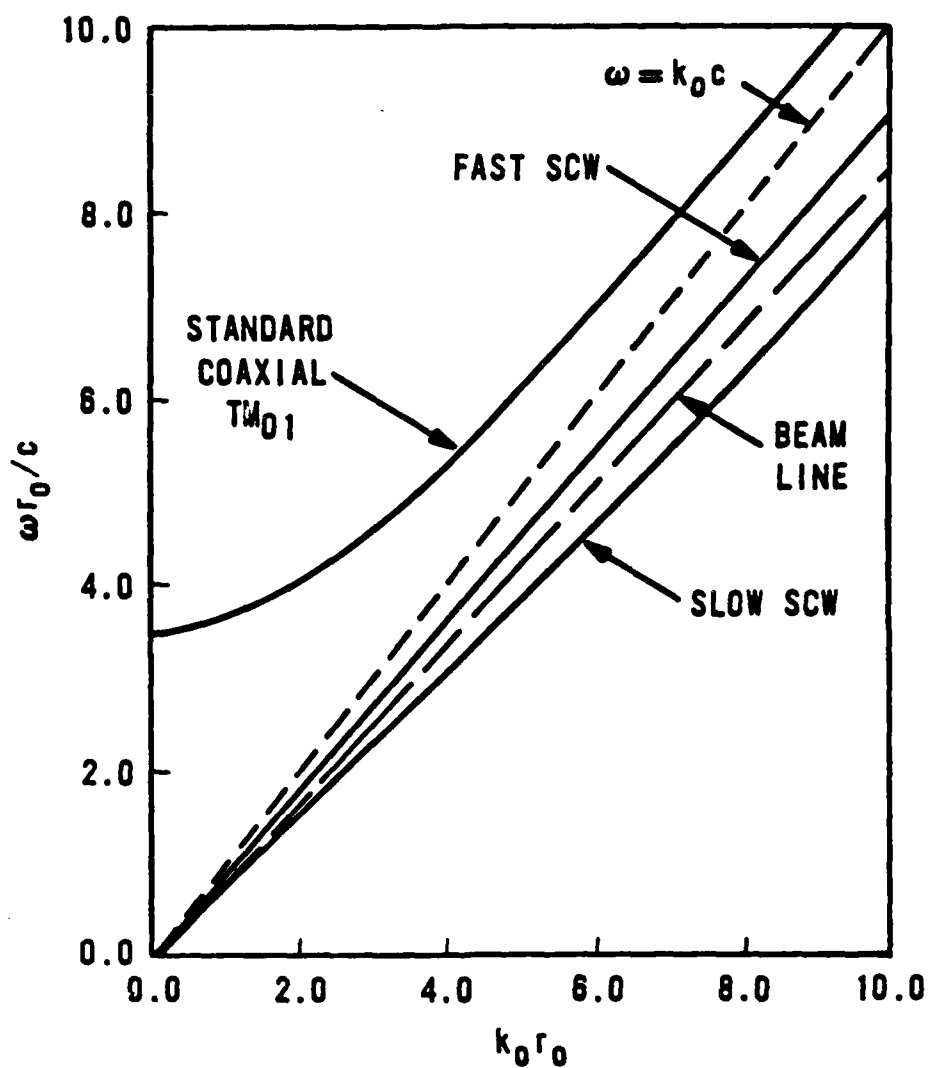


Figure 13. Dispersion diagram for TM_{0n} waves in a smooth, coaxial transmission line containing an annular, monoenergetic electron beam showing sensitivity to beam velocity.

coaxial, periodic transmission line. In this case, the dispersion diagram is expected to resemble a superposition of Figs. 10 and 11; that is, it will consist of fast and slow TM_{0n} modes and space-charge waves. Instability can occur where slow TM_{0n} waves intersect space-charge modes, because at this point they have equal phase velocities. Therefore, in general, the roots of Eq. 62 are composed of real and complex frequencies.

We return to the geometry corresponding to Fig. 10 in which case $r_c = 0.3$ cm, $r_0 = 1.8$ cm, $\epsilon = 0.333$, $d = 1.2$ cm, $z_0 = 1.1$ cm, and $h_0 r_0 = 10.3$. Figure 14 shows how Fig. 10 is modified when an annular electron stream with $r_e = 1.0$ cm, $I_e = -2.0$ kA, $\beta_e = 0.7$, and $\gamma_e = 1.4$ is included. Shown in the figure are the lowest order electromagnetic mode (TM_{01}), beam line and associated space-charge waves, growth rate, and light line. Only the TM_{01} mode is considered because it interacts strongest with the slow space-charge wave. It is clear that the presence of space charge has considerably altered the TM_{01} mode for $k_0 r_0 < 5.5$. The slow space-charge wave merges with the TM_{01} wave to form a single mode in the region $3.0 \leq k_0 r_0 \leq 5.4$. In this region the solution to Eq. 62 has a positive imaginary part indicating instability. The imaginary part of the frequency (growth rate) is also plotted in Fig. 14. Note that there is also a damped solution. As the wave number approaches the boundaries of the unstable region, the growth rate rapidly decreases. The maximum growth rate occurs where the mode group velocity is positive. Therefore, we expect a forward traveling wave that grows in time. From the figure, the oscillation frequency (ν), wave number (k_0), and growth rate (ω_c) of this wave are 6.9 GHz ($1 \text{ GHz} = 1.0 \times 10^9 \text{ s}^{-1}$), 2.5 cm^{-1} , and $4.4 \times 10^9 \text{ s}^{-1}$, respectively. It is clear that the frequency is in the microwave part of the electromagnetic spectrum. The predicted growth rate indicates a rapidly growing instability, the associated wave amplitude increases by a factor of 81.4 ($=e^{4.4}$) every nanosecond ($1 \text{ ns} = 1 \text{ ns} = 1.0 \times 10^{-9} \text{ s}$). The slot-to-slot phase difference in the axial electric field associated with this mode is given by $k_0 z_0 = 2.75$ radians (158 deg), very close to π -mode. The coupling phase velocity is given by $\omega/k_0 = 0.58c$. This phase velocity can be estimated by assuming that the instability occurs near π -mode, in which case the guide wavelength is $2z_0$. Furthermore, the frequency corresponds approximately to a quarter of a free-space wavelength (λ_f) in a slot.

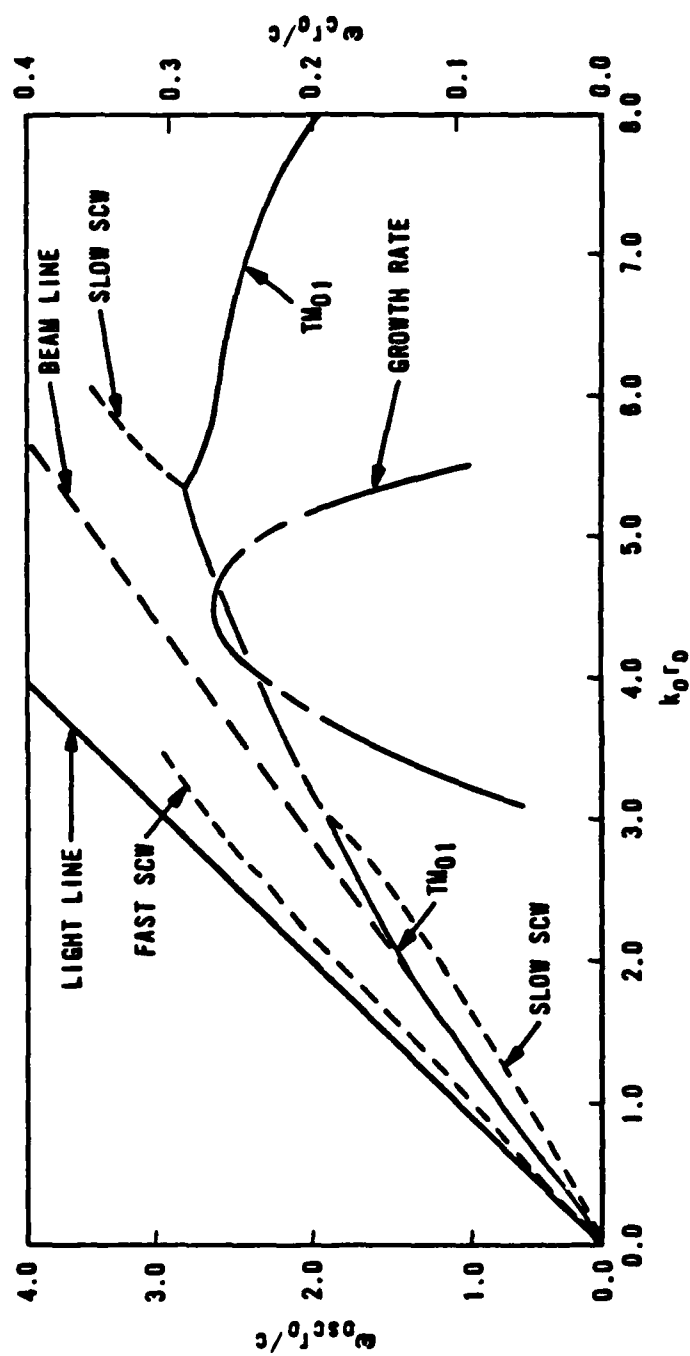


Figure 14. MIO dispersion relation for thin beams.

Thus, in π -mode we expect $k_0 = 2\pi/2z_0 = 2.8 \text{ cm}^{-1}$, $\lambda_f = 4d = 4.8 \text{ cm}$, $v = c/\lambda_f = 6.2 \text{ GHz}$, and $\omega/k_0 = 0.47c$. The estimated coupling velocity is 19 percent smaller than the exact value, but provides a good indication of the dominant TM wave-phase velocity and the electron velocity needed for coupling. The accuracy of the preceding approximation improves with increasing slot depth.

Not shown in Fig. 14 is the point where the slow space-charge wave intersects higher order electromagnetic modes (see Fig. 10). Although instability occurs at these frequencies, corresponding growth rates are at least an order of magnitude lower than the dominant mode; hence, these modes are only weakly present in the MIO.

The instability growth rate is very sensitive to the position of the space-charge sheath with respect to the anode slots. For example, we decreased the maximum growth rate in Fig. 14 by a factor of 2.4, to $1.8 \times 10^9 \text{ s}^{-1}$, by decreasing the electron radius to $r_e = 0.65 \text{ cm}$. This behavior is expected because the axial electric field associated with the TM_{01} mode is largest at the anode slot entrance; therefore, this is the point where an electron interacts strongest with the field.

The discussion of Fig. 14 ignored the fast space-charge wave. This wave is in general stable, because waves traveling faster than the electron flow cannot take energy from it.

According to the above discussion on space-charge waves, we should be able to modify the general MIO dispersion diagram (Fig. 14) by changing electron velocity. Figure 15 confirms this hypothesis, and represents the solution of Eq. 62 with $r_c = 0.3 \text{ cm}$, $r_o = 1.8 \text{ cm}$, $\epsilon = 0.333$, $d = 1.2 \text{ cm}$, $z_0 = 1.1 \text{ cm}$, $h_0 r_0 = 10.3$, $r_e = 1.0 \text{ cm}$, $I_e = -2.0 \text{ kA}$, $\beta_e = 0.85$, and $\gamma_e = 1.9$. Note that the peak growth rate has decreased by 13 percent from the previous example. This is to be expected for monoenergetic space-charge flows because it is difficult to accelerate (decelerate) relativistic electrons in the direction of (opposite to) their velocity. Since the TM wave energy is supplied by

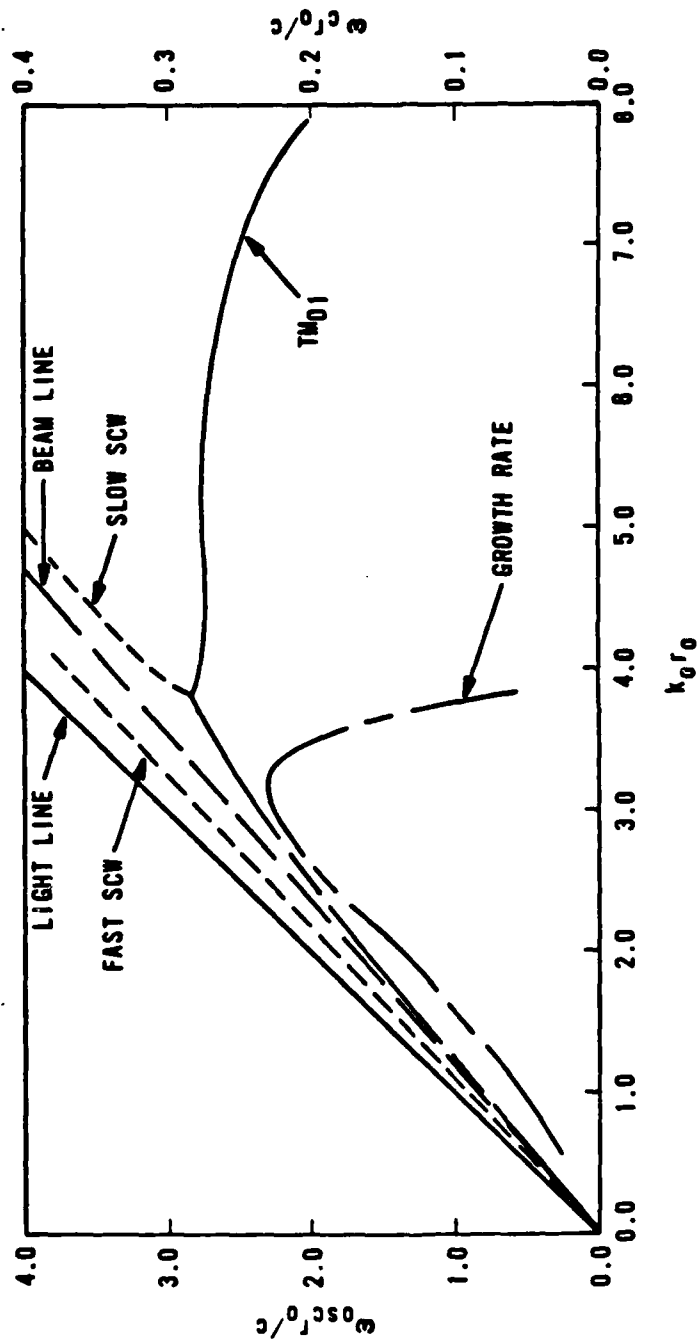


Figure 15. MIO dispersion relation for thin beams showing sensitivity to beam velocity.

electron energy loss via the decelerating axial electric field, we expect the instability growth rate to decrease with increasing particle velocity.

4.2 COMPARISON WITH NUMERICAL SIMULATION I

Results obtained with the analytic dispersion relation provide a picture of MILO physics. To determine whether or not this is an accurate picture, comparisons are made with numerical simulation. The code ISIS (Refs. 23, 24) was used for this purpose.

ISIS is a 2-D, fully electromagnetic, particle-in-cell (PIC) code frequently used for simulating problems involving the interaction of charged particles with electromagnetic fields. We use ISIS to simulate the MILO.

Figure 16 is a schematic of the simulation geometry showing cathode, anode, and corresponding periodic structure. In this case, it is easier to model the periodic anode with a square wave function. The specific geometrical parameters are $r_c = 1.0$ cm, A-K gap = 1.0 cm, d (slot depth) = 0.75 cm, and $z_0 = 1.4$ cm. Experience shows that ten slots are more than adequate for comparisons with analytic theory. We assume that the analytic theory can be applied with reasonable accuracy to finite length slow-wave structures when the structure length is much longer than its period.

To predict the outcome of the simulation, solve Eq. 62 to obtain the dispersion diagram corresponding to an electron stream drifting in a MILO whose geometry corresponds approximately to Fig. 16. The space-charge parameters are $I_e = -7.8$ kA, $r_e = 1.5$ cm, $\beta_e = 0.89$, and $\gamma_e = 2.20$. The square-wave anode is modeled with Eq. A-2 in Appendix A. Figures 17 and 18 represent dispersion diagrams corresponding to the structure in Fig. 16. Figure 17 is the cold dispersion relation; that is, space charge is not included. Figure 18 includes the aforementioned electron stream. The effect of square wave slots (compared with sinusoidal) is to flatten the TM_{01} mode. The average depth of a sinusoid is less than that of a square wave. Hence, the latter corresponds to lower frequency.

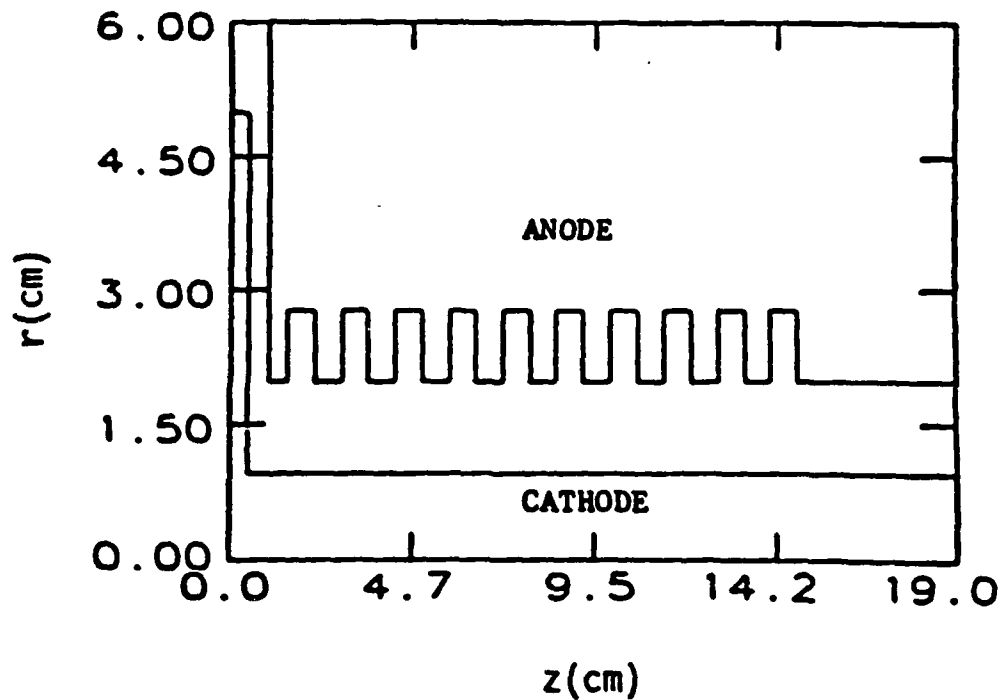


Figure 16. Schematic of geometry used in ISIS MILO simulation.

In Fig. 18, curves labeled A and C are the first two modes shown in Fig. 17. The curve labeled B is the lowest order space-charge wave. Not shown is the corresponding fast wave. Curve D represents the growth rate of the instability that results from the interaction of the TM_{01} mode (A) with the slow space-charge wave (B). The most unstable mode has a positive group velocity (forward wave) and occurs at a frequency $\nu = 6.2$ GHz with a growth rate of $\omega_c = 3.0 \times 10 \text{ s}^{-1}$. The associated wave number is $k_0 = 1.625$ and corresponds approximately to a $2\pi/3$ -mode. Thus, the ISIS simulation is expected to show a very rapidly growing forward-wave instability at a frequency of 6.2 GHz.

In ISIS, the electron flow is generated by space-charge-limited emission from the cathode. Electron emission is initiated by launching a zero frequency TEM wave at the left-hand boundary (Fig. 16). Electrons are

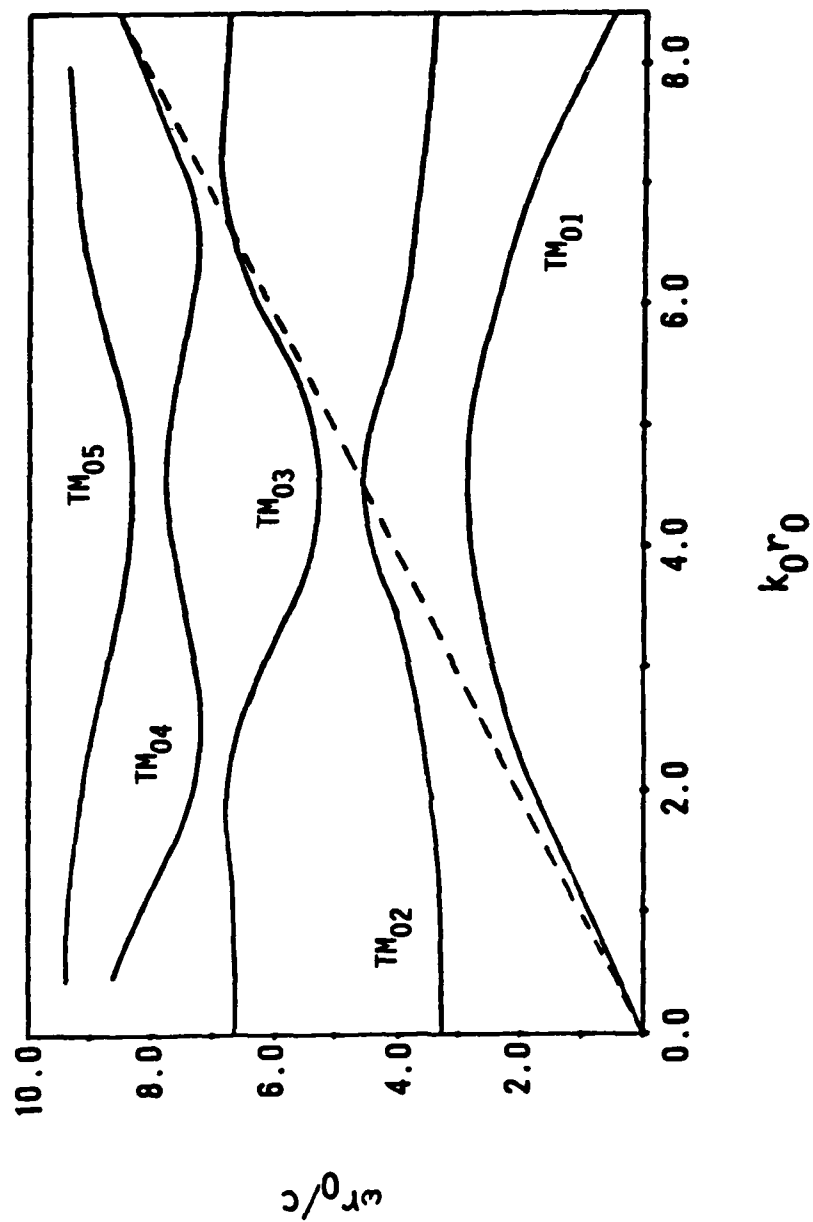


Figure 17. Dispersion relation for TM_{0n} waves in ISIS simulation geometry.

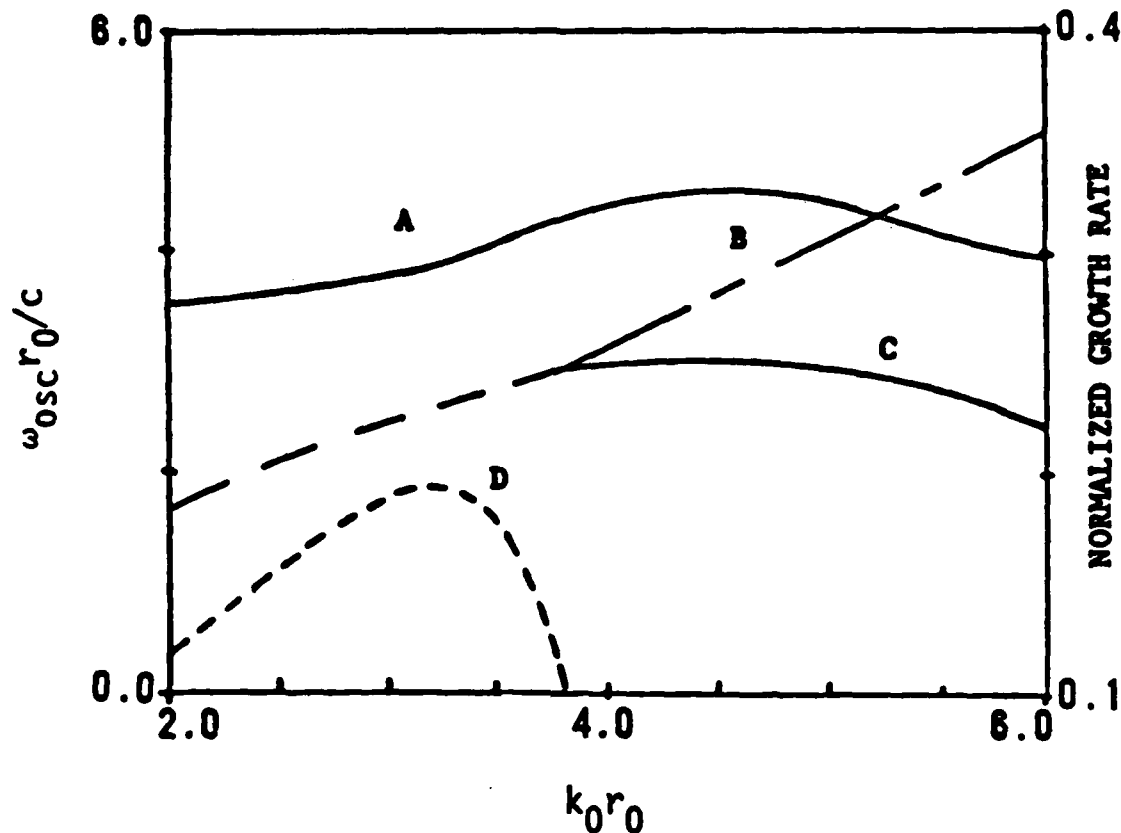


Figure 18. Dispersion relation for TM_{0n} waves in ISIS simulation geometry including space-charge effects.

emitted when the cathode electric field amplitude reaches a specified threshold value.

Figure 19 is an ISIS particle plot 2.2 ns of physics time into a MILO simulation. The left-hand boundary is designed to control source impedance. At the structure midpoint, the electron current and maximum velocity are $|I_e| = 7.9$ kA and $\beta_e = 0.89$, respectively. These agree well with values used in the analytic theory. Note that the space charge flow is neither monoenergetic nor annular; ramifications of this are discussed below.

Inspection of Fig. 19 shows that the MILO electron flow has been modulated by the growing axial electric field. Bunches of charge have formed with an

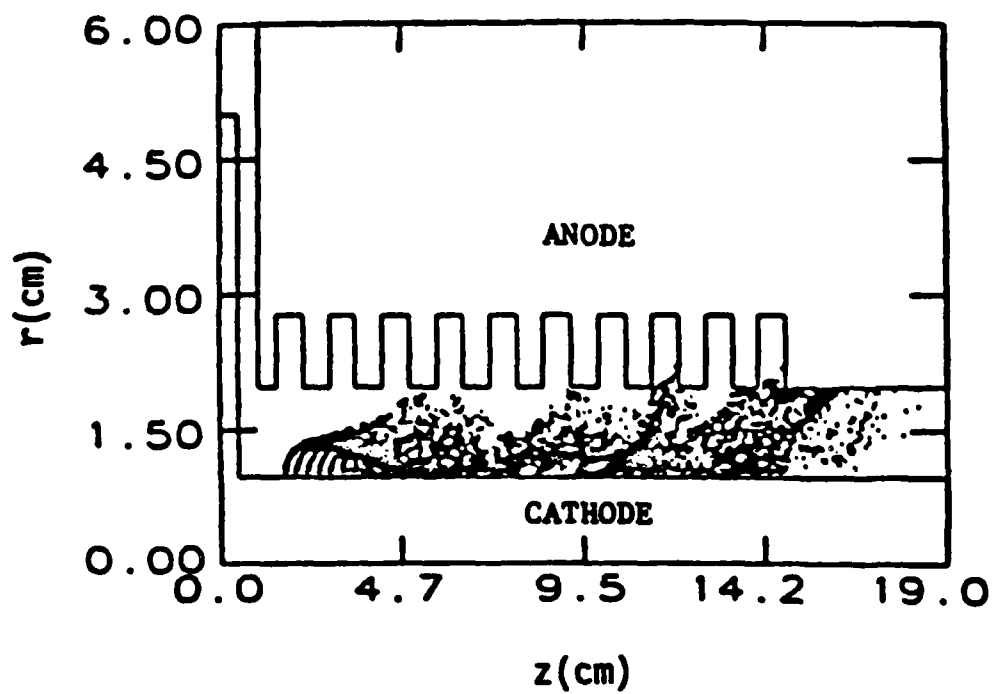


Figure 19. ISIS MILO simulation: particle plot.

approximate separation of $3z_0$. Assuming that this distance also represents the axial electric field (E_z) wavelength, we estimate the mode to be $2\pi/3$, in good agreement with the analytical estimate.

The axial variation (z dependence) of E_z is shown in Fig. 20, which is a plot of E_z versus z at a radial position corresponding to the slot entrances at time $t = 2.2$ ns. Slot numbers are indicated on the plot. The field amplitude is increasing with axial distance (z) from the left-hand boundary, characteristic of a forward-wave instability. In slots 1-4, the field changes sign at the slot midpoint. The total field in these four slots is dominated by the zero frequency mode associated with two-conductor systems (discussed above). In slots 5-10, the oscillatory TM_{01} axial electric field dominates. Since Fig. 20 is for a fixed time, the exact slot-to-slot phase difference is not obvious. Nevertheless, the oscillation is clearly in the vicinity of π -mode.

To obtain the instability oscillation frequency, monitor E_z as a function of time. Figure 21a is a time history of E_z at the midpoint of the entrance to slot six. The vertical axis is normalized to 511 kV/cm. In agreement with theory, the instability grows rapidly, saturating in a little more than 2.0 ns. Saturation is a nonlinear phenomenon that is not modeled in the analytic theory. The nonlinear state occurred too early in the simulation to enable a reasonable estimate of the growth rate.

Figure 21b represents the frequency spectrum associated with Fig. 21a. The dominant frequency is 6.6 GHz, in good agreement with theory. In addition, higher order modes are either very weak or nonexistent, indicating small associated growth rates.

Despite the crude space-charge model used in the analytic theory, reasonable agreement was obtained with the more realistic simulation results. Oscillation frequency and mode are characteristics of geometry and are not very sensitive to the electron equilibrium. Thus, the analytic theory is expected to produce good estimates of these parameters regardless of the space-charge equilibrium employed. This is not true for predictions of the growth rate. Analytic theory showed that the growth rate decreased with increasing electron

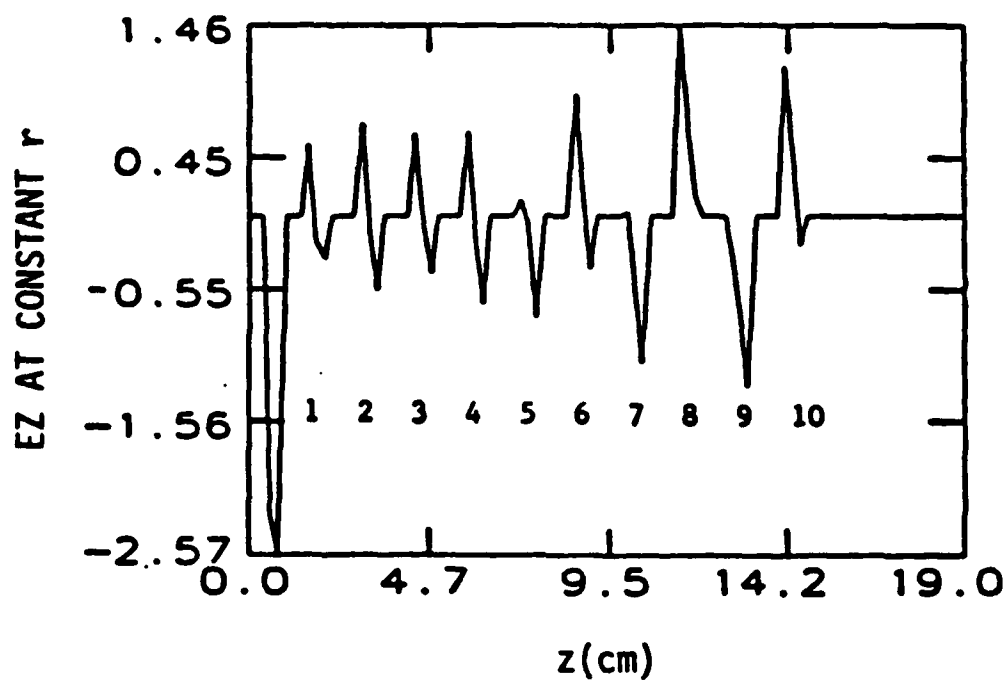
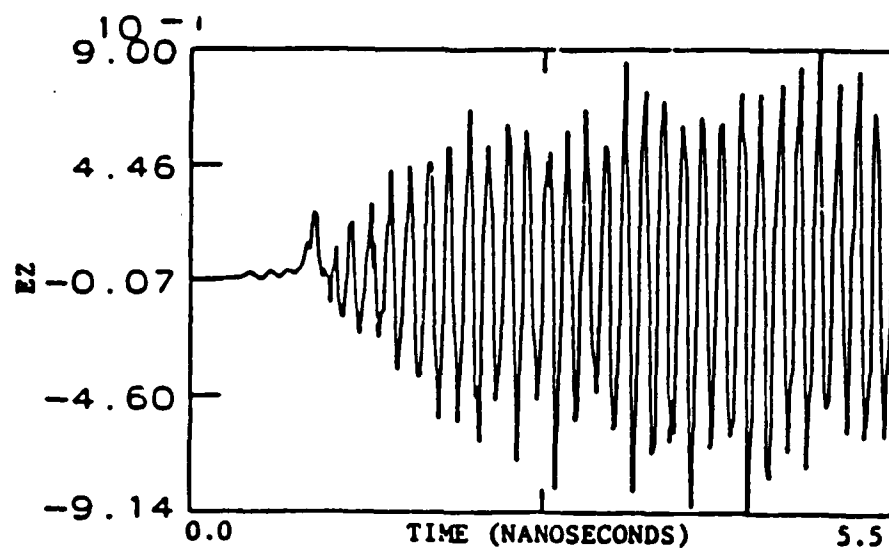
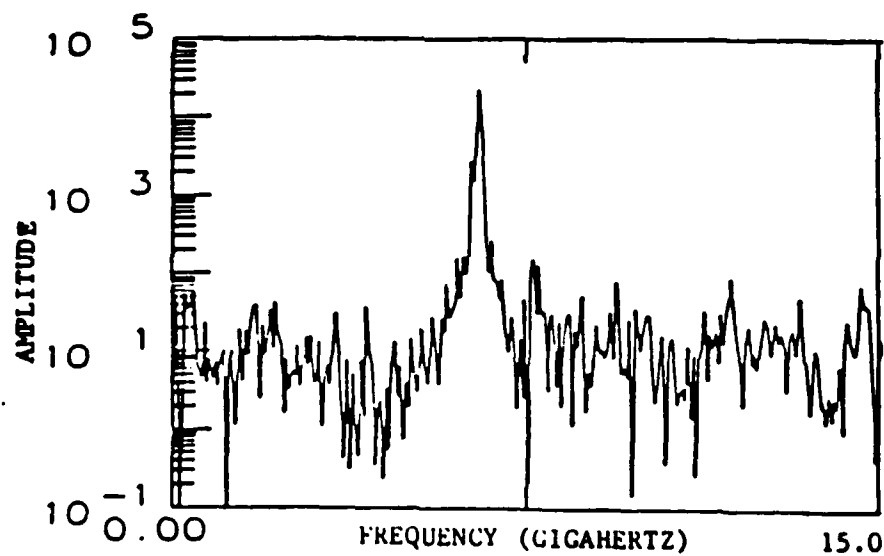


Figure 20. ISIS MILO simulation: axial field amplitude versus Z .



(a) Axial Field at Slot 6.



(b) Spectrum.

Figure 21. ISIS MILO simulation: time history and Fourier transform of the axial electric field.

velocity. Although this result is consistent with the physics of monoenergetic electron flow, it does not agree with what is observed in simulations of magnetically insulated flow in periodic structures. Numerous ISIS simulations of the MILO indicate that the instability growth rate is relatively insensitive to transmission line voltage when the latter is above a critical value. This result is consistent with the physics of magnetic insulation (Sec. 2.1). Recall that in insulated flow, the electron velocity varies from 0 to some maximum (v_e). If v_e is greater than the structure coupling velocity, a resonant layer of electrons will always be present, and oscillations will occur at any voltage. This is exactly the behavior observed in simulations. Thus, the analytic theory cannot accurately predict growth rate and related dependencies unless a model of magnetically insulated electron flow is incorporated, a task which is accomplished in the following section.

Another reason for changing the analytic physics model is to obtain a dispersion equation with wider applicability and which is more efficiently solved on a computer. The algorithm employed to solve Eq. 62 required evaluating numerous Bessel functions, some having complex arguments, to obtain the matrix elements. The matrix elements become very large ($> 10^6$) for geometries with significant radial extent (largest radius > 4.0 cm). Consequently, the value of the associated matrix determinant is beyond what can be handled by the root solver, CROOT.

In the following section, a MILO dispersion equation is derived that includes the physics of magnetically insulated space-charge flow, and can be numerically solved for geometries with reasonably large radial extent.

5.0 MILO DISPERSION RELATION FOR RELATIVISTIC BRILLOUIN FLOW

In this section, the MILO dispersion relation is rederived using a kinetic theory approach. The result corresponds better to reality because most of the assumptions used in Section 3 have been eliminated. The electron equilibrium is modeled with a distribution function that corresponds to relativistic Brillouin flow (RBF), discussed in Section 2.1. The formalism used here is easily extended to include nonlaminar electron equilibria. However, in the latter case not much analytic work can be done because the resulting orbit integral (defined below) is too complicated. Therefore, we restrict the forthcoming analysis to RBF.

Using a perturbation of the form given by Eq. 30, an expression for the perturbed distribution function, which determines the source functions for Maxwell's equations, is derived from the relativistic Vlasov equation. An expression for the perturbed current density is derived and substituted into the linearized Maxwell's equations to obtain the perturbed fields. Application of appropriate electric field boundary conditions leads to a dispersion relation.

Before proceeding with the derivation, we review a few results from the kinetic theory of plasmas (Ref. 25). Let $f(\vec{x}, \vec{p}, t)$ represent the distribution of electrons in phase space where \vec{x} , \vec{p} , and t denote position, momentum, and time, respectively. In the absence of collisions, f is conserved; therefore, its total derivative (df/dt) is equal to zero. Because the particle position in phase space may change with time, the total time derivative operator must be given by

$$\frac{d}{dt} = \frac{\partial}{\partial t} + \frac{d\vec{x}}{dt} \cdot \nabla_{\vec{x}} + \frac{d\vec{p}}{dt} \cdot \nabla_{\vec{p}} \quad (63)$$

where $\nabla_{\vec{x}}$ and $\nabla_{\vec{p}}$ represent the gradient operation with respect to \vec{x} and \vec{p} , respectively. Thus, for collisionless electrons in an electromagnetic field, conservation of $f(\vec{x}, \vec{p}, t)$ implies

$$\left[\frac{\partial}{\partial t} + \vec{v} \cdot \nabla_{\vec{x}} - e \left(\vec{E} + \frac{\vec{v}}{c} \times \vec{B} \right) \cdot \nabla_{\vec{p}} \right] f(\vec{x}, \vec{p}, t) = 0 \quad (64)$$

where \vec{v} has been used for $d\vec{x}/dt$ and $d\vec{p}/dt = -e \left(\vec{E} + \frac{\vec{v}}{c} \times \vec{B} \right)$.

With $\vec{v} = c\vec{p}/(m^2 c^2 + p^2)^{1/2}$, Eq. 64 is the relativistically correct Vlasov equation; its solution describes the evolution of the electron distribution in phase space. Corresponding number and current densities are given by

$$n(\vec{x}, t) = \int d\vec{p} f(\vec{x}, \vec{p}, t) \quad (65)$$

$$\vec{J}(\vec{x}, t) = -e \int d\vec{p} \vec{v} f(\vec{x}, \vec{p}, t) \quad (66)$$

where the integral is over all of momentum space and $d\vec{p}$ represents an infinitesimal volume element in this space.

Any function f depending only on constants of the motion is a solution of Eq. 64. This fact is used in Appendix B to obtain a distribution function for RBF.

Let f_1 represent a perturbation of the distribution function about its equilibrium f_0 such that $f = f_0 + f_1$ ($|f_1/f_0| \ll 1$). Similarly, we write the total electric and magnetic fields as $\vec{E} = \vec{E}_0 + \vec{E}_1$ and $\vec{B} = \vec{B}_0 + \vec{B}_1$, respectively. Substituting these expansions into Eq. 64 and performing some algebra yields to first order in the perturbed quantities

$$\begin{aligned} & \left[\frac{\partial}{\partial t} + \vec{v} \cdot \nabla_{\vec{x}} - e \left(\vec{E}_0 + \frac{\vec{v}}{c} \times \vec{B}_0 \right) \cdot \nabla_{\vec{p}} \right] f_1(\vec{x}, \vec{p}, t) \\ & = e \left(\vec{E}_1 + \frac{\vec{v}}{c} \times \vec{B}_1 \right) \cdot \nabla_{\vec{p}} f_0(\vec{x}, \vec{p}, t) \end{aligned} \quad (67)$$

The parameters \vec{x} , \vec{v} , and \vec{p} were not expanded because in Eqs. 64 and 67 they represent coordinates.

We now obtain an expression for $f_1(\vec{x}, \vec{p}, t)$ by integrating Eq. 67 over unperturbed (equilibrium) particle orbits. Let $\vec{x}(t')$, $\vec{v}(t')$, and $\vec{p}(t')$

represent the time-dependent electron position, velocity, and momentum, respectively, such that at time $t' = t$, $\vec{X}(t) = \vec{x}$, $\vec{V}(t) = \vec{v}$, and $\vec{P}(t) = \vec{p}$. That is, at $t' = t$ the particle reaches a point in phase space having coordinates \vec{x} , \vec{p} , and t . Evaluated along the unperturbed orbit, the left-hand side of Eq. 67 is the total time derivative of f_1 (df_1/dt). Thus, Eq. 67 can be written as

$$\begin{aligned} \frac{d}{dt} f_1(\vec{x}', \vec{p}', t') = e \left[\vec{E}_1(\vec{x}', t') \right. \\ \left. + \frac{\vec{v}'}{c} \times \vec{B}_1(\vec{x}', t') \right] \cdot \nabla_{\vec{p}'} f_0(\vec{x}', \vec{p}', t') \end{aligned} \quad (68)$$

where $\vec{x}' = \vec{X}(t')$, $\vec{v}' = \vec{V}(t')$, and $\vec{p}' = \vec{P}(t')$. Multiplying Eq. 68 by dt' and integrating from $-\infty$ to t yields

$$\begin{aligned} f_1(\vec{x}, \vec{p}, t) = e \int_{-\infty}^t dt' \left(E_1[X(t'), t'] \right. \\ \left. + \frac{1}{c} \vec{V}(t') \times \vec{B}_1[\vec{X}(t'), t'] \right) \cdot \nabla_{\vec{p}'} f_0[\vec{X}(t'), \vec{P}(t'), t'] \end{aligned} \quad (69)$$

To obtain the previous expression, the perturbation was assumed to be non-existent at $t = -\infty$; therefore, $f_1(\vec{x}, \vec{p}, t' = -\infty) = 0$. The integral in Eq. 69 is sometimes referred to as the orbit integral.

Using the aforementioned linear expansion for f in Eqs. 65 and 66, one can derive expressions for the perturbed electron and current densities in terms of f_1 . To first order we have

$$n_1(\vec{x}, t) = \int d\vec{p} f_1(\vec{x}, \vec{p}, t) \quad (70)$$

and

$$\vec{J}_1(\vec{x}, t) = -e \int d\vec{p} \vec{v} f_1(\vec{x}, \vec{p}, t) \quad (71)$$

for the perturbed number and current densities, respectively.

The integral in Eq. 69 cannot be evaluated without expressions for f_0 , \vec{E}_1 , and \vec{B}_1 . Although knowledge of f_0 is assumed, the perturbed fields cannot be determined without first knowing f_1 because the latter is used to obtain the perturbed sources. Therefore, Eqs. 69-71 must be solved self-consistently with Maxwell's equations.

In most cases, self-consistent analytic expressions for f_1 , n_1 , \vec{J}_1 , \vec{E}_1 and \vec{B}_1 cannot be obtained because the orbit integral cannot be evaluated. However, in the case of RBF, analytic solutions are possible, and are used to derive a more physically accurate dispersion relation (than in Sec. 3) for the MILO.

The relevant geometry is shown in Fig. 6, and the same assumptions (as in Section 3) are made regarding length and azimuthal symmetry. The electron flow is magnetically insulated and confined to the region $r_c \leq r \leq r_e$. An external guiding field is not needed because the flow is self-insulated. We assume the electron equilibrium corresponds to RBF; therefore, all electrons move in laminar orbits with the same constant Hamiltonian (H) and canonical momentum (P_z). A distribution function corresponding to this equilibrium is given by

$$f_0 = n(r) \delta(H - mc^2 + P_z) \delta(p_r) \delta(p_\theta) \quad (72)$$

where p_i represents the i th component of momentum, $H = c(p_z^2 + m^2c^2)^{1/2} - e\phi(r)$, $P_z = p_z - eA_z(r)/c$, $n(r) = A^2(mc^3/4\pi e^2)(r_c/r)^A/r^2$, A is the constant defined by Eq. 21, and $\phi(r)$ and $A_z(r)$ represent the equilibrium electric and magnetic potentials, respectively. All equilibrium quantities are defined in Section 2.1. The development of Eq. 72 with constant of the motion $n(r)$ is in Appendix B.

Similar to Section 3, we expand all field and charge quantities about the above equilibrium and look for TM_{0m} modes. Corresponding vacuum equations are obtained by setting the charge plasma frequency equal to zero. From Section 3, the linearized Maxwell equations in the space-charge region are given by

$$\frac{\partial E_{r1}}{\partial z} - \frac{\partial E_{z1}}{\partial r} = -\frac{1}{c} \frac{\partial B_{\theta 1}}{\partial t} \quad (73)$$

$$-\frac{\partial B_{\theta 1}}{\partial z} = \frac{1}{c} \frac{\partial E_{r1}}{\partial t} \quad (74)$$

and

$$\frac{1}{r} \frac{\partial}{\partial r} r B_{\theta 1} = \frac{4\pi}{c} J_{z1} + \frac{1}{c} \frac{\partial E_{z1}}{\partial t} \quad (75)$$

In Eq. 75, J_{z1} , is given by the z component of Eq. 71.

Now assume a perturbation of the form given by Eq. 30, and use Eqs. 69-72 to obtain an expression for the spatial harmonics of J_{z1} . Once J_{z1} is known, all perturbed field components can be determined.

Equation 69 can be simplified by noting that f_0 depends only on r and p_z ; therefore,

$$\nabla_{\vec{p}} \cdot f_0[\vec{X}(t^-), \vec{p}(t^-), t^-] = \hat{k} \frac{df_0}{dp_z} \bigg|_{\vec{X}'=\vec{X}(t^-)} \quad (76)$$

where in this case $\vec{p}(t^-)$ represents ordinary momentum and is not to be confused with canonical momentum. By assumption $\vec{B}_1 = B_{\theta 1} \hat{\theta}$, and because the electron orbits are laminar, $\vec{V}(t^-) = V_z(t^-) \hat{k}$. Thus, the magnetic force term in Eq. 69 has no z component, so its dot product with $\nabla_{\vec{p}} \cdot f_0$ is identically zero. Using Eq. 76, Eq. 69 reduces to

$$f_1(\vec{X}, \vec{p}, t) = e \int_{-\infty}^t dt^- E_{z1}[\vec{X}(t^-), t^-] \frac{\partial f_0}{\partial p_z} \bigg|_{p_z' = p_z(t^-)} \quad (77)$$

Because the orbits are laminar, the electron radial position r is a constant of the motion. In addition, p_z' is a constant of the motion because the system is in equilibrium. Therefore, $\partial f_0 / \partial p_z'$ can be taken outside of the integral in Eq. 77. The perturbed distribution function can now be written as

$$f_1(\vec{x}, \vec{p}, t) = e \frac{\partial f_0}{\partial p_z} \int_{-\infty}^t dt' E_{z1}[\vec{x}(t'), t'] \quad (78)$$

Substituting an expression in the form of Eq. 30 for E_{z1} into Eq. 78 yields

$$f_1(\vec{x}, \vec{p}, t) = e \frac{\partial f_0}{\partial p_z} \sum_{n=-\infty}^{\infty} \int_{-\infty}^t dt' E_{zn}[r(t')] \exp\{i[k_n Z(t') - \omega t']\} \quad (79)$$

In Eq. 79, $Z(t')$ represents the electron trajectory and is determined by solving

$$\frac{d}{dt'} Z(t') = V_z[r(t'), t'] \quad (80)$$

where $V_z[r(t'), t'] = E_{r0}[r(t'), t'] / B_{\theta 0}[r(t'), t']$ is the radially dependent electron drift velocity given in Section 2.1. Because V_z is constant along any particle orbit, Eq. 80 is readily integrated to give

$$Z(t') = z + V_z(t' - t) \quad (81)$$

for the trajectory. To obtain Eq. 81, the condition $Z(t'=t) = z$ was used.

Substituting Eq. 81 into the right-hand side of Eq. 79 yields

$$f_1(\vec{x}, \vec{p}, t) = e \frac{\partial f_0}{\partial p_z} \sum_{n=-\infty}^{\infty} E_{zn} \exp[i(k_n z - \omega t)] \int_{-\infty}^t dt' \exp[-i\Omega_n(t' - t)] \quad (82)$$

where $\Omega_n = \omega - V_z k_n$ is the velocity shifted frequency. Note that E_{zn} has been taken out of the integral in Eq. 82 because, depending only on r , it is a constant of the motion.

Let $I_n(t)$ represent the integral in Eq. 82. Making the transformation $\tau = t' - t$ gives

$$I_n(t) = \int_{-\infty}^0 d\tau e^{-i\Omega_n \tau} \quad (83)$$

The integral is well behaved if ω has a positive complex component. This is the condition for instability and is satisfied in general when space charge is present. In this case, the integral is zero at $\tau = -\infty$. Thus,

$$I_n(t) = - \frac{1}{i\Omega_n(t)} \quad (84)$$

where $\Omega_n(t) = \omega - v_z k_n$. We have redefined Ω_n to reflect the fact that, because the electron velocity is evaluated at $t' = t$, it must now be interpreted as a coordinate in phase space. Substituting Eq. 84 into Eq. 82 yields

$$f_1(\vec{x}, \vec{p}, t) = ie \frac{\partial f_0}{\partial p_z} \sum_{n=-\infty}^{\infty} \frac{E_{zn}}{\Omega_n} \exp[i(k_n z - \omega t)] \quad (85)$$

Using Eqs. 71, 72 and 85, we can derive an expression for the perturbed current density. Substituting Eq. 85 for f_1 into the z component of Eq. 71 yields

$$J_{z1}(r, t) = -ie^2 \sum_{n=-\infty}^{\infty} E_{zn} I_n^*(f_0) \exp[i(k_n z - \omega t)] \quad (86)$$

where

$$I_n^*(f_0) = \int_{-\infty}^{\infty} \int_{-\infty}^{\infty} \int_{-\infty}^{\infty} dp_z dp_\theta dp_r \frac{v_z}{(\omega - v_z k_n)} \frac{\partial f_0}{\partial p_z} \quad (87)$$

In Eq. 87, Ω_n has been written explicitly to show its dependence on v_z . Integrating Eq. 87 using Eq. 72 for f_0 is quite tedious; details are in Appendix C. Substituting the result into Eq. 86 yields

$$J_{z1}(r, t) = iA^2 \frac{m^3 c^6}{\pi} \left(\frac{r_c}{r} \right) A \frac{g(r)}{r^2} \times \sum_{n=-\infty}^{\infty} \frac{\omega E_{zn} \exp[i(k_n z - \omega t)]}{[(\omega/c - k_n)m^2 c^4 + (\omega/c + k_n)g^2(r)]^2} \quad (88)$$

where $g(r) = e\phi(r) + mc^2 - eA_z(r)$. Equation 88 can be simplified considerably using expressions corresponding to RBF in Section 2.1. Note that for $\rho = \ln[(r/r_c)^A]$, $[\cosh(\rho) - \sinh(\rho)] = (r_c/r)^A = g(r)/mc^2$. The denominator in the summation of Eq. 88 can be rewritten as

$$m^4 c^8 \left\{ \frac{\omega}{c} \left[1 + \frac{g^2(r)}{m^2 c^4} \right] - k_n \left[1 - \frac{g^2(r)}{m^2 c^4} \right] \right\}^2 \quad (89)$$

Substituting the above hyperbolic expression for $g(r)$ into Eq. 89 and performing some algebra yields

$$4m^4 c^8 [\cosh(\rho) - \sinh(\rho)]^2 \left[\frac{\omega}{c} \cosh(\rho) - k_n \sinh(\rho) \right]^2 \quad (90)$$

Rewriting Eq. 88 with r -dependent functions replaced by their hyperbolic counterparts and multiplying numerator and denominator by $1/\cosh(\rho)$, after some cancellation gives

$$J_{z1}(r,t) = i \frac{A^2}{4\pi} \frac{1}{r^2 \cosh^2(\rho)} \sum_{n=-\infty}^{\infty} \frac{\omega E_{zn} \exp[i(k_n z - \omega t)]}{\left[\frac{\omega}{c} - k_n \tanh(\rho) \right]^2} \quad (91)$$

Using definitions of ω_p , γ_0 and v_{z0} given in Section 2.1, Eq. 91 simplifies to

$$J_{z1}(r,t) = \frac{i}{4\pi} \frac{\omega_p^2}{\gamma_0^3} \sum_{n=-\infty}^{\infty} \frac{\omega E_{zn}}{\Omega_n} \exp[i(k_n z - \omega t)] \quad (92)$$

Equation 92 is the form of the perturbed current density when the system in Fig. 6, with electron flow equilibrium given by Eq. 72, experiences a linear perturbation in the form of Eq. 30. This result is used to derive the perturbed field harmonics.

Substituting expressions corresponding to Eq. 30 for E_{r1} , E_{z1} , $B_{\theta1}$ and J_{z1} into Eqs. 73 and 74 yields identically Eqs. 31-33 for the spatial harmonics. Thus, Eqs. 33, 40 and 41 remain valid, provided the J_{zn} are defined by Eq. 92. Similar to Section 3, Eqs. 30, 92 and 41 are used to eliminate J_{zn} and $B_{\theta n}$ from Eq. 33. After some algebra, the resulting equation is

$$\left(\frac{1}{r} \frac{d}{dr} r \frac{d}{dr} + r_n^{*2} \right) E_{zn} = 0 \quad (93)$$

where

$$r_n^{*2} = r_n^2 \left[1 - \frac{\omega_p^2 / \gamma_0^3}{\Omega_n^2} \right] \quad (94)$$

and $r_n^2 = \omega^2 / c^2 - k_n^2$. Expression 94 is a complicated function of r because $\omega_p = \omega_p(r)$, $\gamma_0 = \gamma_0(r)$, and $\Omega_n = \Omega_n(r) = \omega - V_z(r)k_n$. Definitions of $\omega_p(r)$, $\gamma_0(r)$, and $V_z(r)$ are given by Eqs. 16, 9 and 10, respectively. The appropriate vacuum equation is obtained by letting $\omega_p = 0$ in Eq. 94. Solving Eq. 93 in regions I and II of Fig. 6, subject to the condition in Eq. 58 with boundary condition $E_{zn}(r=r_c) = 0$, yields all allowed electromagnetic and space-charge modes.

Note that Eq. 93 can be derived from the Maxwell-fluid equations (Eqs. 25-29 in Section 3) for an arbitrary electron equilibrium assuming negligible transverse particle motion. Therefore, this assumption also applies to Eq. 93. Conditions under which the perturbed transverse motion can be neglected will occur when the space-charge equilibrium is devoid of large radially directed gradients in the density or in the velocity field. To first order, the perturbed charge density and velocity are given by $n_1 = \Delta r \partial n_0 / \partial r$ and $v_{z1} = \Delta r \partial v_{z0} / \partial r$, where n_0 and v_{z0} are equilibrium values, and Δr represents a radial displacement of a sheet of charge. If $\partial n_0 / \partial r$ and $\partial v_{z0} / \partial r$ are large, n_1 and v_{z1} will produce significant drifts in the transverse direction via the production of E_{r1} and $B_{\theta 1}$ field components. The resulting drift is due to a combination of equilibrium and perturbed fields.

Confining the present analysis to small radial gradients in the equilibrium is not too restrictive because, in the linear regime, the longitudinal interaction is so strong that it will be the dominant effect. However, by ignoring transverse effects, we have excluded the smooth-bore magnetron instability from the theory, the subject of which is adequately addressed in Ref. 26.

Because of the relative complexity of RBF equilibrium, Eq. 93 cannot be solved analytically in the region containing space charge. In the next section, we numerically solve Eq. 93 subject to the condition in Eq. 58 for the geometry corresponding to Fig. 6 and a variety of space-charge parameters.

6.0 NUMERICAL SOLUTION OF THE MILO DISPERSION RELATION FOR RBF EQUILIBRIUM

The general MILO dispersion relation, for any electron equilibrium, consists of Eq. 62 subject to condition 58. Expression 58 defines the matrix elements $D_{mn}(\omega, k_0)$ once the solution for the spatial harmonics of the axial electric field are known. The latter are determined by the choice of electron equilibrium.

In this section, we obtain dispersion relation solutions that include the physics of magnetically insulated electron flow, and make comparisons with numerical simulation. The procedure is similar to Section 5.0 except that the axial electric field spatial harmonics are determined by numerically solving Eq. 93 in regions I and II of Fig. 6. In region I, the space-charge parameters γ_0 , v_{z0} and ω_p^2 are given by expressions 9, 10 and 16, respectively. In region II, there is no space charge, so $\omega_p \equiv 0.0$. Using appropriate definitions of ω_p , Eq. 93 is numerically solved continuously out to the corrugated anode wall to obtain $E_{zn}[r_a(z)]$. This is part of an iterative process that continues until the roots of Eq. 62 are obtained.

The periodic structure dispersion code DISCODE was used, with appropriate modifications, to obtain solutions of Eq. 62 that include magnetically insulated electron flow. DISCODE was modified to solve Eq. 93 in place of evaluating the analytic solution obtained in Section 3. This is accomplished with the well-known Fehlberg Fourth-Fifth Order Runge-Kutta method (Ref. 27).

Because the E_{zn} may be complex valued, Eq. 93 represents a coupled pair of second-order differential equations. To facilitate the use of the above ODE solver, Eq. 93 is rewritten as a coupled system of four first-order differential equations. To determine the $D_{mn}(\omega, k_0)$, make the substitution $E_{zn}(r) = A_n f_n(r)$ in Eqs. 58 and 93, and numerically solve for $f_n(r)$. It is sufficient to evaluate the $f_n(r)$ to within an arbitrary constant. Any n -dependent constant can be incorporated into the A_n . Therefore, the initial value of df_n/dr is arbitrary. Hence, the initial condition $E_{zn}(r_c) = 0$ in addition to expression 58 are sufficient to determine $f_n(r)$ and corresponding roots of Eq. 62.

Velocity shear associated with RBF considerably complicates the numerical solution of Eq. 93. Recall that in Eq. 93 $\Omega_n = \omega - v_{z0} k_n$. Because v_{z0} varies from 0 at the cathode to some maximum (v_e) at the charge sheath radius (r_e), we see that Ω_n can be zero for a wide range of real ω for a given k_n ; therefore, $\Omega_n = 0$ corresponds to singularities of Eq. 93. Appendix D shows that these singularities are actually branch points which define a continuum of slow space-charge waves. Thus, the general dispersion relation is expected to consist of a continuous spectrum of slow space-charge waves with frequencies in the range $0 < \omega < v_{z0} k_0$, a single fast space-charge wave, and an infinite number of TM modes. It will be shown that the entire space-charge wave continuum is unstable, and that the relative insensitivity of growth rate to changes in MILO voltage is due to velocity shear in the electron flow.

6.1 DISPERSION RELATION SOLUTIONS INCLUDING THE EFFECTS OF RBF

We illustrate the effect of magnetically insulated flow on the MILO dispersion relation with several examples in which dispersion diagrams are obtained using DISCODE to solve Eqs. 62 and 93. Cases without space charge were covered in Section 4.0; hence, the following discussion is limited to problems containing insulated electron flow.

To gain an understanding of the space-charge wave spectrum without complications related to slow TM waves, we obtain the dispersion diagram corresponding to magnetically insulated electron flow in an infinitely long coaxial transmission line with $r_c = 6.5$ cm, $r_a = 9.1$ cm, $V_0 = 0.6$ MV, and $I_a = 59.0$ kA. Corresponding space-charge parameters are $r_e = 8.0$ cm, $I_e = -19.7$ kA, $\beta_e = 0.745$, and $\gamma_e = 1.5$. We obtained these values by specifying the electron sheath radius (r_e) and maximum electron velocity (β_e), and using appropriate equations in Section 2.1 to evaluate remaining parameters. Figure 22 represents the dispersion diagram corresponding to the previous parameter set. Only the space-charge wave spectrum is shown. Not shown is the spectrum of standard coaxial TM_{0n} waves. As pointed out above, the space-charge wave spectrum consists of a single fast mode plus a continuum. The dispersion diagram can be modified, as described in Section 4.0, by changing electron flow parameters. The continuum can be broadened or narrowed by changing β_e ,

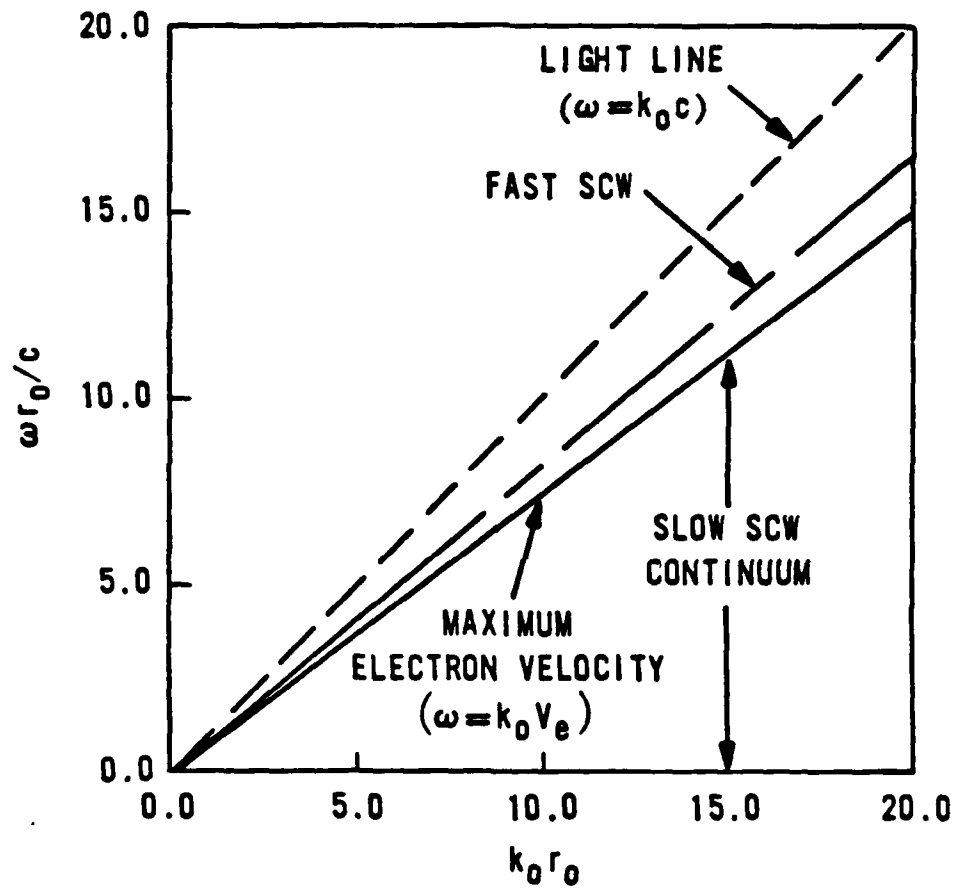


Figure 22. Dispersion diagram for space-charge waves associated with RBF.

but it is always present. When a slow-wave structure is added to the above configuration, instability is expected where the space-charge wave continuum crosses a slow electromagnetic mode.

Equation A-1 is used to add a sinusoidally rippled anode to the previous configuration. The slow wave structure parameters are $r_c = 6.5$ cm, $r_0 = 9.1$ cm, $\epsilon = 0.098901$, $d = 1.8$ cm, and $z_0 = 1.4$ cm. Electron flow parameters are the same as above, but the MILO voltage has been changed to $V_0 = 0.32$ MV. Figure 23 represents the dispersion diagram corresponding to this configuration and is a plot of oscillation frequency ν (not normalized) versus normalized wave number. The slow space-charge wave continuum occupies the region defined by $0 < 2\pi\nu/k_0 < \beta_e c$. Instability occurs where the continuum crosses a slow TM mode. The squares labeled A, B, and C in Fig. 23 mark the frequency and wave number of maximum growth corresponding to the first three TM modes. The oscillation frequencies ν and maximum normalized growth rates ω_c^* ($=\omega_c r_0/c$) of these points are shown in Table 1.

TABLE 1. Oscillation frequency and maximum growth rate of unstable TM modes in Fig. 23.

Mode	ν (GHz)	ω_c^*
A	4.1	0.48
B	8.9	0.04
C	12.6	0.09

Clearly, mode A is dominant, followed by C and B. The forward wave interactions are strongest because the flow of energy is in the forward direction. For a given MILO voltage, growth rates decrease rapidly for points either side of the wave number yielding maximum growth, similar to Figs. 14 and 15.

Except for the space-charge wave continuum, the addition of magnetically insulated flow does not appear to have significantly modified the MILO dispersion diagram. For a fixed value of β_e results are similar to those obtained in Section 4. However, a major difference in computed growth rates becomes evident when β_e is varied.

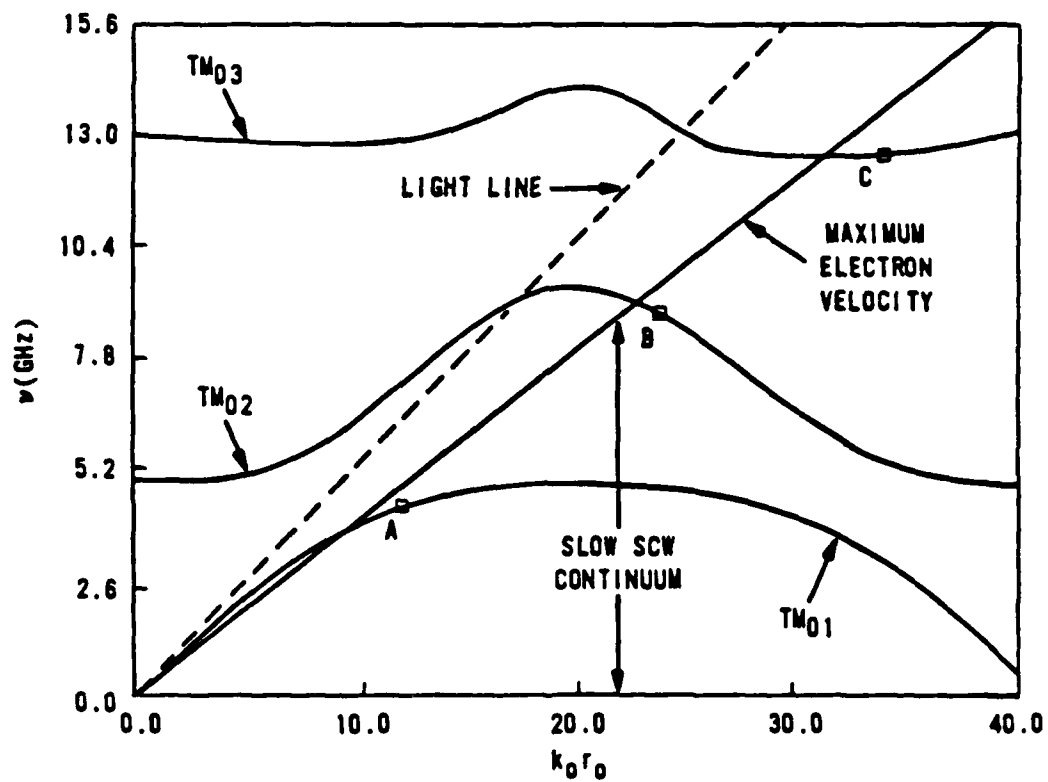


Figure 23. MILO dispersion diagram including the physics of RBF.

Table 2 summarizes the results of a parameter study that shows the sensitivity of growth rate to changes in electron sheath radius and, more importantly, MILO voltage. The periodic structure was generated with Eq. A-1. Corresponding parameters are $r_c = 1.0$ cm, $r_0 = 2.9$ cm, $\epsilon = 0.301345$, $d = 1.8$ cm, and $z_0 = 1.4$ cm. Values of space-charge parameters are given in the table.

TABLE 2. Dependence of growth rate on electron radius and MILO voltage.

Electron Radius (cm)	Maximum Velocity (β_e)	MILO Voltage (MV)	Normalized Growth Rate (ω_c^*)
1.5	0.585	0.3	0.017
1.5	0.929	2.4	0.096
1.5	0.989	9.5	0.094
1.9	0.585	0.2	0.111
1.9	0.929	1.0	0.219
1.9	0.989	3.7	0.182

The data in Table 2 are divided into two groups determined by the value of r_e . Within each group the MILO voltage and corresponding maximum electron velocity take on a wide range of values. Consistent with the results in Section 4.0, the position of the electron radius has a significant effect on growth rate. In contrast to the monoenergetic beam case (compare Figs. 14 and 15), the maximum growth rate does not significantly decrease with increasing voltage. In fact, the growth rate increases to a maximum value, then decreases very slowly with increasing voltage. This is the expected behavior, and is due entirely to the velocity shear present in magnetically insulated flow. Because of velocity shear, there will always be a resonant layer of electrons to interact with the fundamental TM mode, so long as β_e is above the value necessary to produce forward waves ($d\omega/dk_0 > 0$).

6.2 COMPARISON WITH NUMERICAL SIMULATION II

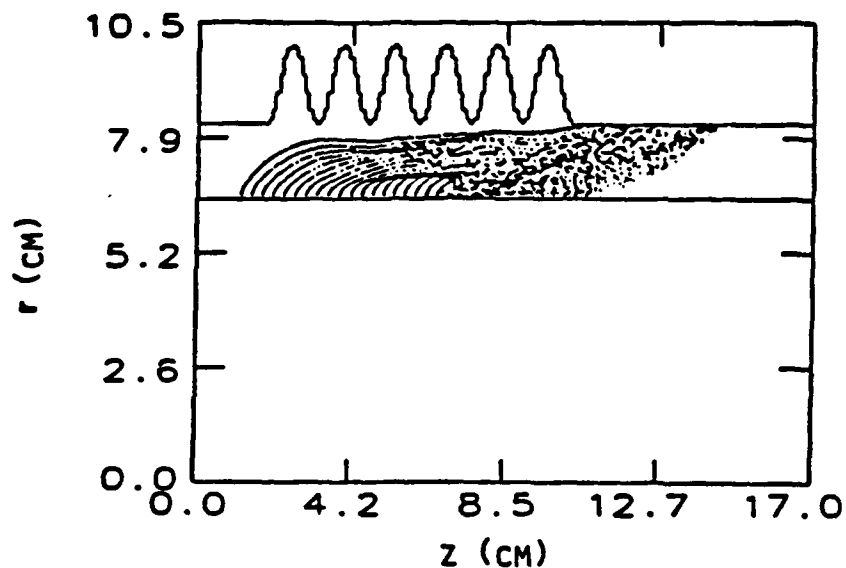
Since a realistic model of electron flow has been incorporated into the analytic theory, more meaningful comparisons with numerical simulation can be made. The results represented by Fig. 23 were compared with an ISIS simulation

of the corresponding geometry; and in this case, we were able to simulate the sinusoidally rippled anode. The simulation procedure is identical to that described in Section 4.2.

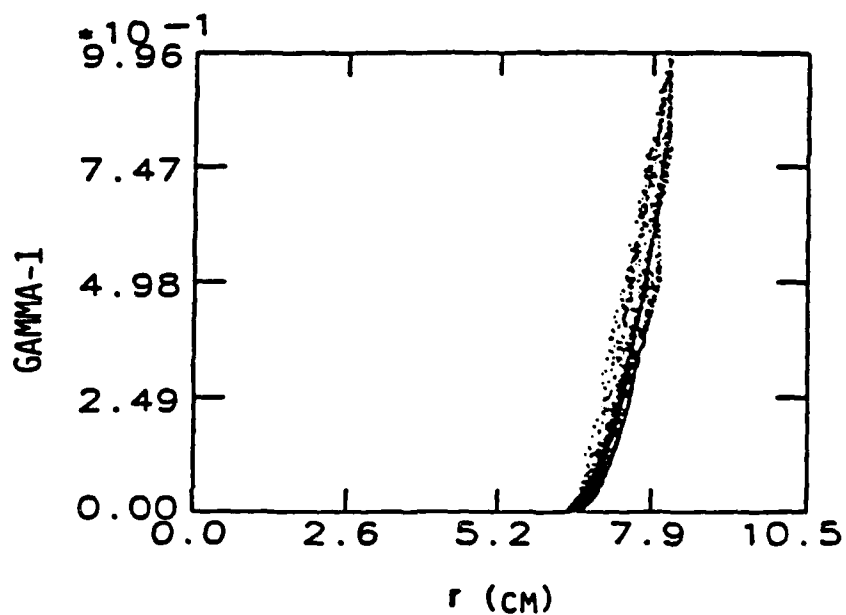
Figure 24a is a plot of simulation particles (electrons) on the MILO geometry corresponding to Fig. 23, and represents a snapshot taken 2.2 ns into the simulation. Recall that $r_c = 6.5$ cm, A-K gap = 1.7 cm, $d = 1.8$ cm, and $z_0 = 1.4$ cm. The electron flow is approximately in equilibrium because the perturbed electric field amplitude is still very small. From Fig. 24a, the electron sheath radius is estimated to be $r_e = 8.0$ cm. Note that the electron flow near the anode slots is approximately laminar. Knowing r_e , we estimate γ_e using Fig. 24b, which is a plot of particle kinetic energy (normalized to $m_e c^2$) versus radius. Using $r_e = 8.0$ cm, we obtain $\gamma_e = 1.5$. Additional relevant simulation parameters are $V_0 = 0.47$ MV, $I_a = 55.4$ kA, and $I_e = -30.8$ kA. The simulation equilibrium agrees very well with the insulated flow used to obtain Fig. 23. The electron current is 50 percent higher in the simulation, but does not have a significant effect on the results.

Similar to Section 4.2, the time history of the axial electric field is monitored to observe the evolution of the instability. Figures 25a and 25b respectively represent the time history and corresponding spectrum of the axial electric field at the midpoint of the entrance to slot three in Fig. 24a (counting from left to right). Figure 25a shows that the instability is in the linear regime, growing exponentially in time. Assuming $E_z \propto \exp(\omega_c t)$, we estimate that $\omega_c = 5.3 \times 10^8 \text{ s}^{-1}$ ($\omega_c^* = 0.16$) for the total growth rate. Comparison with mode A in Table 1 indicates a factor of 3 difference in the analytic prediction. This difference may be due to: (1) slightly nonlaminar electron orbits observed in the simulation, (2) the fact that the analytic model ignores first-order transverse motion of electrons, or (3) a combination of these effects.

Figure 25b shows the frequencies of the first three electromagnetic modes ($TM_{01} - TM_{03}$) to be $\nu_A = 4.4$ GHz, $\nu_B = 9.0$ GHz, and $\nu_C = 12.9$ GHz. Comparison with Table 1 shows that these frequency values are in excellent agreement with analytic theory. In addition, the relative amplitude of modes observed in the

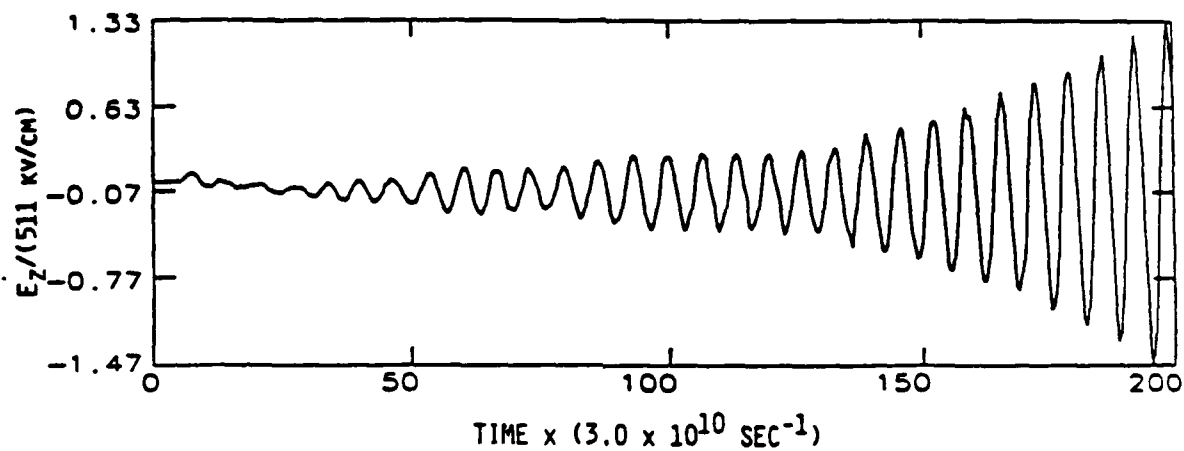


(a) Configuration space.

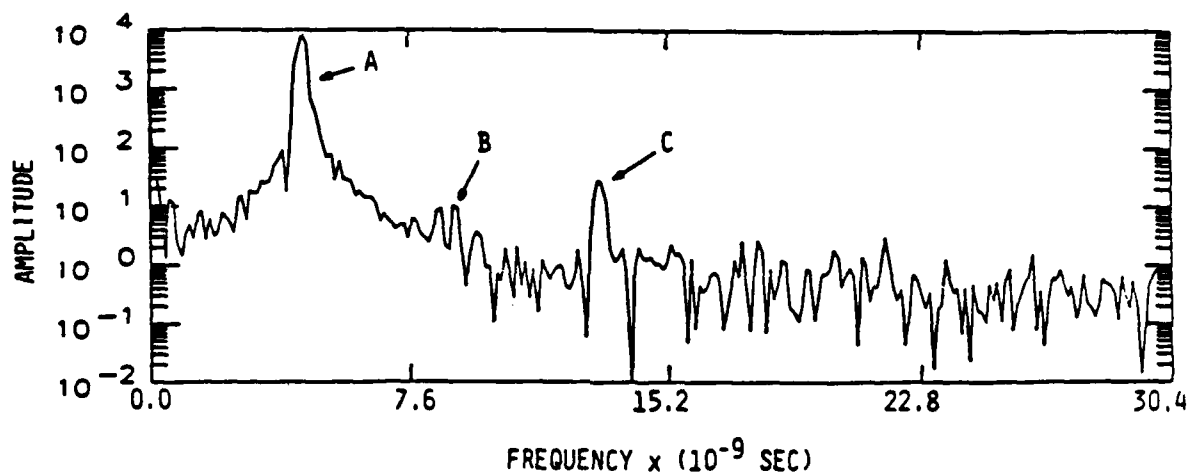


(b) Particle kinetic energy vs. r .

Figure 24. ISIS MILO simulation results showing details of electron flow.



(a) Time history.



(b) Spectrum.

Figure 25. ISIS MILO simulation results showing details of the axial electric field spectrum.

spectrum qualitatively agrees with the growth rates given in Table 1; that is, in the simulation we observe the order of dominance predicted by theory.

In general, the analytic theory including RBF equilibrium provides a very good description of the linear regime in MILO simulations. With a relatively simple model, we can predict oscillation frequency, growth rate, relative mode strength, mode of oscillation, and sensitivities to various parameters.

7.0 CONCLUSIONS

Using Maxwell's equations and Floquet's theorem for periodic structures, we derived a dispersion relation for transverse magnetic (TM) waves propagating in a coaxial, magnetically insulated transmission line oscillator (MILO). The dispersion relation, Eqs. 58 and 62, is written in terms of the axial electric field space harmonics $[E_{zn}(r)]$ evaluated on the periodic anode surface. All space-charge effects are contained in the differential equation for the $E_{zn}(r)$.

Modeling the electron flow with a thin, monoenergetic electron beam allowed us to obtain analytic solutions to the axial electric field differential equation. Using analytic expressions for the $E_{zn}(r)$, we numerically solved the dispersion relation for the purpose of obtaining dispersion diagrams corresponding to various MILO geometries and thin beam parameters. The dispersion diagrams accurately show the presence of slow TM waves, fast TM waves, and space-charge waves. In addition, they clearly indicate that microwaves generated in the MILO are the result of an unstable interaction involving slow TM modes with slow space-charge waves.

The thin-beam dispersion relation accurately predicts MILO mode structure, oscillation frequency, and mode of oscillation. However, it fails to predict the dependence of growth rate on MILO voltage observed in numerical simulation. Growth rates predicted with the thin-beam dispersion relation rapidly decrease with increasing MILO voltage, a consequence of using monoenergetic electron flow. Numerical simulations of the MILO, which accurately model magnetically insulated flow, show little variation in the growth rate over a wide range of transmission line voltages. The difference in theory and simulation is attributed to using a thin, monoenergetic electron beam to approximate magnetically insulated flow.

In an attempt to eliminate the discrepancy between theory and simulation, the thin-beam dispersion relation was modified to include a realistic model of magnetically insulated electron flow. In this model, known as relativistic Brillouin flow (RBF), electrons drift in a sheath along equipotential lines.

An important feature of RBF is velocity shear. The velocity of electrons in the flow varies from zero at the cathode to some maximum value at the edge of the charge sheath.

Incorporating RBF into the dispersion relation did not modify the MILO TM mode structure; however, it had a significant effect on space-charge modes. The single slow space-charge wave associated with monoenergetic beams was replaced with a continuum of slow space-charge waves, a result of the velocity distribution in RBF. Numerical solutions of the dispersion relation including RBF showed the entire space-charge wave continuum to be unstable. Furthermore, it was shown that the peak growth rate was insensitive to MILO voltage as long as the corresponding maximum electron velocity remained above the threshold for a forward wave interaction. This result agrees with numerical simulation, and is a consequence of velocity shear present in magnetically insulated flow.

The dispersion relation including the physics of RBF was used to make accurate predictions of MILO behavior, as confirmed by numerical simulation, and represents the main result of this work.

REFERENCES

1. Bekefi, G.; and Orzechowski, T.J.; Proceedings, of the 1st IEEE International Pulsed Power Conference, Lubbock, TX, 9-11 November 1976.
2. Meek, J.M.; and Craggs, J.D.; Electrical Breakdown of Gases, Chap. 11, p. 839, J. Wiley & Sons, New York, 1978.
3. Kirstein, P.T.; Kino, G.S.; and Waters, W.E.; Space Charge Flow, McGraw-Hill, New York, 1967.
4. Mendel, Jr, C.W.; Seidel, D.B.; and Rosenthal, S.E.; Laser and Particle Beams 1(3), p. 311, 1983.
5. Creedon, J.M., J. Appl. Phys. 48(3), p. 1070, 1977.
6. Creedon, J.M., J. Appl. Phys. 46(7), p. 2946, 1975.
7. Mendel, Jr., C.W.; Seidel, D.B.; and Slutz, S.A.; Phys. Fluids 26(12), p. 3628, 1983.
8. Ron, A.; Mondelli, A.A.; and Rostoker, N.; IEEE Trans Plasma Sci PS-1, p. 85, 1973.
9. Krall, N.A.; and Trivelpiece, A.W.; Principles of Plasma Physics, p. 171, San Francisco Press, San Francisco, California, 1986.
10. Godfrey, B.B.; IEEE Trans Plasma Sci PS-7(1), 1979.
11. Swegle, J.A.; Poukey, J.W.; and Leifeste, G.T.; Phys. Fluids 28(9), p. 2882, 1985.
12. Okress, E., Crossed-Field Microwave Devices, Academic Press, New York, 1961.
13. Atwater, H.A., Introduction to Microwave Theory, McGraw-Hill, New York, 1962.
14. Hutter, R., Beam and Microwave Electronics in Microwave Tubes, D. Van Nostrand Company, Inc., Princeton, New Jersey, p. 107, 1960.
15. Alfven, H., Phys. Rev. 55, p. 425, 1939.
16. Arfken, G., Mathematical Methods for Physicists, Academic Press, Orlando, Florida, p. 578, 1985.
17. Arfken, G., Mathematical Methods for Physicists, Academic Press, Orlando, Florida, p. 599, 1985.
18. Kurilko, V.I.; Kuchurov, V.I.; Ostrovskii, A.O.; and Tkach, Yu. V.; Sov. Phys. Tech. Phys. 24(12), p. 1451, 1979.

REFERENCES (Concluded)

19. Godfrey, B.B., Newton-Raphson Root Solver and CTSS Interface for Dispersion Relation Programs, Mission Research Corporation Report AMRC-N-368, Albuquerque, New Mexico, 1987.
20. Muller, D.E., Math. Tables Aids Comput. 10, p. 208, 1956.
21. Henrici, P., Elements of Numerical Analysis, John Wiley & Sons, Inc., New York, p. 84, 1964.
22. Beck, A.H.W., Space Charge Waves and Slow Electromagnetic Waves, Pergamon Press, New York, p. 103, 1958.
23. Gisler, G.; Jones, M.E.; and Snell, C.M.; Bull. Am. Phys. Soc. 29, p. 1208, 1984.
24. Jones, M.E.; and Peter, W.K.; IEEE Trans. Nucl. Sci. NS-32, p. 1794, 1985.
25. Davidson, R.C., Theory of Nonneutral Plasmas, W.A. Benjamin, Inc., Reading, Massachusetts, 1974.
26. Swegle, J., Phys. Fluids 26(6), p. 1670, 1983.
27. Shampine, L.F.; and Watts, H.A.; Design of a User Oriented Package of ODE Solvers, Sandia National Laboratories Report SAND79-2374, Albuquerque, New Mexico, 1979.
- A-1. Arfken, G., Mathematical Methods for Physicists, Academic Press, Orlando, Florida, p. 787, 1985.
- B-1. Arfken, G., Mathematical Methods for Physicists, Academic Press, Orlando, Florida, p. 489, 1985.
- D-1. Pearson, Karl, Messenger of Mathematics 9, p. 129, 1880.
- D-2. Abramowitz, M.; and Stegun, I.A.; Handbook of Mathematical Functions, U.S. Government Printing Office, Washington, D.C., p. 360, 1970.
- D-3. Arfken, G., Mathematical Methods for Physicists, Academic Press, Orlando, Florida, p. 397, 1985.

APPENDIX A

PERIODIC ANODE FUNCTIONS USED IN MILO STABILITY ANALYSIS

The following is a list of functions used to model the periodic anode in MILO devices.

1. SINUSOIDAL

The anode wall function is given by

$$r_a(z) = r_0[1 + \epsilon \cos(h_0 z)] \quad (A-1)$$

where $h_0 = 2\pi/z_0$ and z_0 represents the structure period. The minimum, maximum, and average radii are given by $r_0(1-\epsilon)$, $r_0(1+\epsilon)$, and r_0 , respectively. The slot depth d is given by $d = 2r_0\epsilon$ and is obviously determined by the parameter ϵ for a given r_0 . Depicted in Fig. A-1, the anode modeled by Eq. A-1 has equal slot and vane widths.

2. SQUARE WAVE

To avoid complications related to the Gibbs phenomenon (Ref. A-1), we do not model a square wave using Fourier series, but instead use the function

$$r_a(z) = r_0 \left\{ 1 + \epsilon \tanh \left[\tan^{2m} \left(\frac{1}{2} h_0 z \right) \right] \right\} \quad (A-2)$$

where $m = 1, 2, 3, \dots$, and h_0 is as before. Expression A-2 has period z_0 and models a square wave to any degree desired by choosing an appropriate value of m ; typically, $m = 4$ is adequate. This yields a square wave anode wall with equal vane and slot widths. The slot depth d is given by $d = r_0(1+\epsilon)$. Figure A-2 is an example of a structure generated by Eq. A-2.

3. DOUBLE HYPERBOLIC TANGENT

The double hyperbolic tangent function is the most versatile of functions presented here. It can be used to model periodic anodes having slot widths equal

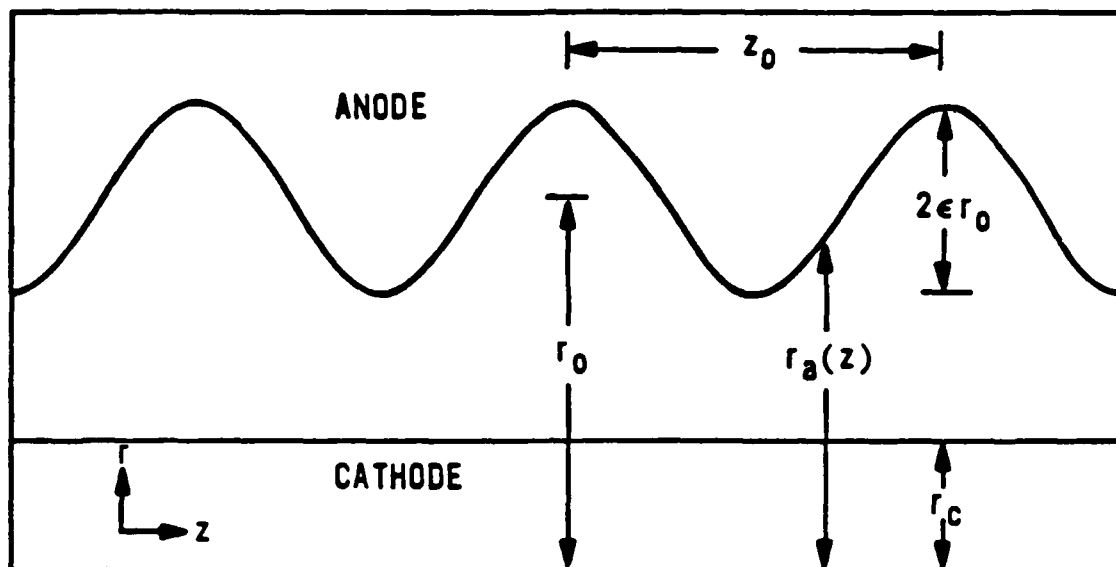


Figure A-1. Sinusoidal model of a MILO.

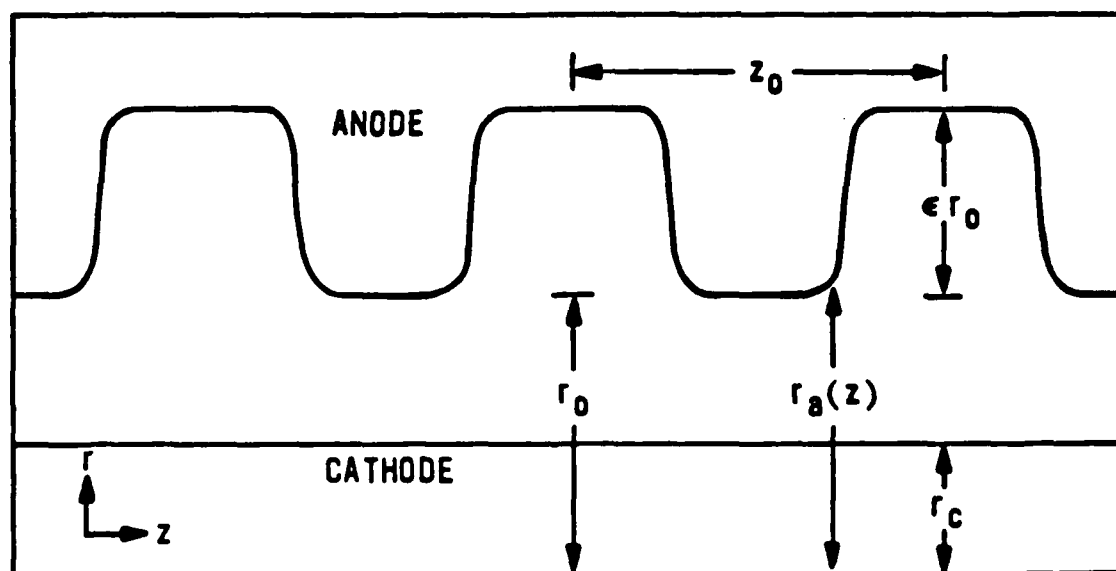


Figure A-2. Square-wave model of a MILO.

to or different than vane widths. The primary part of this function is given by

$$f(z) = \eta \tanh \left\{ a \sin^2 \left[\frac{1}{4} h_0 (z - z_s) \right] \right\} \tanh \left\{ a \cos^2 \left[\frac{1}{4} h_0 (z - z_s) \right] \right\} \quad (\text{A-3})$$

where $\eta = d/\tanh^2(a/2)$ is a normalization factor, d is the slot depth, z_s is a constant that shifts the function relative to the origin, a is a constant used to shape the anode, and h_0 is as before. The function $f(z)$ has period z_0 . Anodes with wide slots and narrow vanes can be modeled by setting $z_s = z_0/2$ in Eq. A-3 and letting

$$r_a(z) = r_0 - d/2 + f(z) \quad (\text{A-4})$$

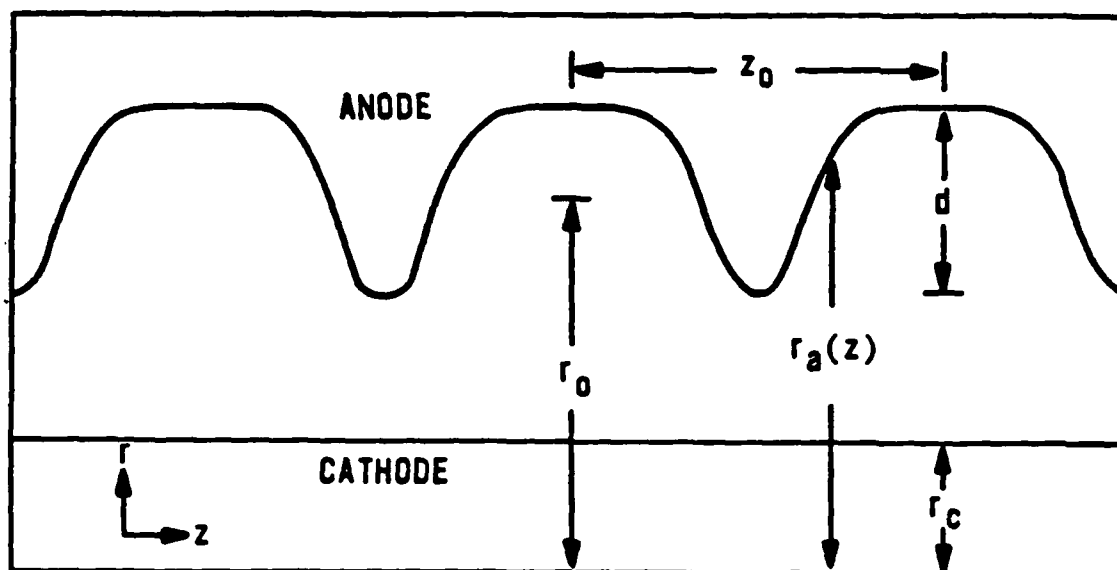
where r_0 is the average anode radius. Then, choosing $a > 1$ will cause the slots to be wider than vanes, illustrated in Fig. A-3(a).

The opposite case of narrow slots and wide vanes is obtained by choosing $z_s = 0$ in Eq. A-3 and setting

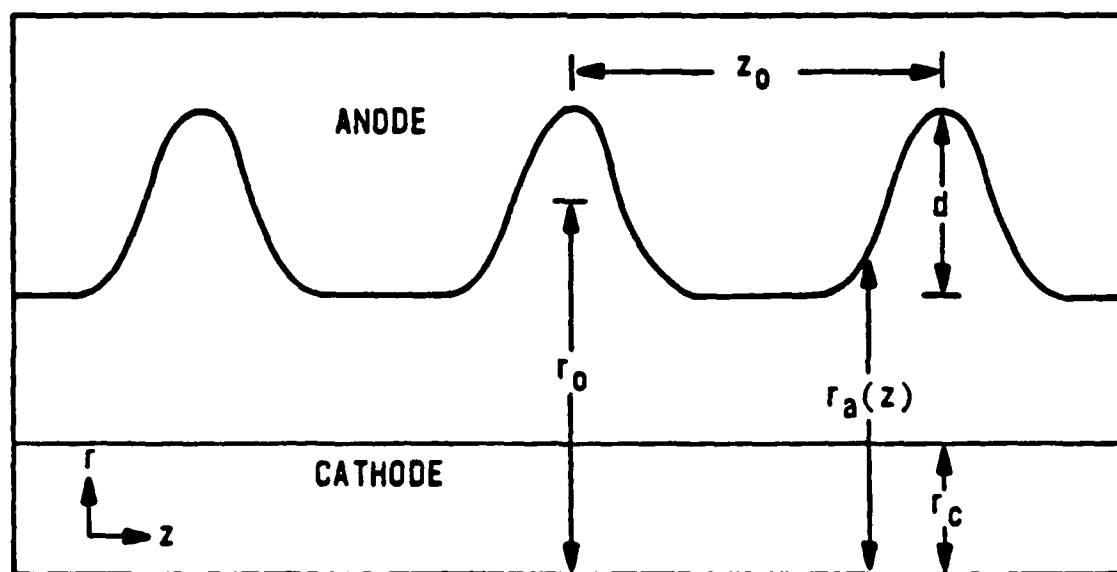
$$r_a(z) = r_0 + d/2 - f(z) \quad (\text{A-5})$$

with r_0 defined as before. Choosing $a > 1$ causes vanes to be wider than slots, illustrated in Fig. A-3(b).

Equal slot and vane widths can be obtained using either Eq. A-4 or A-5 with $a = 1$.



(a) Slots wider than vanes.



(b) Vanes wider than slots.

Figure A-3. Double hyperbolic tangent model of a MIL0.

APPENDIX B

EQUILIBRIUM DISTRIBUTION FUNCTION FOR RELATIVISTIC BRILLOUIN FLOW (RBF)

A distribution function corresponding to RBF is arrived at by considering the inherent physics assumptions involved. Noting that any function depending only on constants of the motion is a solution to Vlasov's equation, we guess the form of a distribution function to within an arbitrary normalization constant. The arbitrary constant is determined by forcing RBF expressions for the electric and magnetic potentials to solve Maxwell's equations with source terms determined by taking moments of the distribution function.

As was pointed out in Section 2.1, RBF is one-dimensional and is characterized by the assumption that all electrons have the same constant Hamiltonian (H) and canonical momentum (P_z). Furthermore, it is assumed that $P_z = 0$ for all electrons in the flow. Based on these assumptions, we guess that the form of the equilibrium distribution function (f_0), in cylindrical coordinates, must be

$$f_0(r, \vec{p}) = n(r) \delta(H - mc^2 + P_z) \delta(p_r) \delta(p_\theta) \quad (B-1)$$

where δ represents the Dirac delta-function, p_i the i th component of ordinary momentum, $n(r)$ is a normalization constant, $H = c(m^2 c^2 + p_z^2)^{1/2} - e\phi(r)$, $P_z = \gamma m v_z - eA_z(r)$, and $\gamma = 1/(1 - v_z^2/c^2)^{1/2}$. The relativistically correct expression for v_z is given by

$$v_z = \frac{cp_z}{(m^2 c^2 + p^2)^{1/2}} \quad (B-2)$$

The functions $\phi(r)$ and $A_z(r)$ respectively represent the radially dependent equilibrium electric and magnetic potentials defined in Section 2.1. Note that because the flow is laminar any function of r is a constant of the motion.

Expression (B-1) represents any equilibrium satisfying the above condition. We now determine $n(r)$ such that (B-1) corresponds to RBF. This requires that expressions for $\phi(r)$ and $A_z(r)$ given in Section 2.1 satisfy

$$\frac{1}{r} \frac{d}{dr} r \frac{d}{dr} \phi(r) = -4\pi\rho(r) \quad (B-3)$$

$$\frac{1}{r} \frac{d}{dr} r \frac{d}{dr} A_z(r) = -\frac{4\pi}{c} J_z(r) \quad (B-4)$$

with source terms given by

$$\rho(r) = -e \int_{-\infty}^{\infty} \int_{-\infty}^{\infty} \int_{-\infty}^{\infty} dp_z dp_\theta dp_r f_0(r, \vec{p}) \quad (B-5)$$

and

$$J_z(r) = -e \int_{-\infty}^{\infty} \int_{-\infty}^{\infty} \int_{-\infty}^{\infty} dp_z dp_\theta dp_r v_z f_0(r, \vec{p}) \quad (B-6)$$

Equations B-3 and B-4 are the equilibrium Maxwell's equations for the MITL problem discussed in Section 2.1.

The mechanics of evaluating the integrals in Eqs. B-5 and B-6 are similar; therefore, we present details of obtaining $\rho(r)$ and simply write down the expression for $J_z(r)$.

Before proceeding, we define

$$g(r) = e\phi(r) + mc^2 - eA_z(r) \quad (B-7)$$

and

$$F(p_z) = c \left(m^2 c^2 + p_z^2 \right)^{1/2} - cp_z - g(r) \quad (B-8)$$

where we have left the r dependence of F implicit.

Substituting Eq. B-1 into B-5 and performing the integrals over p_r and p_θ yields

$$\rho(r) = -e_n(r) \int_{-\infty}^{\infty} dp_z \delta[F(p_z)] \quad (B-9)$$

Evaluation of the previous integral is complicated by the fact that the argument of the delta-function is a function rather than a variable. This difficulty is overcome using the relation (Ref. B-1)

$$\delta[F(p_z)] = \frac{\delta(p_z - p_{z0})}{\left| \frac{dF}{dp_z} \right|} \quad (B-10)$$

where p_{z0} is the solution to $F(p_{z0}) = 0$. Setting the right-hand side of Eq. B-8 equal to zero yields, after some algebra,

$$c(p_{z0}^2 + m^2 c^2)^{1/2} = cp_{z0} + g(r) \quad (B-11)$$

Squaring the previous equation and solving for $2cp_{z0}$ yields

$$2cp_{z0} = \frac{m^2 c^4 - g^2(r)}{g(r)} \quad (B-12)$$

Using Eq. B-10 in expression B-9 yields

$$\rho(r) = - \frac{e_n(r)}{\left| \frac{dF}{dp_z} \right|} \bigg|_{p_z = p_{z0}} \quad (B-13)$$

where

$$\frac{dF}{dp_z} = c \left[\frac{cp_z}{c(p_z^2 + m^2 c^2)^{1/2}} - 1 \right] \quad (B-14)$$

We evaluate Eq. B-14 at $p_z = p_{z0}$ and eliminate p_{z0} from the resulting expression using Eqs. B-11 and B-12 to get

$$\left. \frac{dF}{dp_z} \right|_{p_z=p_{z0}} = - \frac{2cg^2(r)}{m^2c^4 + g^2(r)} \quad (B-15)$$

Substituting Eq. B-15 into Eq. B-13 yields

$$\rho(r) = - \frac{en(r)}{2c} \left[\frac{m^2c^4 + g^2(r)}{g^2(r)} \right] \quad (B-16)$$

for the total charge density.

The procedure for evaluating the current density integral is identical to the one used for $\rho(r)$; omitting the details gives the following expression for the equilibrium current density

$$J_z(r) = - \frac{en(r)}{2} \left[\frac{m^2c^4 - g^2(r)}{g^2(r)} \right] \quad (B-17)$$

With $n(r)$ known, Eqs. B-3 and B-4 could be solved using source terms given by B-16 and B-17 to obtain the equilibrium potentials. The object here, though, is to determine $n(r)$ such that it corresponds to RBF equilibrium. Thus, we uniquely determine $n(r)$ by substituting the expression for $\phi(r)$, Eq. 11, and source term B-16 into Eq. B-3; performing the differentiation and solving for $n(r)$ yields

$$n(r) = \frac{mc^3}{2\pi e^2} \left(\frac{A}{r} \right)^2 \left[\frac{g^2(r)/m^2c^4}{1 + g^2(r)/m^2c^4} \right] \cosh \left[\ln \left(\frac{r}{r_c} \right)^A \right] \quad (B-18)$$

Writing $g(r)$ in terms of the hyperbolic expressions for $\phi(r)$ and $A_z(r)$ (Section 2.1), $g(r)/mc^2 = (r_c/r)^A$. Thus,

$$\frac{g^2(r)/m^2c^4}{1 + g^2(r)/m^2c^4} = \frac{(r_c/r)^{2A}}{1 + (r_c/r)^{2A}} = \frac{(r_c/r)^A}{2 \cosh \left[\ln (r/r_c)^A \right]} \quad (B-19)$$

Using Eq. B-19 in B-18 produces the desired result

$$n(r) = \left(\frac{mc^3}{4\pi e^2} \right) \left(\frac{A}{r} \right)^2 \left(\frac{r_c}{r} \right)^A \quad (B-20)$$

Expression B-1 with normalization constant $n(r)$ given by Eq. B-20 represents the distribution function for RBF, and can be used to determine all properties of the equilibrium.

APPENDIX C

EVALUATION OF THE PERTURBED CURRENT DENSITY INTEGRAL $I_n^*(f_0)$

In this section, we are concerned with evaluating integrals of the form

$$I_n^*(f_0) = \int_{-\infty}^{\infty} \int_{-\infty}^{\infty} \int_{-\infty}^{\infty} dp_z dp_\theta dp_r \frac{v_z}{(\omega - v_z k_n)} \frac{\partial f_0}{\partial p_z} \quad (C-1)$$

when f_0 is given by Eq. 72. The velocity v_z in Eq. C-1 must be considered as a function of p_z . The relativistically correct relationship is given by Eq. B-2.

Expression C-1 can be cast into a form that is easily evaluated by the method given in Appendix B. We define $g(r)$ and $F(p_z)$ as in Eqs. B-7 and B-8, respectively. Noting that

$$-\frac{\partial}{\partial k_n} \ln(\omega - v_z k_n) = \frac{v_z}{(\omega - v_z k_n)} \quad (C-2)$$

we rewrite Eq. C-1 as

$$I_n^*(f_0) = -\frac{\partial}{\partial k_n} \int_{-\infty}^{\infty} \int_{-\infty}^{\infty} \int_{-\infty}^{\infty} dp_z dp_\theta dp_r \ln(\omega - v_z k_n) \frac{\partial f_0}{\partial p_z} \quad (C-3)$$

Using the definition of v_z given by Eq. B-2, we integrate Eq. C-3 by parts to get

$$\begin{aligned} I_n^*(f_0) = & -f_0 \frac{\partial}{\partial k_n} \ln(\omega - v_z k_n) \Big|_{-\infty}^{\infty} \\ & - m^2 c^3 \frac{\partial}{\partial k_n} \int_{-\infty}^{\infty} \int_{-\infty}^{\infty} \int_{-\infty}^{\infty} dp_z dp_\theta dp_r G(p_z, k_n) f_0 \end{aligned} \quad (C-4)$$

where

$$G(p_z, k_n) = \frac{k_n}{\left[\omega (p_z^2 + m^2 c^2)^{1/2} - c k_n p_z \right] (p_z^2 + m^2 c^2)} \quad (C-5)$$

The first term on the right-hand side of Eq. C-4 is zero because we do not allow electrons with infinite momentum; that is, $f_0(p_z = \pm\infty) = 0$.

Substituting Eq. 72 for f_0 into Eq. C-4 and performing the integrals over p_r and p_θ yields

$$I_n^*(f_0) = -m^2 c^3 n(r) \frac{\partial}{\partial k_n} \int_{-\infty}^{\infty} dp_z G(p_z, k_n) \delta[F(p_z)] \quad (C-6)$$

where $n(r)$ is given by Eq. B-20. Using Eq. B-10, the integral in Eq. C-5 is easily evaluated giving

$$I_n^*(f_0) = -m^2 c^3 \frac{n(r)}{\left| \frac{dF}{dp_z} \right|_{p_z=p_{z0}}} \frac{\partial}{\partial k_n} G(p_{z0}, k_n) \quad (C-7)$$

with p_{z0} given by Eq. B-12. Differentiating $G(p_{z0}, k_n)$ with respect to k_n yields

$$\frac{\partial}{\partial k_n} G(p_{z0}, k_n) = \frac{\omega}{\left[\omega(p_{z0}^2 + m^2 c^2)^{1/2} - ck_n p_{z0} \right]^2 (p_{z0}^2 + m^2 c^2)^{1/2}} \quad (C-8)$$

Substituting Eq. C-8 and the absolute value of Eq. B-14 into Eq. C-7 yields

$$I_n^*(f_0) = - \frac{m^2 c^2 \omega n(r)}{\left[\omega(p_{z0}^2 + m^2 c^2)^{1/2} - ck_n p_{z0} \right]^2 \left[(p_{z0}^2 + m^2 c^2)^{1/2} - p_{z0} \right]} \quad (C-9)$$

Using Eqs. B-11 and B-12, C-9 can be rewritten as

$$I_n^*(f_0) = - \frac{4m^2 c^3 \omega n(r) g(r)}{\left[(\omega/c - k_n) m^2 c^4 + (\omega/c + k_n) g^2(r) \right]^2} \quad (C-10)$$

Substitution of Eq. C-10, with $n(r)$ given by Eq. B-20, into Eq. 86 yields Eq. 88 for the perturbed current density.

APPENDIX D

ANALYSIS OF SOLUTIONS TO EQUATION 93 ABOUT SINGULAR POINTS

This section shows that solutions to Eq. 93 in the space-charge region remain finite at singular points, and that these singularities are actually branch points of the associated dispersion relation. In addition, the relationship between branch points and the space-charge wave continuum is discussed.

Equation 93 can be simplified considerably by transforming to the coordinate ρ defined in Section 2.1 as

$$\rho = \ln \left[\left(\frac{r}{r_c} \right)^A \right] \quad (D-1)$$

Then,

$$\frac{1}{r} \frac{d}{dr} r \frac{d}{dr} E_{zn} = \left(\frac{A}{r_c} \right)^2 e^{-2\rho/A} \frac{d^2}{d\rho^2} E_{zn} \quad (D-2)$$

Substituting Eq. D-2 and Eqs. 94, 9, 10 and 16 into Eq. 93 yields

$$\left\{ \frac{d^2}{d\rho^2} + \Gamma_n^2 \left[\left(\frac{r_c}{A} \right)^2 e^{2\rho/A} - f_n(\rho) \right] \right\} E_{zn} = 0 \quad (D-3)$$

where

$$f_n(\rho) = \frac{\text{sech}^2(\rho)}{[\omega/c - k_n \tanh(\rho)]^2} \quad (D-4)$$

and

$$\Gamma_n^2 = \omega^2/c^2 - k_n^2 \quad (D-5)$$

Equation D-3 has no singular points when ω is complex, and is therefore well behaved in the case of instability. However, when ω is real, singularities occur at points ρ_0 given by

$$\rho_0 = \operatorname{arctanh} \left(\frac{\omega/c}{k_n} \right) \quad (D-6)$$

The real frequency solutions to the dispersion relation determine the behavior of space-charge waves away from unstable points on the dispersion diagram. Hence, we investigate solutions to Eq. D-3 at the singular points.

In Eq. D-3, we make the transformation $\rho = \rho_0 + z$ where $z \ll 1$, and expand the coefficient of E_{zn} in a Taylor series about the point $z = 0$. To second order in z , we have

$$f_n(\rho_0 + z) \approx -\frac{1}{r_n^2} \left[\frac{1}{z^2} - \frac{1}{3} + \frac{1}{15} z^2 + \dots \right] \quad (D-7)$$

and

$$e^{2(\rho_0 + z)/A} \approx e^{2\rho_0/A} \left[1 + \frac{2}{A} z + \frac{1}{2} \left(\frac{2}{A} z \right)^2 + \dots \right] \quad (D-8)$$

For z approximately zero, the behavior of solutions to Eq. D-3 will be dominated by terms of order less than one (in z) in the above series expansions. Thus, ignoring all higher order terms, Eq. D-3 transforms to

$$\left\{ \frac{d^2}{dz^2} + \left[\frac{K_1}{z^2} + K_2 \right] \right\} E_{zn} = 0 \quad (D-9)$$

where $K_1 = 1$ and $K_2 = (r_n r_0/A)^2 - 1/3$. The constant r_0 is defined by Eq. D-1 with $\rho = \rho_0$.

The exact solution to Eq. D-9 is given by Ref. D-1

$$E_{zn} = z^{1/2} \left[A_n J_{1/3/2}(K_2 z) + B_n Y_{1/3/2}(K_2 z) \right] \quad (D-10)$$

where J and Y represent Bessel's functions of the first and second kind, respectively.

We are interested in the behavior of Eq. D-10 as z goes to zero. For small arguments, the Bessel functions can be written as (Ref. D-2)

$$J_{i\sqrt{3}/2}(k_2 z) \approx \frac{\left(\frac{1}{2}k_2 z\right)^{i\sqrt{3}/2}}{\Gamma(1+i\sqrt{3}/2)} \quad (D-11)$$

and

$$Y_{i\sqrt{3}/2}(k_2 z) \approx -\frac{1}{\pi} \frac{\Gamma\left(i\frac{\sqrt{3}}{2}\right)}{\left(\frac{1}{2}k_2 z\right)^{i\sqrt{3}/2}} \quad (D-12)$$

where Γ represents the gamma function. Any quantity raised to a power can be written in terms of an exponential. Thus,

$$(k_2 z)^{\pm i\sqrt{3}/2} = e^{\pm(i\sqrt{3}/2)\ln(k_2 z)} \quad (D-13)$$

Clearly, as z approaches zero, Eq. D-13 oscillates rapidly, but remains bounded in the process. It follows that, in the limit as z goes to zero in Eq. D-10, the Bessel functions remain bounded and, because of the $z^{1/2}$ factor, the solution approaches zero. Thus, Eq. D-10 is a valid solution for E_{zn} near singular points in the space-charge region.

The singularities are manifest in the derivative of Eq. D-10 with respect to z . Because of the $z^{1/2}$ dependence, the derivative of Eq. D-10 with respect to z diverges as z approaches zero. The singular points (ρ_0) are actually branch points (Ref. D-3), and represent branch points of the dispersion relation (Ref. 10).

The existence of a space-charge wave continuum depends on the electron velocity distribution and not on the presence of a slow wave structure. Hence, to establish the frequency range in which branch points occur, we set $n=0$ in Eq. D-4. Then, the solutions to

$$\omega - k_0 v_{z0}(r) = 0 \quad (D-14)$$

determine the singular points. The r -dependent electron velocity is given by (Eq. 10, Section 2.1)

$$v_{z0}(r) = \tanh[A \ln(r/r_c)] \quad (D-15)$$

Because v_{z0} varies from 0 to v_e (maximum electron velocity), the real frequency range in which branch points occur is $0 < \omega < k_0 v_e$. In this range, there exists a continuum of solutions in the form of Eq. D-10 that are associated with slow space-charge waves. The continuum becomes unstable where it crosses a slow electromagnetic mode.

DISTRIBUTION

AUL/LSE, Maxwell AFB, Ala.
DTIC/FDAC, Alexandria, Va.
AFWL/SUL/HO, Kirtland AFB, N. Mex.
AFCSA/SAMI, Washington, D.C.
AFWL/CA, Kirtland AFB, N. Mex.
AFWL/AWP, Kirtland AFB, N. Mex.
AFSC/XTWT, Andrews AFB, Md.
AFOSR/NP, Bolling AFB, DC
DARPA/DEO, Arlington, Va.
Lawrence Livermore Natl Lab, Livermore,
Calif.
Sandia Natl Laboratories, Albuquerque,
N. Mex.
Science Applications, Inc., Albuquerque,
N. Mex.
Los Alamos Natl Laboratory, Los Alamos,
N. Mex.
Mission Research Corp, Albuquerque,
N. Mex.
University of Alabama, Tuscaloosa, Ala.
Massachusetts Institute of Technology,
Cambridge, Mass.
Naval Research Laboratory, Washington,
DC
Voss Scientific, Cedar Crest, N. Mex.
OFFICIAL RECORD COPY
AFWL/AWPB, Kirtland AFB, N. Mex.